University of Évora

ARCHMAT
(ERASMUS MUNDUS MASTER in ARCHaeological MATerials Science)

Mestrado in Arqueologia e Ambiente (Erasmus Mundus - ARCHMAT)

Development and optimisation of protocols for surface cleaning of Cultural Heritage metals

Carla Lucía Soto Quintana (34316)

Dr. Emma Angelini
Politecnico di Torino
Co-supervisor

Dr. Ruth Lahoz Espinosa
Institute of Materials Science of Aragon
Co-supervisor

Dr. Nicola Schiavon
University of Évora
Co-supervisor

Évora, Portugal, September 2016

"I am among those who think that science has great beauty."

Marie Skłodowska Curie

UNIVERSITY OF ÉVORA

Abstract

Erasmus Mundus Master in Archaeological Materials Science

Development and optimisation of protocols for surface cleaning of Cultural Heritage metals

by Carla Lucía Soto Quintana

The conservation and valorisation of cultural heritage is of fundamental importance for our society, since it is witness to the legacies of human societies. In the case of metallic artefacts, because corrosion is a never-ending problem, the correct strategies for their cleaning and preservation must be chosen. Thus, the aim of this project was the development of protocols for cleaning archaeological copper artefacts by laser and plasma cleaning, since they allow the treatment of artefacts in a controlled and selective manner. Additionally, electrochemical characterisation of the artificial patinas was performed in order to obtain information on the protective properties of the corrosion layers. Reference copper samples with different artificial corrosion layers were used to evaluate the tested parameters.

Laser cleaning tests resulted in partial removal of the corrosion products, but the laser-material interactions resulted in melting of the desired corrosion layers. The main obstacle for this process is that the materials that must be preserved show lower ablation thresholds than the undesired layers, which makes the proper elimination of dangerous corrosion products very difficult without damaging the artefacts. Different protocols should be developed for different patinas, and real artefacts should be characterised previous to any treatment to determine the best course of action.

Low pressure hydrogen plasma cleaning treatments were performed on two kinds of patinas. In both cases the corrosion layers were partially removed. The total removal of the undesired corrosion products can probably be achieved by increasing the treatment time or applied power, or increasing the hydrogen pressure. Since the process is non-invasive and does not modify the bulk material, modifying the cleaning parameters is easy.

EIS measurements show that, for the artificial patinas, the impedance increases while the patina is growing on the surface and then drops, probably due to diffusion reactions and a slow dissolution of copper. It appears from these results that the dissolution of copper is heavily influenced by diffusion phenomena and the corrosion product film porosity.

Both techniques show good results for cleaning, as long as the proper parameters are used. These depend on the nature of the artefact and the corrosion layers that are found on its surface.

Acknowledgements

First, I would like to express my sincere gratitude to my advisers Dr. Emma Angelini from Politecnico di Torino, Dr. Ruth Lahoz Espinosa from the Institute of Materials Science of Aragon, and Dr. Nicola Schiavon from the University of Évora, for the continuous support during the development of my research, for their patience, motivation, and immense knowledge, and for their insightful comments and encouragement, which helped me widen my research from various perspectives. I could not have imagined having better advisers and mentors during this project.

My sincere thanks also goes to Dr. Sabrina Grassini, Dr. Marco Parvis, and Elisabetta di Francia from Politecnico di Torino, who gave me the opportunity to join their team during my research project, and Dr. Luis Alberto Angurel and Dr. Xermán de la Fuente from the Institute of Materials Science of Aragon for their advice. Without their precious support it would not have been possible to conduct this research.

I would like to acknowledge and thank the Education, Audiovisual and Culture Executive Agency (EACEA) of the European Commission for providing me with a scholarship to attend the Erasmus Mundus Master in Archaeological Materials Science, and the coordinators and professors of the ARCHMAT course.

I thank my fellow classmates Aman Maldewo, Drita Abazi, Rana Abboud, Diego Badillo, Francisco Céntola, Leonor Costa, Elisaveta Demidova, Dela Kuma, Dauren Adilbekov, Whitney Jacobs, Guilhem Mauran, Milan Markovic, Ivona Posedi, Ilona Viliūnaitė, and Indrė Žalaitė for the stimulating discussions, for the sleepless nights we were working together before deadlines, and for all the fun we have had in the last two years.

Last but not least, I would like to thank my friends and family: my parents, sisters, and grandmother for their unfailing support and continuous encouragement throughout my years of study and my life in general. This accomplishment would not have been possible without them.

Thank you.

Contents

List of Figures

List of Tables

Acronyms

EIS	elctrochemical impedance spectroscopy
FESEM	field emission scanning electron microscopy
FWHM	full width half maximum
LACONA	Lasers in the Conservation of Artworks
laser	light amplification by stimulated emission of radiation
PLA	pulsed laser ablation
PMT	photomultiplier tube
sccm	standard cubic centimetre per minute
SHE	standard hydrogen electrode
μXRD	X-ray micro-diffraction

Symbols

A	area	cm^2
α_{eff}	(effective) absorption coefficient	cm^{-1}
D	thermal diffusivity	m^2/s
δ	ablation depth	µm
ρ	density	g/cm^3
d_{line}	interlining	µm
d_{pulse}	distance between pulses	µm
E	energy	J
E_a	absorbed energy	J
E_{cr}	critical energy	J
E_r	reflected energy	J
E_t	transmitted energy	J
F	fluence	J/cm^2
F_a	attenuated fluence	J/cm^2
F_{th}	ablation threshold	J/cm^2
F_{tr}	transmitted fluence	J/cm^2
I	irradiance	W/cm^2
ν_r	repetition rate	pulse/s
$p_{overlap}$	pulse overlap	pulses/mm
P	power	W
P	pressure	Pa
T	temperature	K
t	time	s
τ_l	pulse width	s
v_{scan}	scan speed	mm/s
W_a	ablation rate	$µm^3$/pulse
λ	wavelength	nm
z_{th}	heat diffusion length	µm

To my parents

Chapter 1

Conservation of Cultural Heritage metals

The conservation and valorisation of cultural heritage is of fundamental importance for our society, since it is witness to the artistic and industrial legacies of human societies. The information that can be gathered from such materials is a valuable source to understanding the past. A large component of this consists of material cultural assets that are often exposed to harmful long-term effects of environmental pollution, inappropriate handling, and intrinsic physicochemical instability.

In the case of metallic artefacts, one of the main problems is the preservation of archaeological objects taken out of excavation and stored in museums or deposits. Because corrosion is a never-ending problem, archaeologists and curators often face the challenge to choose the correct strategies for cleaning and preservation. Cleaning is one of the critical steps of the conservation process and involves stabilising the material and the exposure of hidden details on the surface of the artefact in question. As artefacts are often fragile and irreplaceable it is very important to choose suitable techniques and methods to avoid damage. Finally, they have to choose the correct strategy to stop, or limit, surface degradation phenomena in order to avoid further damage. Restoration procedures must be non-destructive, reversible, and they have to respect the integrity of the objects and satisfy specific requirements for preserving their aesthetic appearance (Angelini et al., 2014, 10-11; Grassini, Angelini, d'Agostino, Palumbo, & Ingo, 2007; Koh, 2005; Selwyn, 2004).

During burial, artefacts react with the environment and become covered with corrosion products of different compositions, mainly in dependence of the chemical composition of the artefact and of the soil components. Unlike iron artefacts, the patina of copper alloys, such as bronzes, is often considered valuable; for example, on bronze statues the patinas are deliberately produced in order to get the required colour. The most common alteration products of copper and copper alloys are: oxides, sulphides, basic sulphates, chlorides, hydroxychlorides, basic green carbonates, and oxalates. Among them, corrosion products containing chlorides are considered very dangerous because copper and copper alloys which have been buried or

recovered from a wet site can suffer from the effects of chloride salts, resulting in the development of the so-called bronze disease (see Section 1.1.1). The products of the reaction are light green, powdery, voluminous basic chlorides of copper, which disrupt the surface and may disfigure the object. For this reason it is important to remove the chlorides in the most complete way (Angelini et al., 2007).

This work focuses on the development of protocols for cleaning copper artefacts by two different techniques which can be used for this purpose: laser and plasma cleaning. This chapter is used to give an introduction into the importance of copper in cultural heritage, its main corrosion products, and common conservation techniques (Section 1.1).

1.1 Copper in Cultural Heritage

Pure copper (Cu) is a light red to salmon pink in colour, ductile, and malleable metal. It is non-magnetic, has high thermal conductivity, and can be easily soldered and brazed. Because copper lacks mechanical strength, it is rarely used in this form, but can be alloyed with other elements to provide materials with a broad range of mechanical, physical and chemical properties (e.g. increased hardness, reduced melting point, change in surface appearance and improved corrosion resistance). Brass - an alloy of copper and zinc (Zn) - and bronze - an alloy of copper and tin (Sn) - are the best known examples. Besides utilitarian objects, copper and its alloys were (and still are) appreciated decorative metals which have been used throughout history for the realisation of various art objects, from jewellery to statuary (Selwyn, 2004).

Copper was one of the earliest metals to be used by humans - the first recorded use dates from around 8500 B.C. in the Near East (Selwyn, 2004). The first undisputed evidence for human exploitation of native copper comes from a Neolithic site in south-eastern Turkey, where beads of malachite and native copper, dated around 7000 B.C.,were found (Scott, 2002). Much of the early copper metalwork was made from native copper, and many of the smaller artefacts are merely hammered native copper. Some of the larger items, such as hammer-axes, are cast native copper. Evidence for the smelting of copper has been found at Turkish sites, dating back to the sixth millennium B.C. (Tylecote & Institute of Materials (Great Britain), 1992).

Bronze started to be made from the fourth to the third millennium B.C. and became widely spread during the Bronze Age. In the full Bronze Age, the attention to detail increased, with the production of finer objects and more accurate castings. An addition of lead was often made to increase the fluidity of the metal. However, the leading of bronzes was rather local and by no means universal (Tylecote & Institute of Materials (Great Britain), 1992). Brass, the alloy of copper and zinc, was restricted in early usage. By co-smelting zinc and copper ores, brass did become important during the Roman period. From 45 B.C. on, for example, the Romans produced brass coinage (Scott, 2002).

In common with many other metals, copper corrodes once it comes into contact with an aggressive environment, for example the sea or the atmosphere. In the field of art, copper-based objects are preferred in the corroded state, not only because of the aesthetically pleasing colours, but also because the presence of corrosion products provides evidence of time past and time passing, thereby adding extra value to the object. In the majority of cases, corrosion compounds even tend to be protective for the underlying metal and become a permanent part of the object to which they are attached. However, corrosion may also form a problem, especially when specific corrosion products (such as cuprous chlorides) are in contact with the metal core, if it masks the object's surface or weakens its physical structure. In specific corrosion conditions, the deterioration of the underlying metal will continue and will lead to the destruction of the object. One of the first steps in caring for metal objects is therefore to determine whether corrosion is desirable or dangerous. Where corrosion is found to be a problem, strategies have to be sought to prevent it from happening or to successfully treat the problems it causes (Leyssens, 2006; Selwyn, 2004). This work aims to remove the dangerous corrosion products associated with copper-based objects without affecting the protective patina or aesthetic value of the artefact.

1.1.1 Corrosion of Copper and its alloys

The corrosion of metals is the degradation of the metallic structure at its surface through chemical reactions of the metal with species of the environment. In contrast to mechanical wear, corrosion is principally a chemical process. The surface damage is not the result of abrasion of metal particles, but rather the transition of metal atoms from the metallic to the non-metallic state of a chemical compound (Kaesche, 2003). The surface of nearly all ancient metal objects which are buried in soil, immersed in fresh or in salt water or exposed to air, rain and sun, will certainly undergo these transformations. The surface alteration may be quite thin and superficial or it may be so complete that nearly none of the original metal remains. Eventually, the metal reverts to mineral forms (Gettens, 1961, sup1).

Most corrosion phenomena are electrochemical in nature. They imply two or more electrode reactions: the oxidation of a metal (anodic partial reaction) and the reduction of an oxidising agent (cathodic partial reaction) (Selwyn, 2004; Plenderleith & Werner, 1971). Furthermore, the corrosion process also requires an ionic connection (an electrolyte) between the anode and cathode to allow the flow of ionic species. In most corrosion processes, this ionic connection is provided by water, e.g. condensation from humid air, rain, or seawater. Whenever the relative humidity is higher than 65 %, there is enough absorbed water on most clean metal surfaces to approach the behaviour of bulk water and support electrochemical reactions. Damp soil or a damp deposit may also hold water against the surface of metal. The anodic half-reaction describing the oxidation of copper is given by Reaction {1}.

$$\mathrm{Cu(s)} \longrightarrow \mathrm{Cu^{2+} + 2e^-} \quad \{1\}$$

$$\mathrm{O_2 + 2H_2O + 4e^-} \longrightarrow \mathrm{4OH^-} \quad \{2\}$$

$$\mathrm{2H^+ + 2e^-} \longrightarrow \mathrm{H_2(g)} \quad \{3\}$$

The metal cations released at the anode may enter the environment as aqueous ions and precipitate away from the metal. Therefore, the metal continues to corrode. The metal is then in a so-called "active" state. Alternatively, the metal cations may react immediately with anions in the environment and form corrosion products (carbonates, oxides, hydroxides, sulphates, etc.) which adhere to the surface of the metal. Sometimes there is a progressive growth of the surface minerals which increases at the expense of the metallic core; in other cases, the mineralisation is compact, stable, and tends to inhibit further change. The metal is then said to be in a "passive" state (Plenderleith & Werner, 1971; Pourbaix & Burbank, 1963; Selwyn, 2004).

In each case, the electrons produced by the metal oxidation half-reaction at the anode must be simultaneously consumed by a balancing reduction half-reaction at the cathode. In aqueous solutions, this reaction is usually the reduction of hydrogen ions (Reaction {3}) or the reduction of oxygen (Reaction {2}). However, in general, the species co-reducing may be any species in the corrosive electrolyte reducing at a more positive potential than the metal system (Crow, 1994; Selwyn, 2004; Hamann, Hamnett, & Vielstich, 2007).

The corrosion of copper can be classified according to the corrosive environment to which an artefact is exposed. For archaeological bronzes, five corrosive environments can be considered: atmospheric conditions, indoor museum environment, soil (burial) conditions, marine environment, and post-excavation environment (Scott, 2002; Selwyn, 2004). Depending on the environment, different corrosion products are formed; for example malachite is typically formed in soil, brochantite in the atmosphere, and atacamite in seawater. However, objects can be corroded in different environments during certain stages in their lifetime. This means that archaeological artefacts are usually associated with complex corrosion mechanisms and that different corrosion compounds can be formed during exposure to different environments. Furthermore, even apparently identical objects discovered only a few metres apart on the same site, can be corroded in totally different ways since chemical defects such as damage, segregations and inclusions, as well as structural defects, such as grain boundaries, dislocations and stresses within the materials, might influence the occurring corrosion phenomena (Leyssens, 2006).

An overview of common copper minerals and corrosion products is given in Table 1.1, followed by a brief description of the corrosion products which are most relevant to this work.

TABLE 1.1: Typical copper corrosion products (Scott, 2002; Selwyn, 2004)

Chemical name	Mineral name	Chemical formula	Colour
copper(I) oxide	cuprite	Cu_2O	red
copper(II) oxide	tenorite	CuO	black
copper(II) hydroxide	spertiniite	$Cu(OH)_2$	blue green
copper(II) carbonate hydroxide	malachite	$Cu_2(CO_3)(OH)_2$	pale green
copper(II) carbonate hydroxide	azurite	$Cu_3(CO_3)_2(OH)_2$	blue
copper(II) carbonate hydroxide	georgeite	$Cu_2(CO_3)(OH)_2$	pale blue
copper(II) sodium carbonate trihydrate	chalconatronite	$Na_2Cu(CO_3)_2 \cdot {}_3H_2O$	greenish blue
copper(I) chloride	nantokite	$CuCl$	palegrey
copper(II) chloride hydroxide	atacamite	$Cu_2Cl(OH)_3$	pale green
copper(II) chloride hydroxide	paratacamite	$Cu_2Cl(OH)_3$	pale green
copper(II) chloride hydroxide	clinoatacamite	$Cu_2Cl(OH)_3$	pale green
copper(II) chloride hydroxide	botallackite	$Cu_4Cl_2(OH)_6 \cdot H_2O$	pale green
copper(II) hydroxide sulphate	brochantite	$Cu_2(SO_4)(OH)_6$	dark green
copper(II) hydroxide sulphate	antlerite	Cu_3SO_4	vitreous green
copper(II) hydroxide sulphate monohydrate	posnjakite	$Cu_2(SO_4)(OH)_6 \cdot H_2O$	vitreous green
copper(II) sulphate pentahydrate	chalcanthite	$CuSO_4 \cdot {}_5H_2O$	deep blue
copper(I) sulphide	chalcocite	Cu_2S	blackish grey
copper(II) sulphide	covellite	CuS	dark blue

Copper oxides

The most widely occurring alteration product of ancient copper and its alloys is cuprite (Cu_2O). Cuprite typically has a lustrous dark red to orange red colour, although it may exhibit a range of colours; yellow, orange, red or dark brown, depending on impurities, non-stoichiometry and particle size. Cuprite occurs over a wide range of conditions; it can form on a bronze by exposure to moist air, by tarnishing in use, or during burial. For the majority of bronzes, cuprite is the corrosion layer which immediately overlays the original metallic surface. Usually most of the cuprite is concealed beneath overlaying green basic copper salts.

Tenorite is usually a dull black cupric oxide (CuO) and a rare component of natural patinas. When it is present as a patina constituent, it usually indicates that the object has been subjected to heating before or during burial (Scott, 2002).

Copper carbonates

Only two of the copper carbonate minerals are important as corrosion products; these are the green malachite ($Cu_2(OH)_2CO_3$) and the blue azurite ($Cu_3(OH)_2(CO_3)_2$). The two minerals are often identified in bronze patinas formed during land burials. Their formation on buried copper alloys is promoted by high levels of carbonate ions in groundwater (Selwyn, 2004). Furthermore, malachite and azurite are also found as minor phases in corrosion products formed during outdoor exposure or sea burial and as post-excavation alteration products of other minerals (Scott, 2002).

Malachite usually forms smooth, dark green compact layers on the surface of a bronze. Malachite can be a significant component of patinas that have developed during corrosion of copper alloys buried into the soil, where it usually forms over an initial cuprite layer. The formation of azurite is favoured at higher carbonate levels. However, azurite is less stable than malachite and may be converted to it in the presence of moisture through the loss of carbon dioxide. Probably for this reason, azurite is less common than malachite. Azurite sometimes occurs on objects as a compact, continuous, dark blue layer, but more frequently as fine crystal aggregates scattered among patches of malachite (Scott, 2002; Selwyn, 2004).

Copper chlorides

The most important copper chlorides in bronze corrosion are nantokite (CuCl), and the copper trihydroxychlorides: atacamite, paratacamite, clinoatacamite and botallackite, all of which are isomers of $Cu_2(OH)_3Cl$ (Scott, 2002). Nantokite is a naturally occurring, pale grey, wax-like mineral with low solubility in water. It forms under conditions of high chloride ion concentration, acidity and low oxygen conditions. In moist air, nantokite is unstable and it reacts with oxygen and water to produce copper trihydroxychlorides and hydrochloric acid. The main copper chloride hydroxides, also called basic copper chlorides, are atacamite ($\alpha-Cu_2Cl(OH)_3$)

and paratacamite ($\gamma-Cu_2Cl(OH)_3$). These are naturally occurring minerals with the same chemical formula but different crystal structures, and they both have green colours. On outdoor bronzes, atacamite and paratacamite are mostly found in sheltered and partly exposed areas. These are areas not readily washed by rain, where enough chlorides could accumulate (Scott, 2002; Selwyn, 2004).

Chloride containing corrosion products are normally associated with a marine environment. However, the copper chlorides catch the most attention for their role in bronze disease. This term has long been used to describe the appearance of powdery light green spots on the surface of archaeological copper alloys after excavation. Objects exhibiting this form of corrosion were once said to be diseased or sick, and the cause was attributed to bacterial or fungal infection. However, it is now known that this corrosion is caused by chloride contamination. Bronze disease originates from the existence of cuprous chloride in close proximity to whatever metallic surface may remain. As long as the nantokite is isolated from the surrounding air by the outer layers of corrosion, it remains unreacted. However, if the protective outer material covering the nantokite is cracked, damaged, or even removed, the nantokite is exposed to the surrounding environment. Reaction with moisture and oxygen causes this unstable compound to convert to one of the copper trihydroxychlorides (Scott, 2002; Selwyn, 2004).

Bronze disease is a form of pitting corrosion which includes the presence of a deposit of cuprous chloride under a layer of cuprite (Cu_2O). The cuprite layer acts as a bipolar electrode: corrosion (anodic) reactions occur on the metal side of the cuprous oxide membrane, while oxygen reduction (cathodic) reactions occur on the environmental side. The driving force for the pitting reaction is the concentration gradient of copper(I) species between the bottom of the pit and the corrosion mound above the Cu_2O film. In the presence of chloride ions, the normally insoluble CuCl can further react to form a series of soluble complexes, such as $CuCl_2^-$ and $CuCl_3{}^-{}_2$, in the pit. These copper(I) species diffuse through cracks in the Cu_2O membrane and are then oxidised by molecular oxygen to cupric ions (Scott, 1990). A schematic representation of this phenomenon is depicted in Figure 1.1.

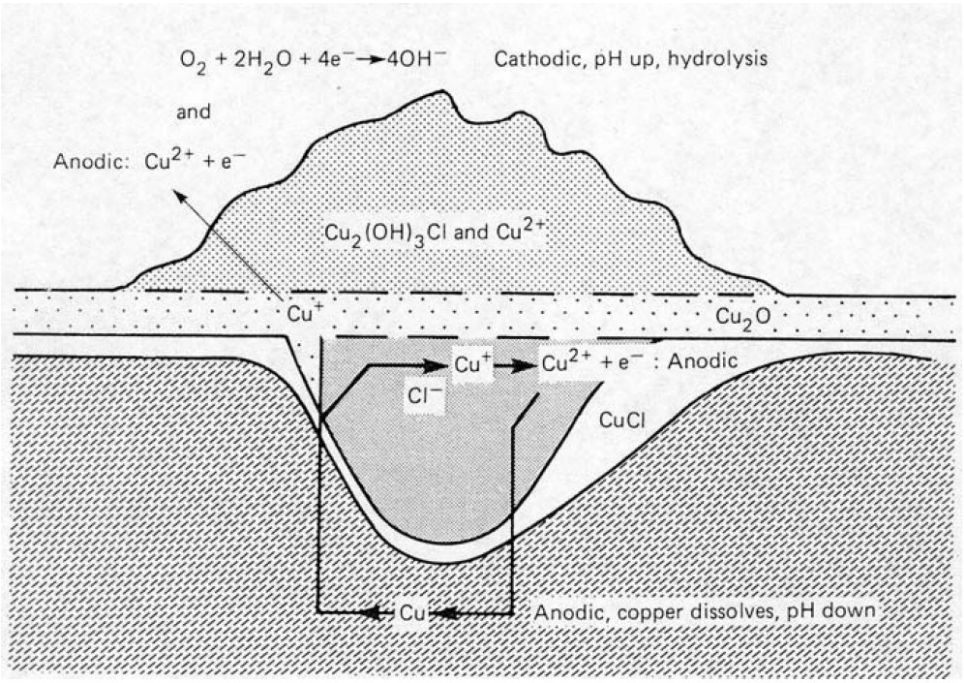

FIGURE 1.1: Schematic representation of the major oxidation and reduction reactions involved in Bronze disease (Leyssens, 2006)

1.1.2 Conservation methods

Conservation is the preservation of cultural property for the future. Conservation activities include examination, documentation, treatment, and preventive care, supported by research and education. Preventive conservation is an important element of museum policy and collections care. It is an essential responsibility of members of the museum profession to create and maintain a protective environment for the collections in their care, whether in store, on display, or in transit. The principal goal should be the stabilisation of the artefact. All conservation procedures should be documented and be as reversible as possible, and all alterations should be clearly distinguishable from the original artefact.

Restoration is a process that attempts to return the work of art to some previous state that restorer imagines to be the original one, this was commonly done in the past. In the late twentieth century a different concept of conservation has been developed, more concerned with preserving the work of art for the future, and less with making it look pristine. The concept of restoration remains controversial, since it often involves some irreversible change to the original material of the artwork with the goal of making it "look good". The attitude of restorers in recent years is to make all the restoration they undertake reversible. Art conservation can involve the cleaning and stabilisation of the work of art. Ideally, any process used is reversible, but in reality cleaning is not a reversible process and can sometimes be controversial due to fears that cleaning would damage the artefact (Angelini et al., 2007).

The investigation of metal artefacts and their conservation has been through major improvements in the last decades. In the past, large samples were required to perform an accurate investigative analysis, while today only a small amount of metal is needed. As regards conservation practices, the integrity of artefacts was previously not respected when cleaning the metal surface of its corrosion layers. As a result the original surface was often lost. Today, no intervention is possible without respecting the original surface and preserving any archaeological or historical information that can be retrieved during the cleaning process (Degrigny, 2007).

Corrosion on metal objects may be valued for its colour, beauty or stability. But it may also be disfavoured if it masks the object's intended surface. Moreover, it can even be dangerous if it weakens the object's physical structure. One of the first steps in caring for metal objects is therefore to determine whether corrosion is desirable or dangerous. Where corrosion is found to be a problem, conservation strategies have to be sought to prevent it from happening or to successfully treat the problems it causes. Conservation then encompasses three explicit functions: examination, preservation, and restoration. Examination is the preliminary procedure taken to determine the original structure and materials comprising an artefact and the extent of its deterioration, alteration, and loss. Preservation is action taken to retard or prevent deterioration or damage in cultural properties through control of their environment and/or treatment of their structure in order to maintain them, as nearly as possible, in an unchanging

state. Restoration is action taken to return a deteriorated or damaged artefact, as nearly as is feasible, to its original form, design, colour, and function with minimal further sacrifice of aesthetic and historic integrity (Leyssens, 2006; Selwyn, 2004).

Cleaning methods can usually be classified as mechanical, chemical, electrochemical, ultrasonic, plasma, or laser cleaning. In principle, they are aimed at removing dirt and undesirable corrosion products from the surface of a metal object. No single cleaning technique is able to resolve all conservation issues of an object so, each one has to be treated individually depending on the metal and environment to which it was exposed. Analysis of the object before treatment is an important step to determine the correct cleaning method(s).

Mechanical cleaning uses abrasive, scraping techniques to remove corrosion layers. Micro sandblasting, scalpel, scraper, rotating steel brush, drills, water jetting and other cleaning methods are common. While not as risky a method as chemical cleaning, irregular and imprecise removal of corrosion can disrupt the original surface of the object and remove valuable evidence about the archaeological context of an artefact.

Chemical cleaning consists on treating the surface of the object with a solution(s) that selectively removes corrosion products, over-cleaning or chemical modification and activation of the substrate can occur.

Electrochemical cleaning is commonly used to stabilise, clean and reverse further oxidation of a surface. As this method requires the use of an electrolytic solution, the risks associated are similar to those of chemical cleaning (Degrigny, 2007).

Laser and plasma cleaning allow for the treatment of artefacts in a controlled and selective manner, without any mechanical (and sometimes chemical) contact with the substrate. Due to the complexity of archaeological artefacts, further studies are needed in order to provide thorough descriptions of the interaction dynamics occurring in inhomogeneous multilayer stratifications (i.e. corrosion layers) (Siano, 2008). Hence, the selection of these techniques for this project. The working principles involved in the use of laser and plasma cleaning are discussed in Chapters 3 and 4, respectively.

Chapter 2

Methods

In this chapter, the basic principles behind the techniques used in this work for sample preparation and characterisation are discussed. They include artificial corrosion protocols, μXRD, FESEM, and confocal microscopy. The principles involved in laser cleaning and plasma cleaning are discussed in Chapters 3 and 4, respectively, and EIS is discussed in Chapter 5.

2.1 Artificial corrosion

Due to the uniqueness and inhomogeneous nature of archaeological artefacts, their use as samples for the evaluation of the processes assessed in this study is not advisable. Instead, copper coupons (Cu, 99.99 wt %) were artificially corroded. Artificial corrosion experiments were performed by two methods: immersion in a solution for an extended period, and electrochemical patination. The latter was carried out using a three electrode electrochemical cell (Figure 2.1) and an Ivium CompactStat: Portable Electrochemical Interface & Impedance Analyser potentiostat by Ivium Technologies (Netherlands), and controlled via IviumSoft. The three components of the cell are discussed in more detail below.

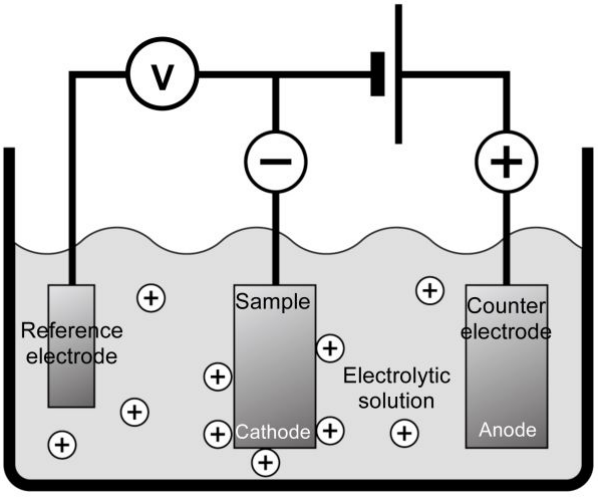

FIGURE 2.1: Schematic of a three electrode electrochemical cell (Bron et al., 2010).

2.1.1 Reference electrode

The main requirement of a reference electrode is that it has a stable potential which does not vary during the experiment. Silver-silver chloride electrodes - Ag/AgCl (3.000 mol/l KCl) - from AMEL Electrochemistry (Italy) were used as reference for all the experiments carried out in this work. The electrode consists of a silver wire coated with a thin layer of silver chloride, and contains potassium chloride (KCl) to stabilise the AgCl concentration. The electrode potential is 0.2100 V with respect to the SHE at 25 °C. The half cell reactions are given by reactions {4} and {5}, while the overall reaction is shown in reaction {6}.

$$Ag^+ + e^- \rightleftharpoons Ag\,(s) \quad \{4\}$$

$$AgCl\,(s) \rightleftharpoons Ag^+ + Cl^- \quad \{5\}$$

$$AgCl\,(s) + e^- \rightleftharpoons Ag\,(s) + Cl^- \quad \{6\}$$

2.1.2 Counter Electrode

The purpose of the counter electrode is to supply the current required by the working electrode. Therefore, it must be an electric conductor that closes the electric circuit. The electrode process at the counter electrode can be the decomposition of solvent or the oxidation or reduction of a component in the electrolyte. However, these reaction products must not interfere with the reaction being studied. This requires the choice of clean counter electrode chemistry. Counter electrodes made from stainless steel were used in this work.

2.1.3 Corrosion protocols

The artificially corroded samples acted as working electrodes. Prior to a patination protocol the electrodes were polished using 180, 320, 500, and 800 grit SiC sandpaper, and degreased with ethanol. Different protocols were used to obtain a cuprite patina, a paratacamite patina, and a cuprite and malachite patina (referred to as "malachite patina" in the rest of the document).

To obtain a cuprite (Cu_2O) patina, the samples were polarised at 84 mV (vs Ag/AgCl) for 16 h in a 0.1 mol/l Na_2SO_4 solution. While, samples were immersed for 2 months in a 0.5 mol/l NaCl solution to obtain a paratacamite ($Cu_2(OH)_2Cl$) patina (Leyssens, 2006). The malachite ($Cu_2CO_3(OH)_2$) patina was obtained by immersing the sample in an ASTM D1384 solution with added carbonates (corrosive water) (0.01 mol/l Na_2SO_4, 2.8×10^{-2} mol/l NaCl, and 16.1×10^{-2} mol/l $NaHCO_3$), and applying an anodic potential of 0.150 V (vs Ag/AgCl) for 2 h, followed by 96 h at 0.380 V (vs Ag/AgCl).

2.2 Characterisation methods

2.2.1 X-ray micro-diffraction

X-ray diffraction analysis is a versatile non destructive technique that reveals detailed information about the chemical composition and crystallographic structure of natural and manufactured materials. It is based on the irradiation of a sample with X-ray light and recording the reflected radiation.

Every atom scatters an incident X-ray beam in all directions. However, for atoms in a crystal, these scattered X-rays will interfere with each other. This process leads to the enhancement of the intensity of the scattered radiation in certain directions due to constructive interference controlled by the periodicity and symmetry of the crystals, and destructive interference in all other directions (Chung & Smith, 2000). The position of the peak is controlled by the Bragg equation (Equation (2.1)), where n is the order of a reflection, λ the wavelength, d the distance between parallel lattice planes and θ the so-called Bragg's angle between the incident beam and a lattice plane.

$$2d \sin\theta = n\lambda \tag{2.1}$$

When the path length in the crystal ($2d \sin\theta$) is a multiple of the wavelength, constructive interference occurs and diffraction is obtained (Ladd & Palmer, 2013). The diffracted intensities are determined by the type and arrangement of atoms within the crystal lattice. Atoms with more electrons scatter more strongly. Therefore, no two substances have absolutely identical diffraction patterns when one considers both the direction and intensity of all diffracted beams. The diffraction pattern is thus a fingerprint of a crystalline compound. For the identification of a crystalline compound, the combination of the peak positions and the intensity can be calculated or compared with reference diffraction patterns (Chung & Smith, 2000).

The most commonly applied method in X-ray crystallography for the identification of crystallic compounds in samples, on the other hand, is the powder method. More than 50 000 sets of powder diffraction patterns are archived in the Powder Diffraction File (PDF) of the Joint Committee of Powder Diffraction Standards (JCPDS) (Chung & Smith, 2000). Since the corrosion compounds present on bronze objects are of crystalline nature, it is possible to identify the species using powder XRD (De Ryck, Adriaens, Pantos, & Adams, 2003).

X-ray diffraction analysis performed on small samples or small areas of large samples is commonly referred to as micro-diffraction. Considered the technique of choice when samples are too small for the optics and accuracy of conventional diffraction instrumentation, the method employs a micro X-ray beam so that diffraction characteristics can be mapped as a function of sample position.

For this work μXRD was used to analyse the composition of corrosion layers in artificially corroded samples before and after cleaning treatments. Data was collected on a Rigaku (Japan)

D/MAX RAPID system equipped with an imaging plate and a two-dimensional area detector using Cu Kα radiation. Phase identification was performed using X'Pert HighScore 2.2 (PANalytical, Netherlands) software package.

2.2.2 Field Emission Scanning Electron Microscopy

The electron microscope allows a sample to be examined at far higher magnification and lateral resolution than is possible with light microscopy. A further, important advantage is a very large depth of field and the possibility of simultaneous imaging and localized chemical analysis. In brief, electrons are ejected from an electron source and accelerated and focused into a small probe that is scanned over the surface of a sample (Figure 2.2). As the electron beam is rastered sequentially over the sample surface, the signal of each point is recorded and stored individually. The magnification of the image is determined by the ratio of the size of the displayed image to the scanned area. The resolution is determined ultimately by the probe diameter, but more typically, by the size of the interaction volume (Adriaens & Dowsett, 2004).

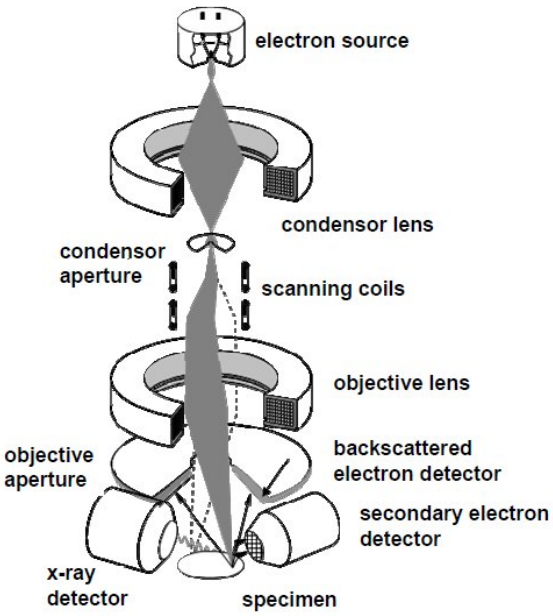

FIGURE 2.2: Schematic representation of a SEM-EDX instrument (Adriaens & Dowsett, 2004)

The power and versatility of electron microscopy derives from the variety of ways in which the primary electron beam interacts with the sample. As the primary electrons enter the sample bulk, they undergo elastic and inelastic collisions with atoms of the sample. The most common signal used for creating images is the secondary electron (SE) signal, made up of low energy electrons ejected from the sample surface by the interaction of the primary beam. Because the

intensity of the SE signal is primarily a function of sample surface morphology, SE images appear to be similar to a macroscopic surface seen with the naked eye.

Field emission scanning electron microscopy (FESEM) uses a field-emission cathode, instead of a thermoionic emitter, in the electron gun of a scanning electron microscope providing narrower probing beams at low as well as high electron energy, resulting in both improved spatial resolution and minimized sample charging and damage. FESEM provides topographical and elemental information at magnifications of 10x to 300 000x, with virtually unlimited depth of field. Compared to conventional scanning electron microscopy (SEM), FESEM produces clearer, less electrostatically distorted images with a spatial resolution down to 1.500 nm – three to six times better. A FESEM Zeiss Supra40 (Germany) microscope equipped with an Energy Dispersion Microprobe (EDAX 9900, USA) was used in this work for microscopic imaging.

2.2.3 Confocal microscopy

A confocal microscope creates sharp images of a specimen that would otherwise appear blurred when viewed with a conventional microscope. This is achieved by excluding most of the light from the specimen that is not from the microscope's focal plane. The image has less haze and better contrast than that of a conventional microscope and represents a thin cross-section of the specimen. Thus, apart from allowing better observation of fine details it is possible to build three-dimensional (3D) reconstructions of a volume of the specimen by assembling a series of thin slices taken along the vertical axis (Weeks & Semwogerere, 2013).

The image in a confocal microscope is achieved by scanning one or more focused beams of light, usually from a laser or arc-discharge source, across the specimen. This point of illumination is brought to focus in the specimen by the objective lens, and laterally scanned using some form of scanning device under computer control. The sequences of points of light (emission light of the fluorescence or reflected light of opaque materials) from the specimen are detected by a PMT through a pinhole, and the output from the PMT is built into an image and displayed by the computer (Weeks & Semwogerere, 2013; Paddock, 2000). The basic configuration of modern confocal systems can be seen in Figure 2.3

In this study, three-dimensional reconstructions of the surface in laser treated samples were obtained using an optical imaging profiler (Sensofar PLμ 2300, USA) with 10x/0.935, 20x/0.623 and 50x/0.350 objectives.

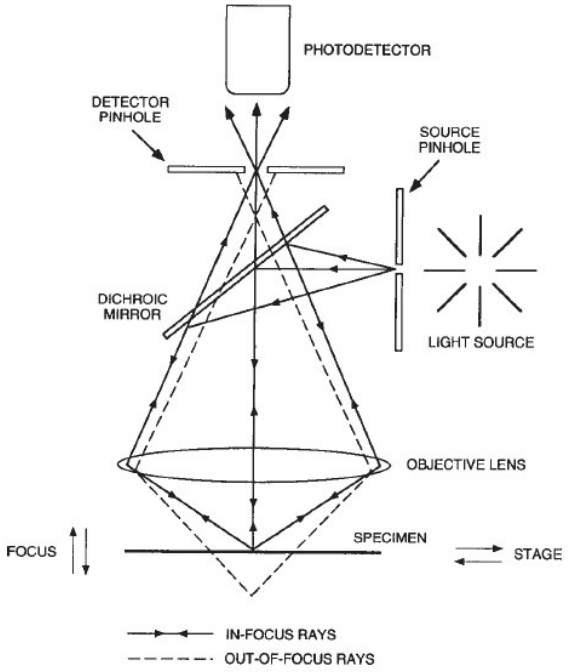

FIGURE 2.3: Basic configuration of modern confocal systems (Paddock, 2000).

Chapter 3

Laser cleaning

In this chapter, the principles involved in laser cleaning processes are explained (Section 3.1). Followed by a discussion of the laser cleaning treatments performed on artificially corroded copper samples (Sections 3.3 to 3.5) and their suitability for use on cultural heritage artefacts. Future works that can be done to optimise the cleaning process are discussed in the conclusions (Section 3.6).

3.1 Laser cleaning in Conservation

Light amplification by stimulated emission of radiation cleaning in conservation was first proposed by Asmus in the seventies. However, the limitations of lasers and high costs of the technique at the time meant that the approach stayed in the experimental stage for 20 years. In the 1990s several research centres and conservation institutions initiated the development of dedicated laser systems and methodologies for different materials. In 1995, the introduction of the international conference LACONA represented an important step for the consolidation of laser cleaning and extended the application of lasers to address other conservation problems. The conference has become a fundamental reference for the dissemination of laser techniques in the field and, since its introduction, other conferences have been instituted, as well as special sessions in interdisciplinary conferences. Presently, the importance of laser applications for the conservation of artworks and cultural heritage is evidenced by the increasing number of studies published in several international journals (Siano, 2008).

Cleaning of artworks and other artefacts is desirable from an aesthetic point of view, but is often absolutely necessary to prolong their lifetime. In laser cleaning, laser irradiation is used for the removal of unwanted materials, such as pollutants, dirt, and corrosion products, in a precise, accurate, and highly controlled manner. Other advantages of the method include site selectivity, lack of mechanical or chemical contact with the substrate, and diversity in the types of substrates that can be treated. On the other hand, with commercially available lasers, some difficulties in the precise control of output power, and changes in beam profile, are encountered. This can result in surface damage due to uncontrolled melting or ablation. This section

aims to provide an introduction of the main principles and physicochemical phenomena associated with the use of lasers and that should be taken into account when optimising laser treatments for cleaning, focusing on metals (Fotakis, 2007; Bäuerle, 2011).

3.1.1 Principles of Laser Ablation

Lasers are sources of temporally and spatially coherent light, which results in light that is strongly monochromatic. This property, along with high intensity (due to beam collimation) and the possibility to generate short and ultra-short pulses, meaning high peak power, makes laser light especially suited for applications in surface and materials science. In this context, two important variables are to be distinguished: the power per area or *irradiance* (I, W/cm^2) and the pulse energy per area or *fluence* (F, J/cm^2), also referred to as energy density (Rubahn, 1999).

Fluence is determined by Equation (3.1) where P is the average output power (W), ν_r is the repetition rate (pulse/s), and A is the spot area in cm^2. Irradiance is calculated by Equation (3.2), where τ_l is the pulse duration in seconds (s).

$$F = \frac{P}{\nu_r . A} \tag{3.1}$$

$$I = \frac{P}{\nu_r A . \tau_l} = \frac{F}{\tau_l} \tag{3.2}$$

In a simplified scheme, when a surface is irradiated, the energy (E, J) that interacts with the material may be absorbed (E_a), scattered, reflected (E_r), and transmitted (E_t). These phenomena produce attenuation (F_a) and spatial redistribution of the energy (diffusion). Figure 3.1 shows a qualitative representation of energy redistribution in homogeneous material layers in the case of absorption (Figure 3.1a) and scattering limits (Figure 3.1b), along with a composite situation of an absorbing layer on a diffusing substrate (Figure 3.1c). It's worth noting that, in cases of practical interest, the irradiated layers are strongly heterogeneous. Thus, the superposition of these phenomena must be taken into account for the description of the energy distribution.

The relative importance of the various terms in the above scheme may be controlled to a large extent when a laser is used as the radiation source. Thus, laser cleaning relies on the process of *ablation* - a consequence of the interactions mentioned above - for the removal of unwanted materials from a surface. When the surface of a material is irradiated with a laser beam, several mechanisms may be induced within the interaction volume, depending essentially, if not exclusively, on the interplay of the laser parameters and properties of the material being irradiated. Light amplification by stimulated emission of radiation parameters include

the wavelength, pulse energy, frequency, pulse width, and pulse overlap. The material is characterised by its chemical composition and microstructure, which determine thermal and optical properties that are important to understand the different interactions between lasers and materials. The efficiency of material removal, described by the *ablation rate* (W_a, μm^3/pulse), depends on these mechanisms. Light amplification by stimulated emission of radiation processing parameters have to be optimised depending on the nature of the materials to be removed and the underlying substrate so that unwanted products are ablated while the thermal and photochemical effects are contained as much as possible, so the original surface won't be affected. The processes that usually appear on the irradiated surface include heating, melting, evaporation, and plasma formation. A schematic of these processes can be seen on Figure 3.2. It is worth noting that the formation of intense plasma, while enhancing cleaning efficiency, dramatically reduces the control on side effects and the accuracy of material removal during the ablation process (Fotakis, 2007; Siano, 2008; Lahoz, Angurel, Brauch, Estepa, & de la Fuente Leis, 2013).

PLA involves the excitation of free electrons within a metal, or vibrations within an insulator. In general, the excitation energy is dissipated into heat in a short amount of time. Because of the fast heating and cooling rates achieved with pulsed lasers, material damage can often be ignored in cases where the ablated layer thickness is smaller than the heat penetration depth. With ns pulses this is often achieved when using a UV-laser. With VIS- and IR-laser radiation, this condition is harder to meet due to the lower absorption of many materials at longer wavelengths. Additionally, with increasing wavelength, laser-plasma interactions become more pronounced. Because of the high thermal conductivity of these materials, this can

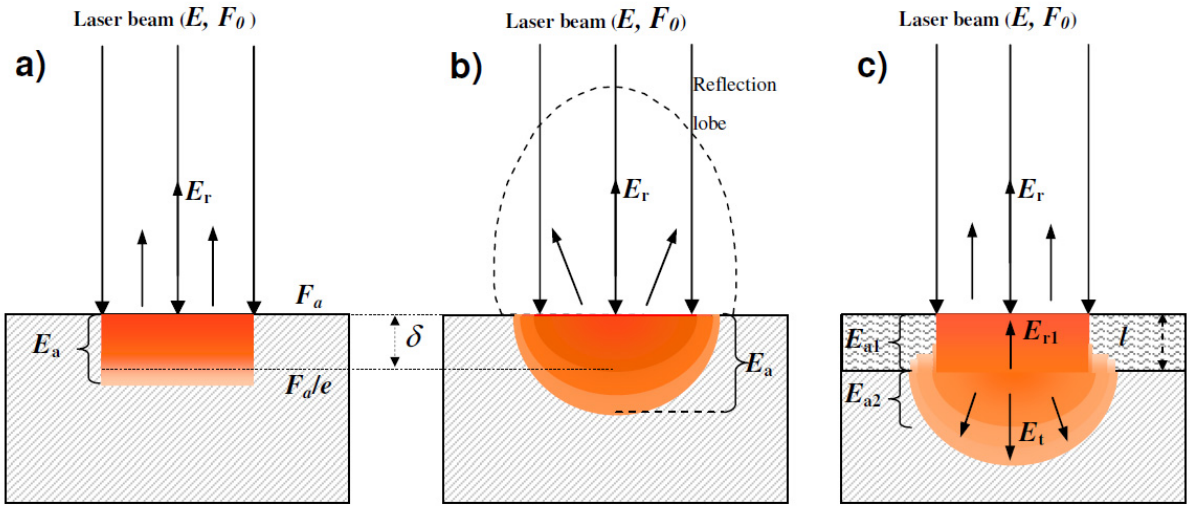

FIGURE 3.1: Representation of energy redistributions in laser-material interaction: absorbing material (a), diffusing material (b), and the adjacent absorbing and diffusing materials layers (c). (Siano, 2008)

only be fulfilled with ps or fs laser pulses.

The mechanisms induced by irradiation are usually described as thermal, photochemical, and photo-mechanical. At low irradiance values, a linear laser-material interaction can be assumed, for homogeneous surfaces. At high irradiance values, there can be significant coupling between the processes and the linear approach becomes questionable. A general description of the process requires the consideration of the different interaction mechanisms and their coupling. Figure 3.3 shows the different channels by which ablation can occur - thermal activation, direct bond breaking, or a combination of both. In all cases the process starts with single or multi-photon material excitation.

Thermal ablation occurs when the excitation energy is transformed into heat. The rise in temperature changes the optical properties of the material and therefore the absorbed power. This results in either, vaporisation - with or without surface melting - or explosive-type ablation, where there is material pop-off due to high stresses induced on the material's surface. If the photon energy is high enough, excitation can result in direct bond breaking - which causes atoms, molecules, clusters of fragments to desorb form the surface - or high stress induced by photochemically dissociated bonds that results in mechanical ablation. Both paths can occur, in principle, without any change in surface temperature and, thus, are known as photochemical ablation. In photophysical ablation, both thermal and non-thermal mechanisms contribute to the overall ablation rate.

Ablation being a thermally activated process, no real threshold exists. However, significant ablation is only observed above a certain fluence - known as the *ablation threshold* (F_{th}). The ablation threshold depends on the material, its microstructure and concentration of chemical and physical defects, and on the laser parameters, in particular the wavelength and pulse duration. Typical values for metals are within the range of 1 to 10, while inorganic insulators values, typically, fall between 0.50 to 2. With thin films, the ablation threshold becomes dependant on film thickness and substrate material (Bäuerle, 2011). Two models, namely the

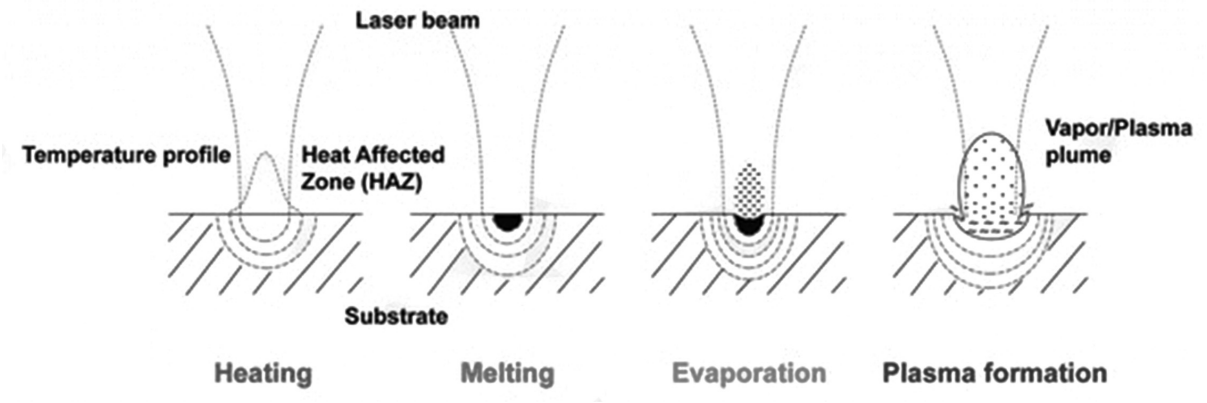

FIGURE 3.2: Physicochemical phenomena that can be induced on an irradiated surface (Lahoz et al., 2013).

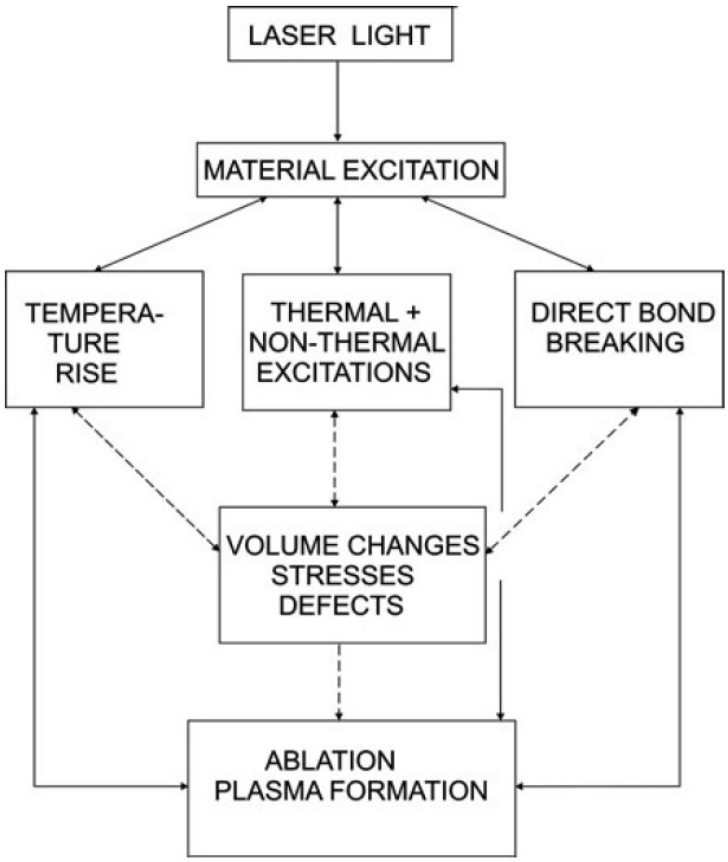

FIGURE 3.3: Different interaction and feedback mechanisms involved in PLA. Ablation can be based on thermal activation (left path), photochemical ablation (right path), or photophysical ablation (intermediate path) (Bäuerle, 2011)

steady-state and blow-off models, have been developed to evaluate the efficiency and accuracy of material removal that can be obtained with laser irradiation. These are used for describing the ablation depth (δ, µm) as a function of the incident laser fluence (Fotakis, 2007).

The steady-state model is based on the assumption that material removal occurs for fixed energy density, once F_{th} is exceeded. In this case, δ scales linearly with laser fluence:

$$\delta = \frac{F - F_{th}}{\rho E_{cr}} \qquad \text{for} \qquad F \geq F_{th} \tag{3.3}$$

Where E_{cr} is the critical energy per unit mass and ρ (g/cm^3) is the density of the material. This formula presumes that the rate of energy deposition is balanced by the rate of energy removal due to material ejection. For this balance to be attained, material ejection must start early on during the pulse. Thus, strictly speaking, this only applies for microsecond or longer laser pulses. However, for nanosecond pulses, the equilibrium implied in Equation (3.3) cannot be attained. In this case, material ejection is largely determined by the spatial distribution of the absorbed energy. So, for an incident fluence, all material within a depth exposed to a fluence above F_{th} is removed. This assumption results in the blow-off model for nanosecond laser pulses. Assuming Beer's law for the absorption process, and no reflection of the incident fluence, the dependence of material removal depth on incident fluence is now given by Equation (3.4) where F_{tr} is the transmitted fluence at depth δ, and α_{eff} (cm^{-1}) is the (effective) absorption coefficient.

$$F_{tr} = F.e^{\alpha_{eff}\delta} \geq F_{th} \quad \rightarrow \quad \delta = \frac{1}{\alpha_{eff}} \ln(\frac{F}{F_{th}}) \qquad \text{for} \qquad F \geq F_{th} \tag{3.4}$$

According to this model, what matters is the fluence absorbed at depth δ, whereas the absorbed energy in the ejected layers is essentially wasted (transformed into kinetic energy of the ejected material). Thus, the ejected material thickness increases with increasing fluence values.

For both models, the basic parameter characterising laser ablation processes is the ablation threshold. Generally, F_{th} scales as E_{cr}/α_{eff}, proving that it depends strongly on the substrate absorptivity.

Since these models are based on specific assumptions and simplifications, it is understandable that Equations (3.3) and (3.4) may fail to describe the complete ablation process. For instance, below F_{th}, an exponential dependence may be obeyed, whereas, close to the ablation threshold, δ may scale linearly even for ns pulses. Besides this, irradiation with successive laser pulses can result in different morphological changes and removal rates, and chemical modifications to the substrate, with a consequent change in the absorption coefficient and therefore reduction of ablation threshold. Thus, for fluence somewhat below the single-pulse ablation threshold, ablation may be induced after a certain number of pulses (incubation effect). Likewise, for ablation at fluencies slightly above F_{th}, the thickness removed per pulse may vary

with successive laser pulses, until a constant rate is reached.

In laser cleaning, the most important point is to achieve material removal with minimal side effects on the underlying substrate. As follows from Equation (3.4), the use of a wavelength that is relatively strongly absorbed by the unwanted material is required in order to achieve a good material removal rate. The criteria for the optimisation of this and other laser processing parameters are discussed in Section 3.1.2. However, because of the high variability in the nature of materials employed in Cultural Heritage, the study of a representative object sample is needed in order to provide a thorough description of the interaction dynamics and define the optimal laser parameters (Fotakis, 2007; Siano, 2008).

3.1.2 Laser Cleaning parameters

Ideally, laser cleaning should be a self-terminated process. When the correct laser parameters are used, the ablation process stops when the metal surface is reached. The absorbed laser fluence is too low to ablate the highly reflecting metal surface. While the ablation threshold for organic contaminants is very low, metal carbonates an oxides are much more stable. Due to the high diffusivity of metals and low absorptivity of contamination layers, well defined material removal is achieved with ultrashort-pulse lasers (Bäuerle, 2011). Some considerations on the parameters that can be modified, to optimise the cleaning process, are discussed in this section.

Wavelength

Wavelength selection depends greatly on the absorption coefficient of the unwanted material and underlying substrate due to the need of high absorptivity to achieve efficient material removal of the treated area. For UV-lasers, the activation of photochemical processes, that can induce chemical modifications, is a main concern. In metals, the corrosion products on each layer often vary greatly in a small area and the selection process becomes more complicated (Fotakis, 2007; Bäuerle, 2011).

Pulse duration

Thermal diffusion can be controlled by the laser pulse duration - or pulse width - to avoid heat propagation in cleaning. There are several energy modes in which a laser beam can be pulsed (e.g. Gaussian, top-hat). So, pulse width is defined by the FWHM of the peak, regardless of its shape [1]. It is important to consider the power affecting the surface, since the average output power can be considerably lower than the peak power. The peak power of a pulse increases as pulse duration decreases. This proportionality is also true for surface temperature and pressure. These characteristics can be seen on Figure 3.4.

[1] A detailed description of the different pulse modes can be found in Bäuerle, 2011

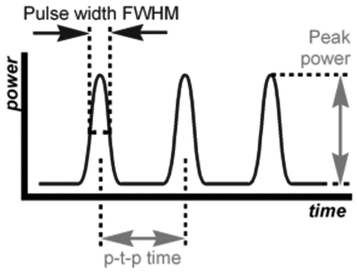

FIGURE 3.4: Laser pulse characteristics

Thermal side effects are usually negligible when the pulse duration is less than the thermal conduction time (i.e. ultra-short pulses). However, this becomes particularly important in the cleaning of metal artefacts due to their high absorptivity. Heat propagation into the material is represented by the heat diffusion length (z_{th}, µm) as expressed in Equation (3.5), where D (m^2/s) is the thermal diffusivity of the material.

$$z_{th} = 2\sqrt{D\tau_l} \tag{3.5}$$

Figures 3.5a and 3.5b show examples of the effect of different pulse durations on temperature (T) and heat diffusion length, respectively.

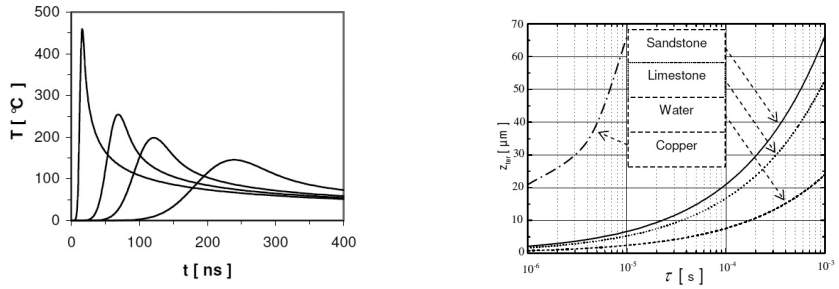

(a) Examples of temperature transients associated with Gaussian pulses of different duration.

(b) Thermal diffusion length as a function of pulse duration of different materials.

FIGURE 3.5: Effects of pulse duration on temperature (a) and thermal diffusion length (b) (Siano, 2008).

Pulse overlap

The discussion of thermal effects in Section 3.1.1 was focused on the effects of a single laser pulse. For cold processes (i.e. ultra-short pulses), when the overlapping between pulses (where two pulses in the same spot means a 100% overlap) is too high to allow the complete thermal relaxation between two consecutive pulses, thermal incubation can occur, resulting in a

larger thermal damage zone. In the nanosecond regime, thermal effects are induced by a single pulse, and are enhanced with increasing overlapping (Siano, 2008). Pulse overlap (p_{overlap}, pulses/mm) can be controlled by modifying the repetition rate and the scan speed of the laser (v_{scan}, mm/s) - which determine the distance between pulses (d_{pulse}, µm)-, and the interlining (d_{line}, µm), in the X and Y axes, respectively, as shown in Figure 3.6.

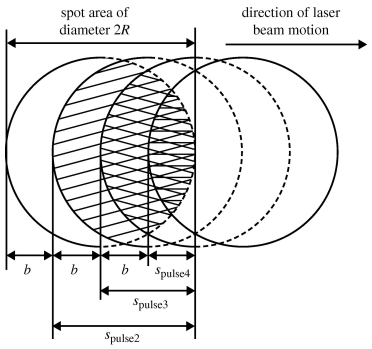

FIGURE 3.6: Graphic representation of laser pulse overlap.

3.1.3 Instrumentation

A Yb:YAG fibre laser (EasyMark-20), developed by Jeanologia (Spain), was used for laser cleaning tests. The laser operates at 1064 nm with a maximum output power of 20 W and a maximum repetition rate of 200 kHz. Pulses, with nanosecond to microsecond durations, are generated in Q-switching mode and focused by a convex lens with a focal length of 160 mm. The generated pulses have a Gaussian distribution and a spot diameter of 30 µm. The laser is controlled via a vector graphic editor, EzCAD2.6UNI (China), which enables the performance of rapid, precise, and complex surface treatments. The software allows the modification of the following laser parameters: power (1 % to 100 %), scan speed, repetition rate, pulse width, interlining, and number of cycles. Samples are positioned on a flat working surface at the focal distance of the lens (18.15 cm). The area to be treated can be defined using the CAD-like features of the software. Alternatively, when dealing with complex surfaces, a raster image of the sample can be uploaded to select the area with high precision.

3.2 Experimental parameters

Three, artificially corroded, copper samples, with different patinas - cuprite, paratacamite, and malachite - were treated by laser cleaning (Figure 3.7). The cuprite sample (Figure 3.7a) has a layer of reddish brown copper oxides, while the paratacamite sample (Figure 3.7b) has a green, highly translucent, crystals layer, and the malachite sample (Figure 3.7c) has a red oxides layer with big green transparent crystals on top.

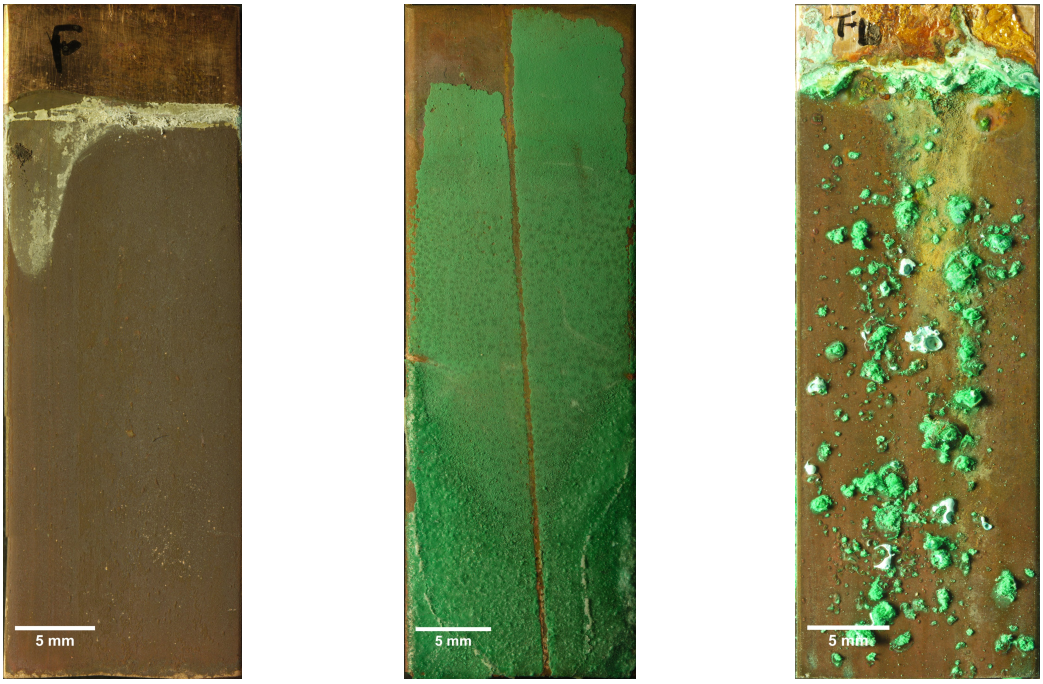

(a) (b) (c)

FIGURE 3.7: Samples used for laser cleaning tests, with a cuprite (a), paratacamite (b), and malachite (c) patina.

A set of tests was performed on each of the samples, the experimental parameters used are shown on Table 3.1. The selection of parameters was based on previous works performed in the Laser Applications Lab in collaboration with the Politecnico di Torino, where ablation thresholds of different patinas' composition were obtained (Hrnjic et al., 2015). The samples were then characterised by FESEM, confocal microscopy, and μXRD. The following sections discuss the results obtained from the cleaning treatments.

TABLE 3.1: Experimental parameters of laser cleaning tests

		Power (W)	Repetition rate (pulse/s)	Pulse width (ns)	Fluence (J/cm^2)	Irradiance (MW/cm^2)	Scan speed (mm/s)	Interlining (µm)	Pulse overlap (pulses/mm)	Cycles
	A	-	-	-	-	-	-	-	-	-
1	B	0.2500	20 000	8	1.770	221.1	300	15	66.67	1
	C	0.2100	20 000	8	1.490	185.7	300	15	66.67	1
	A	0.7700	20 000	8	5.450	680.8	300	15	66.67	1
2	B	0.2300	20 000	4	1.630	406.7	300	15	66.67	1
	C	0.2800	20 000	4	1.980	495.2	300	15	66.67	1
	A	0.7300	20 000	4	5.160	1291	300	15	66.67	1
3	B	0.4200	20 000	4	2.970	742.7	300	15	66.67	1
	C	0.5200	20 000	4	3.680	919.6	300	15	66.67	1
	A	0.4300	20 000	8	3.040	380.2	300	15	66.67	1
4	B	0.5800	20 000	8	4.100	512.8	300	15	66.67	1
	C	0.4200	20 000	14	2.970	212.2	300	15	66.67	1
	A	0.2100	20 000	8	1.490	185.7	300	15	66.67	2
5	B	0.2100	20 000	8	1.490	185.7	300	15	66.67	4
	C	0.2100	20 000	8	1.490	185.7	300	15	66.67	6
	A	0.2100	20 000	8	1.490	185.7	250	15	80	1
6	B	0.2100	20 000	8	1.490	185.7	200	15	100	1
	C	0.2100	20 000	8	1.490	185.7	150	15	133.3	1

3.3 Cuprite

Copper-based archaeological objects usually have a corrosion layer mainly composed of cuprite that should be preserved during conservation processes since it can act as a protective layer for the artefact itself. Laser cleaning tests were performed on an artificially corroded sample with a cuprite layer. An area of the sample with the original patina and a FESEM micrograph of the patina can be seen in Figures 3.8a and 3.8b, respectively.

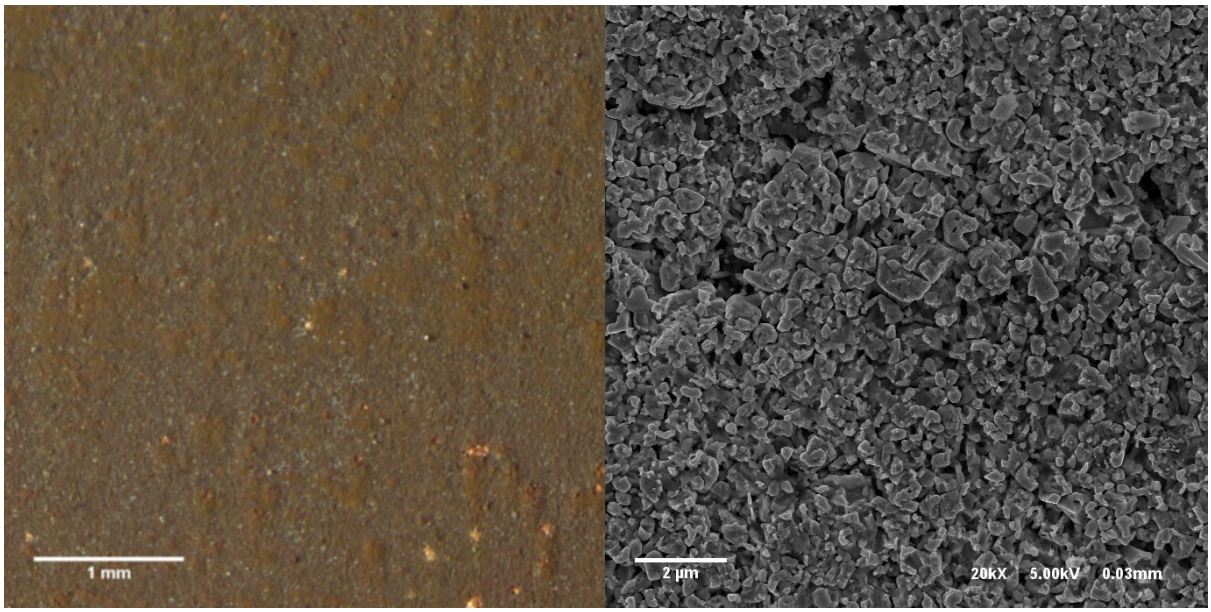

(a) (b)

FIGURE 3.8: Image of patina (a) and FESEM micrograph (b) of the cuprite patina sample before laser cleaning.

μXRD analysis shows that the corrosion layer is mainly composed of cuprite, with some copper oxide present (Figure 3.9). Also, peaks corresponding to copper from the source and substrate can be distinguished in the diffractogram.

After the laser tests, FESEM analysis of most areas shows signs of melting of the patina and, sometimes, the substrate, and the cuprite crystals are not visible any more. In some cases, the damage to the surface is also visible to the naked eye. An example of this is shown in Figure 3.10, where the visible damage caused by test A2 is seen in Figure 3.10a and the melted surface can be clearly seen in the FESEM micrograph of the same area (Figure 3.10b). It is evident from these results that the applied cleaning treatments were too aggressive for this kind of patina.

The areas where tests C1 and B2, with the lowest fluence values, show less damage than other areas, at least visibly. However, FESEM analysis shows that the outer part of the cuprite layer was melted during the process with both conditions (Figures 3.11 and 3.12). This could be related to an increase in the cuprite porosity or the tested layer in comparison with the layer

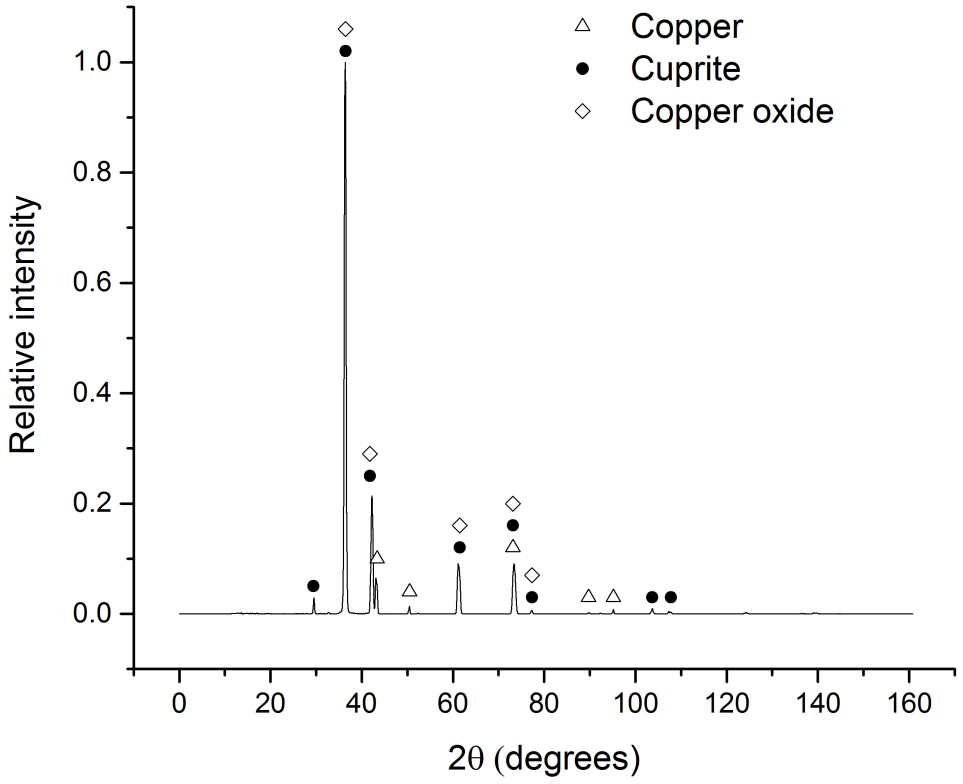

FIGURE 3.9: X-ray diffractogram of the cuprite patina with labelled peaks for copper, cuprite, and copper oxide.

used for obtaining the ablation thresholds. An increase in porosity favours melting in these type of oxides (Lahoz, 2006). This could explain why this irradiance values do not work in this new samples. Nevertheless, to understand the results and these being the mildest parameters used, μXRD and confocal microscopy analyses were carried out in these two areas.

Although the composition of the patina remains the same, in terms of compounds, a small change in the relative intensity of the peaks can be seen in the obtained diffractograms, more evident for laser condition C1 (Figures 3.13 and 3.14). This is especially visible for the copper and cuprite peaks around 43°, where the intensities are reversed when compared to the original patina, i.e. the intensity of the copper peak is higher than that of cuprite (Figure 3.9). At first this could indicate either a lower cuprite content, or a higher copper content, or both, but the cuprite layer thickness remains practically the same. This being said, it is possible that heterogeneity of the patina and the crystal disposition within the layer could lead to a relative intensity changes of the diffractogram peaks depending on the area selected for the characterisation. Also the highly sharpened peaks of the diffractograms suggest that the cuprite layer remains with high crystallinity despite the melted morphological appearance showed in the FESEM images. This suggests that only the outer part of the cuprite layer is melted under these conditions.

Confocal microscopy analysis (see Appendix A) confirms that the thickness of the cuprite patina did not suffer significant changes (Table 3.2), i.e. only a few microns of difference between the thickness of the original patina and tested areas, but the surface is seen to be

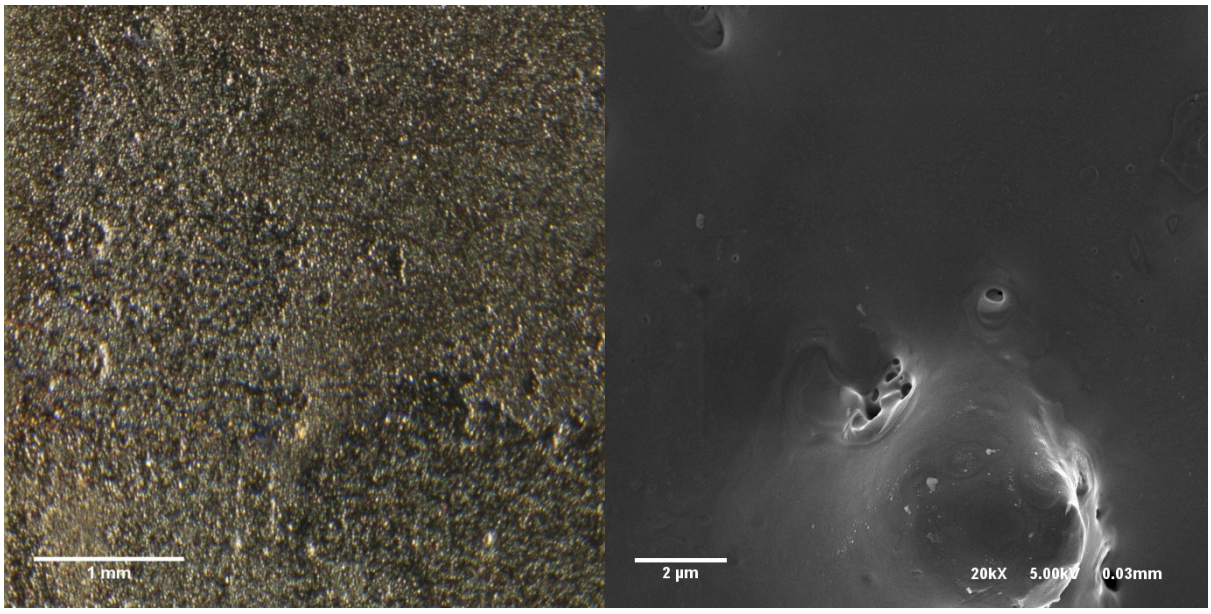

(a) (b)

FIGURE 3.10: Image (a) and FESEM micrograph (b) of test area A2 of the cuprite patina sample after laser cleaning.

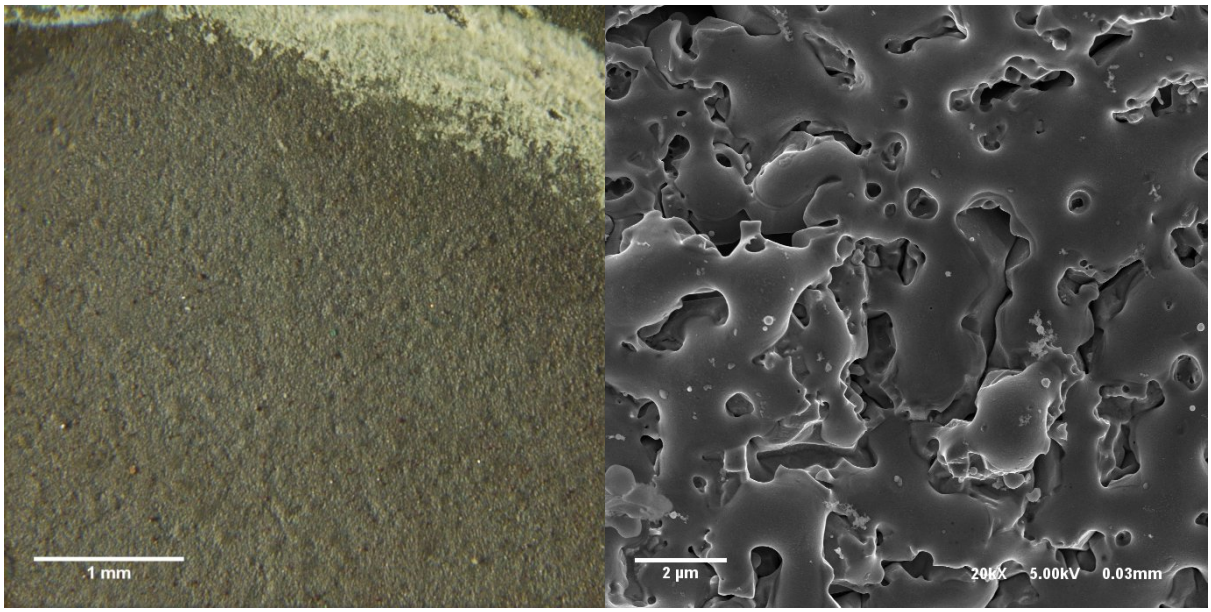

(a) (b)

FIGURE 3.11: Image (a) and FESEM micrograph (b) of test area C1 of the cuprite patina sample after laser cleaning.

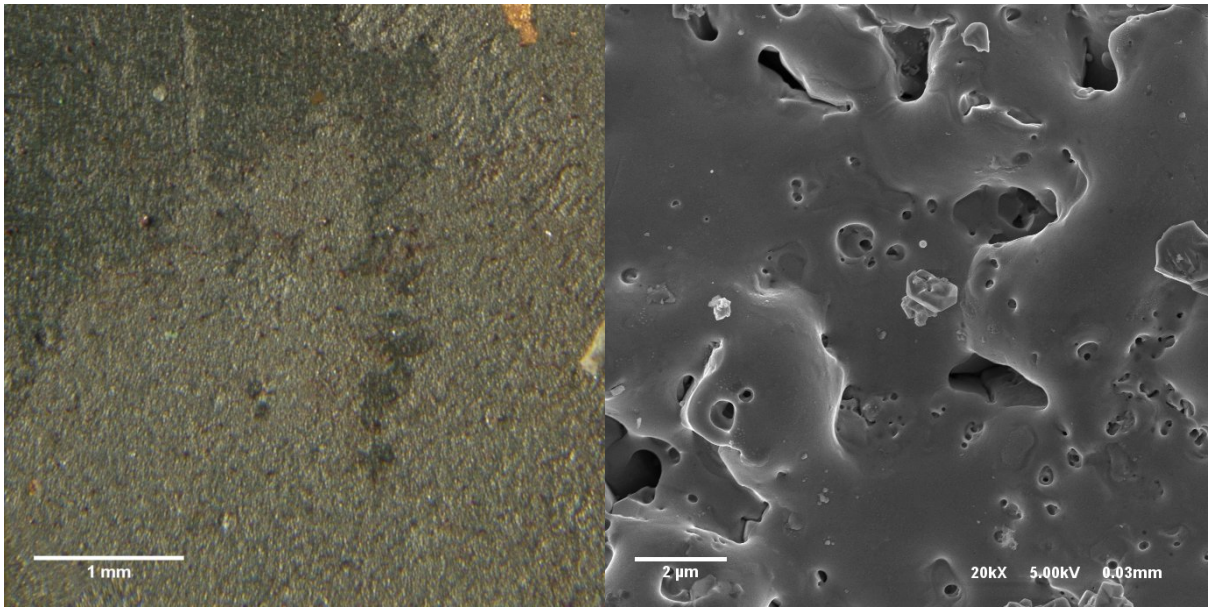

(a) (b)

FIGURE 3.12: Image (a) and FESEM micrograph (b) of test area B2 of the cuprite patina sample after laser cleaning.

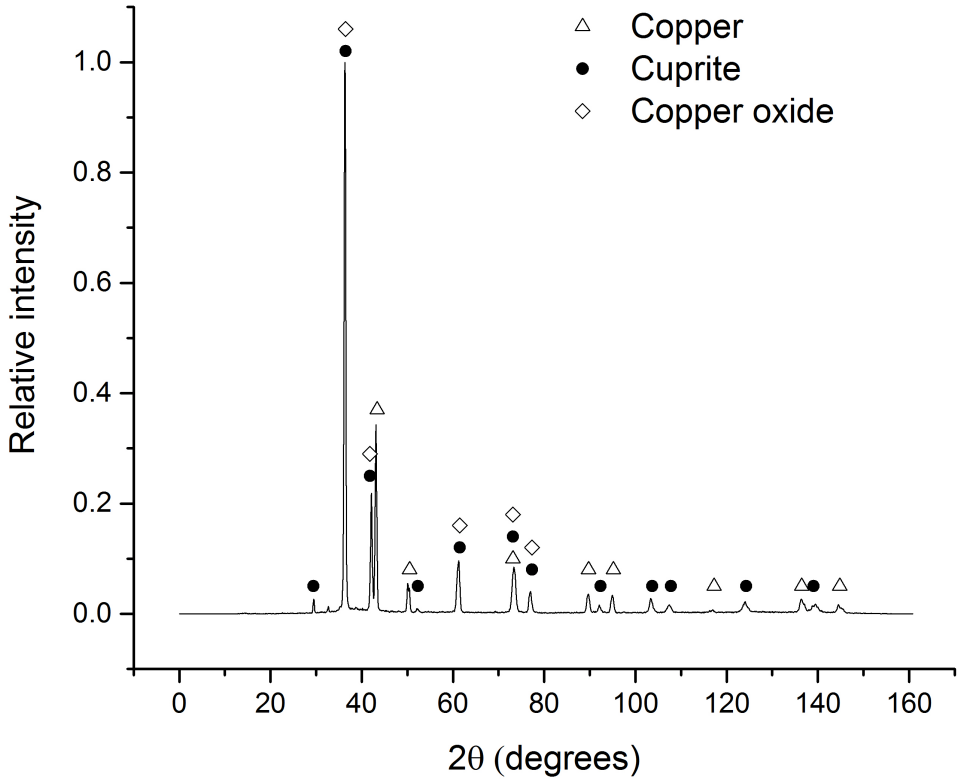

FIGURE 3.13: X-ray diffractogram of test area C1 of the cuprite patina sample with labelled peaks for copper, cuprite, and copper oxide.

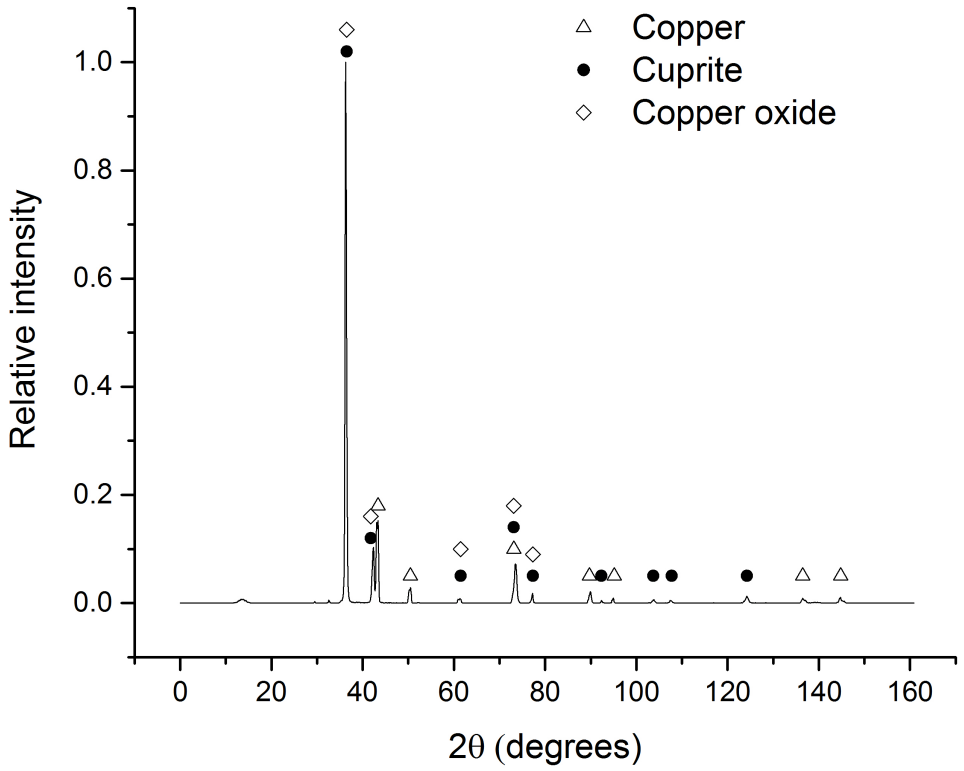

FIGURE 3.14: X-ray diffractogram of test area B2 of the cuprite patina sample with labelled peaks for copper, cuprite, and copper oxide.

smoother than that of the original layer, as can be seen in the surface plots shown in Figure 3.15, where the original patina is represented by the first half of the plot along the x-axis, and the second half represents the tested area.

TABLE 3.2: Average thickness of cuprite patina layer.

Area	Patina	A2	C1	B2
Average thickness (μm)	40	38	37	38

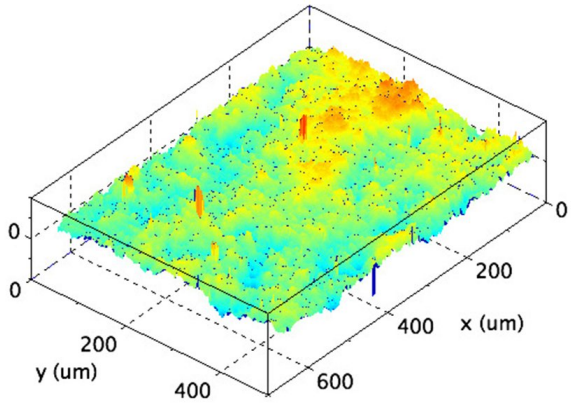

(a)

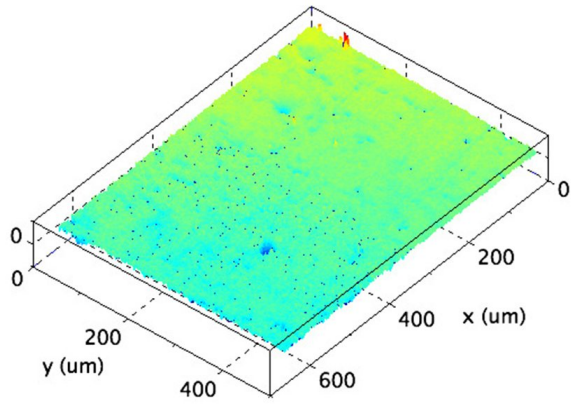

(b)

FIGURE 3.15: Confocal microscopy surface plots of test areas C1 (a) and B2 (b) of the cuprite patina sample. The surface of the original patina is plotted starting from 0 on the x-axis, the second half of the plot represents the treated area.

According to these results, a partial melting of the cuprite corrosion layer can be assumed during the cleaning process. Since this layer has a considerable porosity, the densification of the melted part could explain the small decrease in the layer thickness values. Evidence of this is the diminished roughness of the treated surfaces and the small difference in layer

thickness. Most likely, there is practically no removal of the corrosion layer with these laser conditions. It is worth mentioning that the morphological features observed in the FESEM micrographs of this sample (Figures 3.10b, 3.11b and 3.12b) are very similar to those observed on a melted metal, but based on the obtained results it is not possible to discern between a melted substrate and a melted patina. This could be achieved by analysing the cross-section of the treated samples.

3.4 Paratacamite

Similar to the cuprite sample discussed in Section 3.3, cleaning tests were performed on a sample with a paratacamite corrosion layer and the cleaned surfaces were characterised by field emission scanning electron microscopy. Test areas C1 and B2 were further analysed by μXRD and confocal microscopy. The original sample has a visible green paratacamite crystals layer, a high resolution image of an area of the sample can be seen in Figure 3.16a next to a FESEM micrograph, where the paratacamite crystals can be seen (Figure 3.16b).

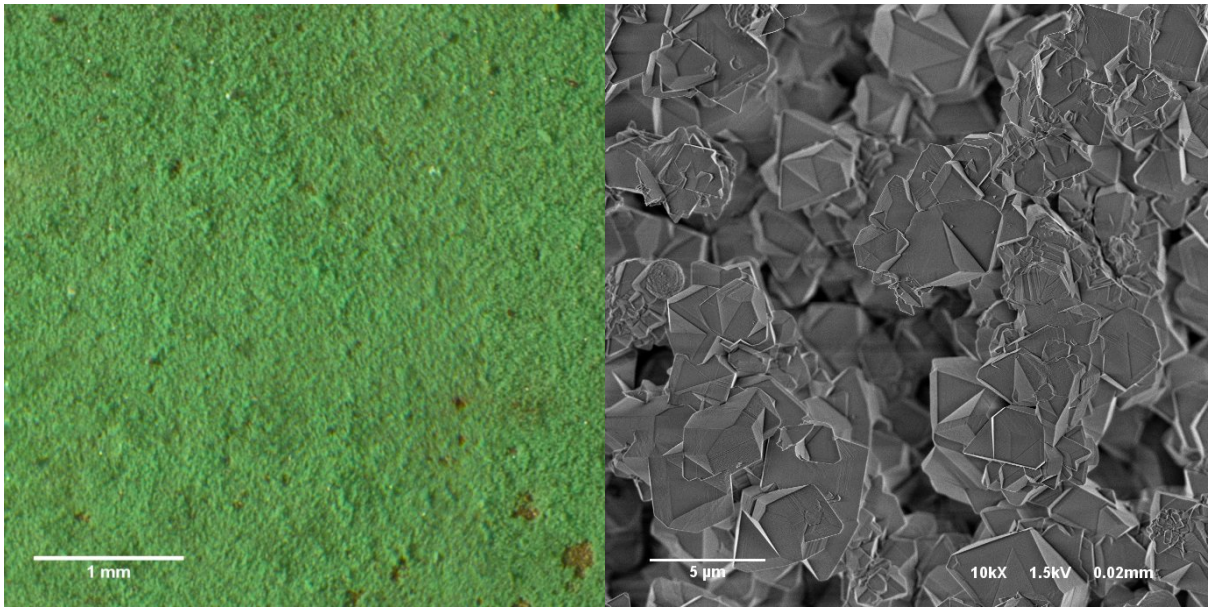

(a) (b)

FIGURE 3.16: Image (a) and FESEM micrograph (b) of the paratacamite patina sample before laser cleaning.

X-ray micro-diffraction analysis of the sample (Figure 3.17) indicates that the patina is conformed of a layer of cuprite with a paratacamite crystals layer on top, and the presence of small amounts of copper oxide and tolbachite. Peaks corresponding to copper, from the substrate and x-ray source, can also be identified in the diffractogram. This is in accordance with the procedure used to obtain the artificial patina.

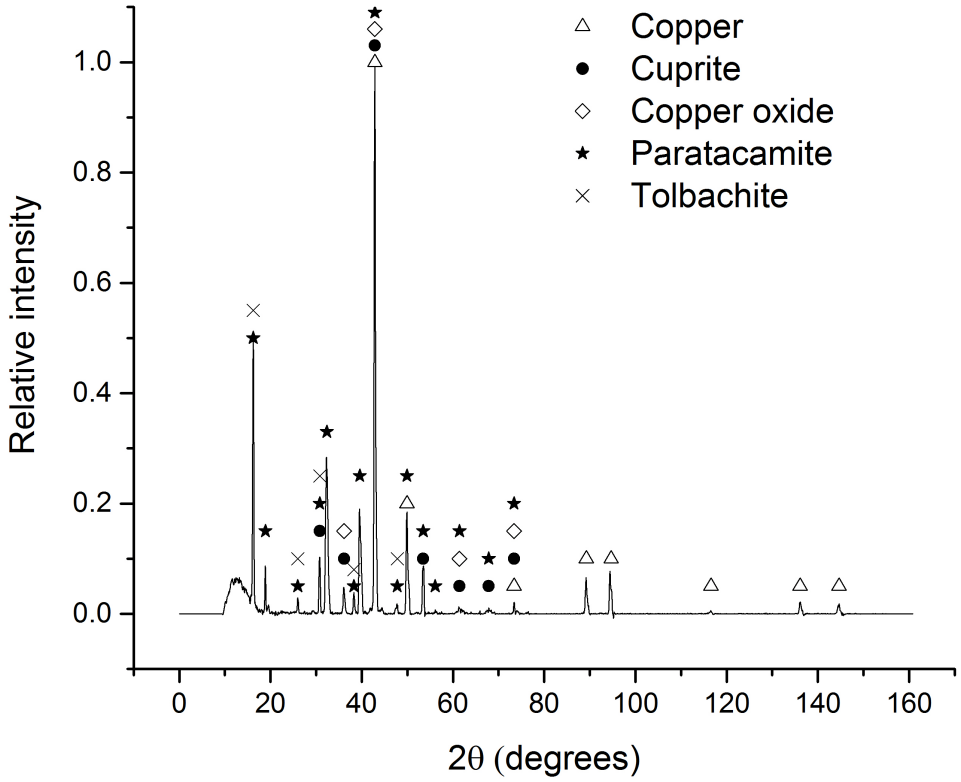

FIGURE 3.17: X-ray diffractogram of the paratacamite patina sample with labelled peaks for paratacamite, copper, cuprite, tolbachite, and copper oxide.

The majority of laser cleaning tests performed on this sample were too intense, and resulted in melting of either the corrosion layer or the substrate itself. Figure 3.18 shows an example of this. The image seen in Figure 3.18a is of test area A2 after cleaning, next to a FESEM micrograph, where evidence of melting of the patina is easily seen (Figure 3.18b). Confocal microscopy measures of this area show that the corrosion products layer has been reduced in thickness by 87.50 %, so a partial melting of the substrate cannot be discarded.

Paratacamite crystals present a high transparent/translucent behaviour upon IR irradiation. This means that the crystals, specially the bigger ones, do not absorb a high amount of the energy applied. So, despite the lower melting point of this material (250 °C), when compared to cuprite ($\sim$ 1200 °C), and the much lower porosity, less damage and melting are seen for this sample than for the cuprite layer with the same laser conditions. This means that the paratacamite presents a higher ablation threshold than that of cuprite.

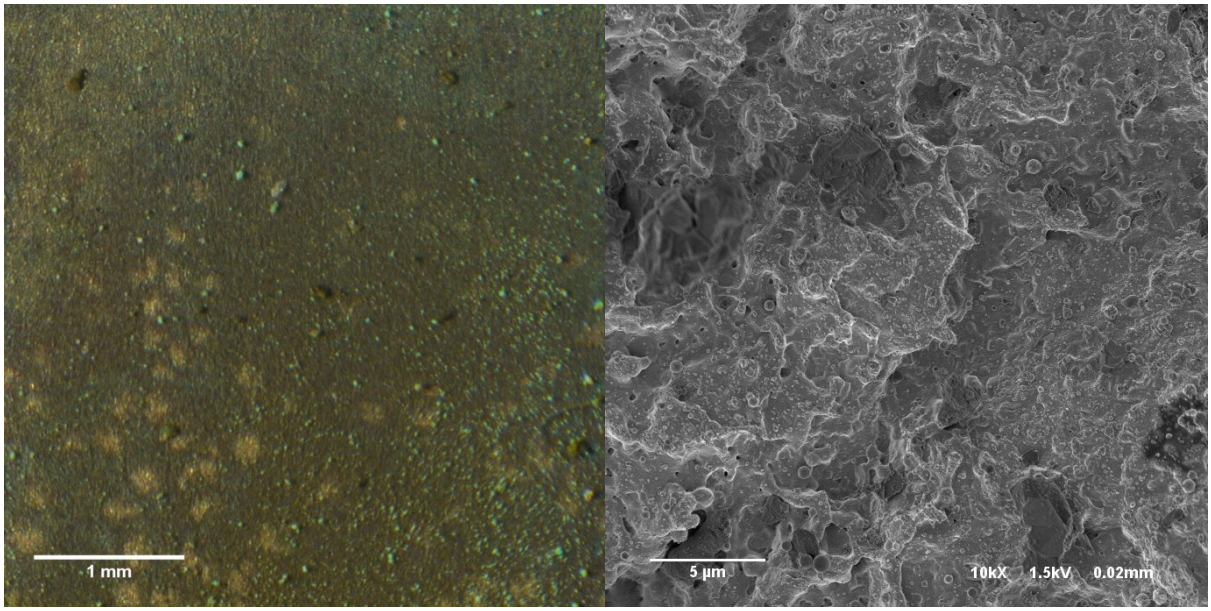

(a) (b)

FIGURE 3.18: Image (a) and FESEM micrograph (b) of test area A2 of the paratacamite patina sample after laser cleaning.

Areas submitted to the lowest fluence values show less visible damage than the rest. For this reason, and for purposes of comparison of cleaning tests across samples, areas C1 (Figure 3.19) and B2 (Figure 3.20) were analysed by μXRD and confocal microscopy. Although the paratacamite layer has been partially removed, the crystals can still be seen in the FESEM micrographs (Figures 3.19b and 3.20b), but areas where the patina is thinner or has detached from the substrate still show signs of melting (Figure 3.19c). In this case, we observe less melting, and the removal of the layer presents a significant photophysical component. Since paratacamite crystals are transparent to IR radiation, any real absorption of the laser energy only

occurs around the grain borders by scattering mechanisms, so melting starts in these areas. This, combined with the mechanical shock wave related to the laser plasma plume during the ablation mechanisms, favours the intergranular breaking and ejection of the material.

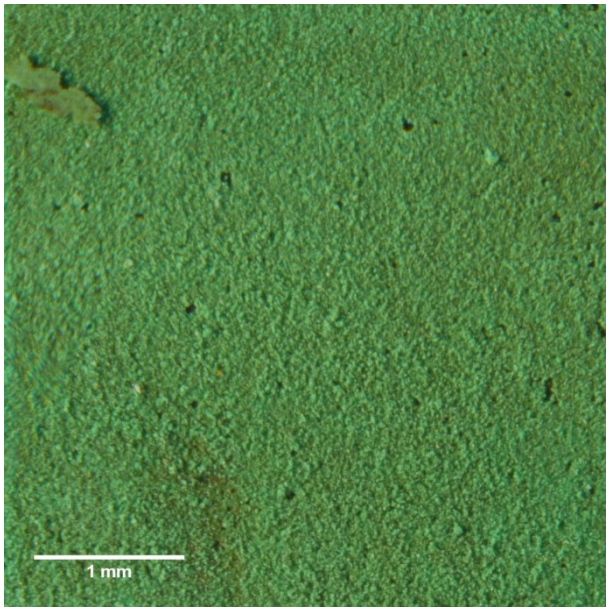

(a)

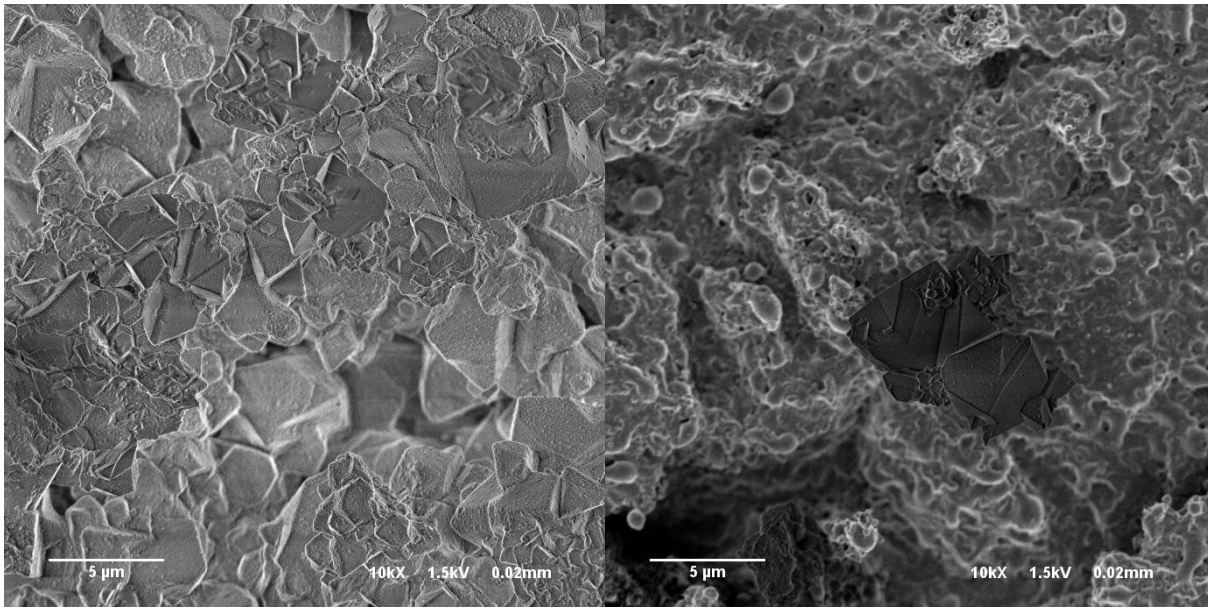

(b) (c)

FIGURE 3.19: Image (a) and FESEM micrographs of the crystals (b) and melted substrate (c) areas found on test area C1 of the paratacamite patina sample after laser cleaning.

On the x-ray diffractogram obtained after cleaning of test area C1 (Figure 3.21), peaks corresponding to copper and copper oxides have a higher relative intensity than their counterparts

in the original patina (Figure 3.17). This can be interpreted as a partial removal of the paratacamite layer, since a thinner corrosion layer means that x-rays can penetrate deeper into the substrate, hence increasing the intensity of the copper peaks.

The diffractogram of area B2 (Figure 3.22) shows that most of the patina has been removed after cleaning, as can be seen by the high intensity of the peaks corresponding to copper, i.e. the substrate, and diminished intensity of peaks corresponding to paratacamite and copper oxides, while tolbachite peaks have virtually disappeared.

Confocal microscopy was used to determine the changes on the surface and amount of material removed with each cleaning treatment, Table 3.3 shows the average thickness of the patina in different areas. The original patina had an average thickness of 40 µm, around 10 µm were removed after treatment in area B2, and 5 µm in area C1. The changes on the surface after treatments can be seen in Figure 3.23, where the first half of the plot, along the x-axis, corresponds to the original surface and the second half to the treated area of test areas C1 (Figure 3.23a) and B2 (Figure 3.23b).

TABLE 3.3: Average thickness of paratacamite patina layer.

Area	Patina	A2	C1	B2
Average thickness (µm)	40	5	35	30

A partial removal of the paratacamite layer and removal of tolbachite can be assumed from

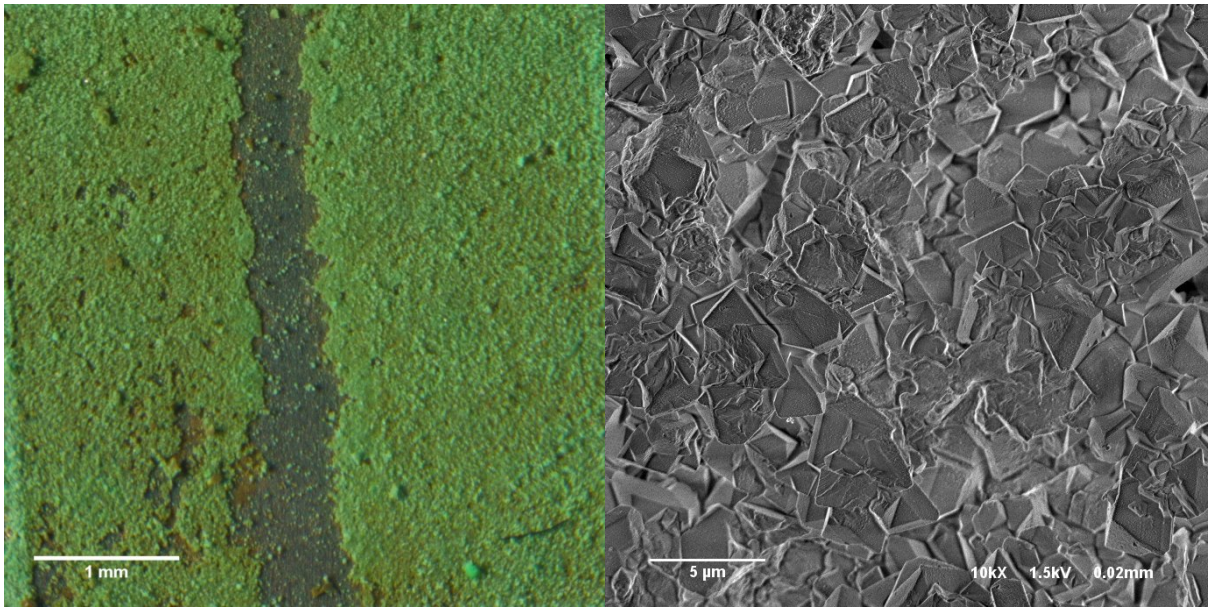

(a) (b)

FIGURE 3.20: Image (a) and FESEM micrograph (b) of test area B2 of the paratacamite patina sample after laser cleaning.

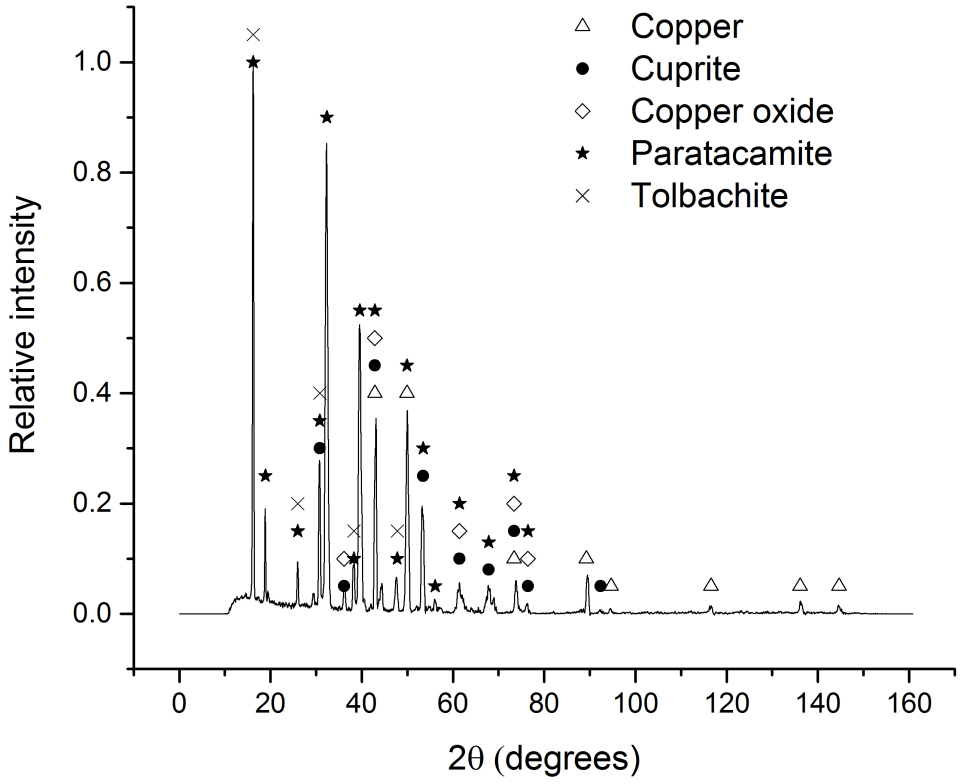

FIGURE 3.21: X-ray diffractogram of test area C1 of the paratacamite patina sample with labelled peaks for paratacamite, copper, cuprite, tolbachite, and copper oxide.

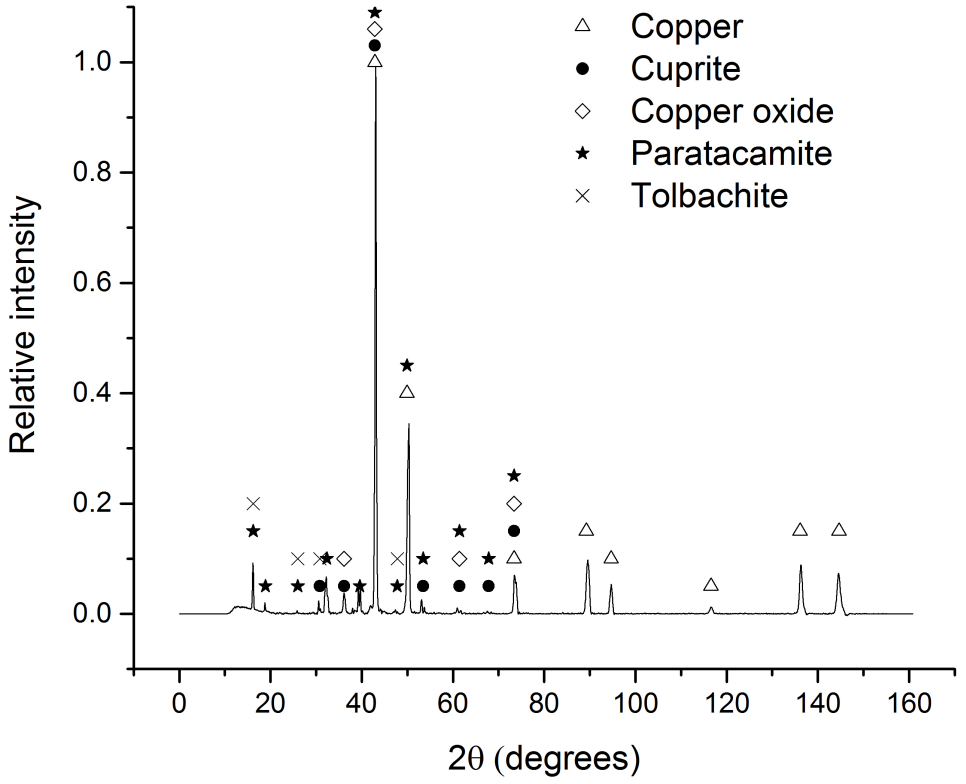

FIGURE 3.22: X-ray diffractogram of test area B2 of the paratacamite patina sample with labelled peaks for paratacamite, copper, cuprite, tolbachite, and copper oxide.

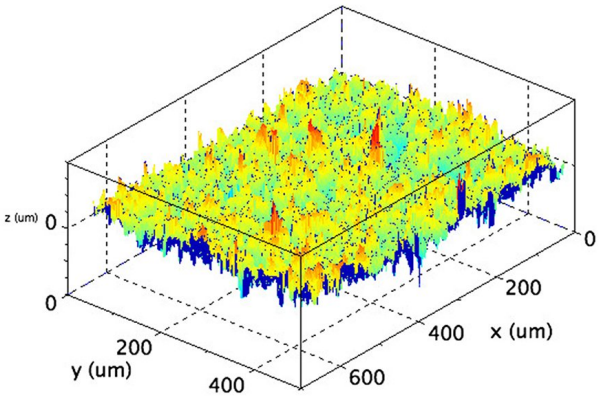

(a)

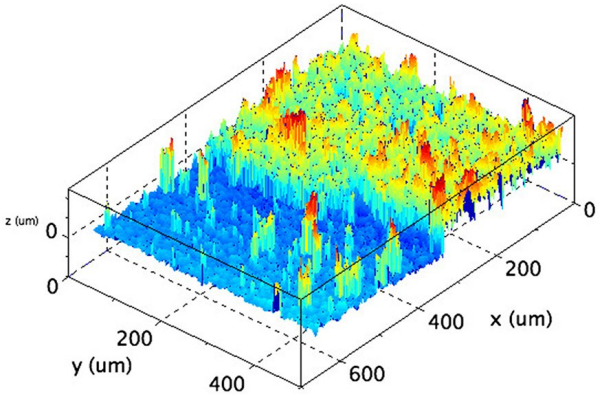

(b)

FIGURE 3.23: Confocal microscopy surface plots of test areas C1 (a) and B2 (b) of the paratacamite patina sample. The surface of the original patina is plotted starting from 0 on the x-axis, the second half of the plot represents the treated area.

these results. However, the treated areas show signs of melting of the cuprite layer. In this instance, the morphology observed under the field emission scanning electron microscopy (Figures 3.18b and 3.19c) in accordance to the one usually seen for melted inorganic crystals.

3.5 Malachite

The third tested sample, shown in Figure 3.24 has a patina composed of a cuprite layer with green malachite and nantokite crystals spread along the sample (Figure 3.24a). FESEM images of the cuprite layer and a crystal are shown in Figures 3.24b and 3.24c, respectively.

The composition of the patina was confirmed by μXRD. The corresponding diffractogram, shown in Figure 3.25, evidences the presence of the cuprite and malachite/nantokite crystals, and the copper peaks from the substrate and source can also be distinguished.

FESEM images of the treated areas show that the applied treatments, for the most part, have melted the patina where no crystals are present, while the malachite and nantokite crystals were removed, burned or remain unaffected. An example, from test area A2, can be seen in Figure 3.26, where images of the area after treatment (Figure 3.26a) and FESEM micrographs (Figures 3.26b and 3.26c) of the remaining patina, are shown. This corrosion layer exhibits a behaviour that is a combination of the ones observed on the previously discussed cuprite and paratacamite crystals layers. For the cuprite layer, we expect to observe the same behaviour, a slightly densification of the outer parts of the layer due to melting of the patina. In the case of the malachite and nantokite crystals, these exhibit the same transparency to IR radiation as paratacamite, or even a higher one, due to the larger size of the crystals. Bigger crystals lead to less intergranular scattering so it is observed that many of the crystals do not suffer any modification and remain unaltered even on the melted cuprite layer.

Areas C1 and B2, the images and FESEM micrographs of which are shown in Figures 3.27 and 3.28, respectively, were analysed by μXRD in areas with and without visible crystals.

In areas without visible crystals (Figures 3.29a and 3.30a) the patina was partially removed, as can be seen by the disappearance or lowered intensity of peaks corresponding to malachite and nantokite in the μXRD diffractograms. Areas where crystals were present (Figures 3.29b and 3.30b) show no significant difference in composition from the original patina, although they were altered visually Figures 3.27a and 3.28a.

Although the parameters used in tests C1 and B2 could be effective on malachite and nantokite crystals, the applied power is still too intense for cuprite, as can be seen from the melting of this layer, which shows morphological features characteristic of melted inorganic crystals when analysed by FESEM (Figures 3.26c, 3.27b and 3.28b).

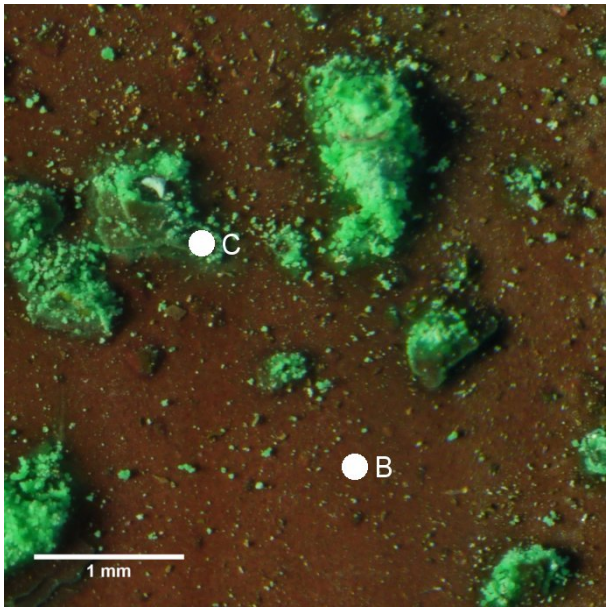

(a)

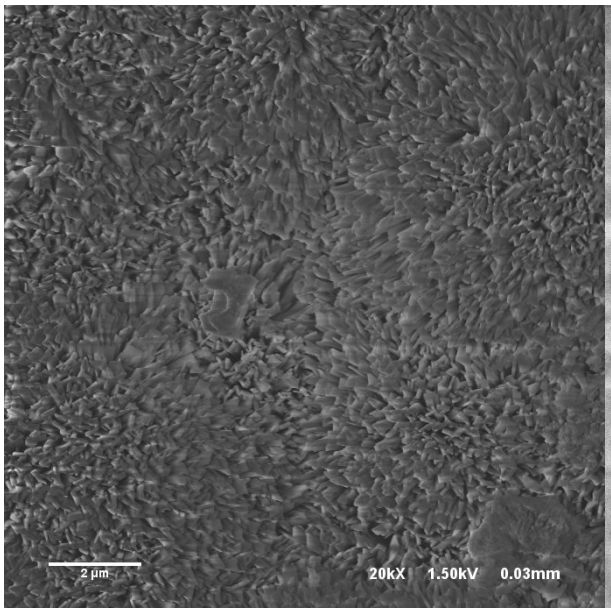

(b)

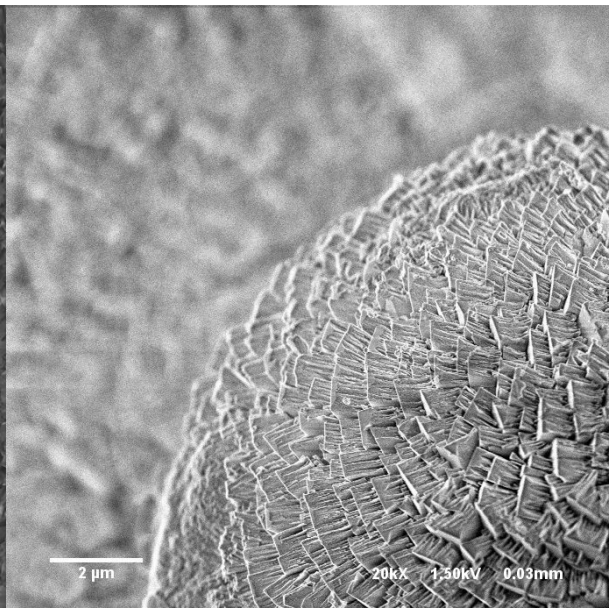

(c)

FIGURE 3.24: Image (a) and FESEM micrographs of the cuprite layer (b) and malachite crystals (c) of the paratacamite patina sample before laser cleaning.

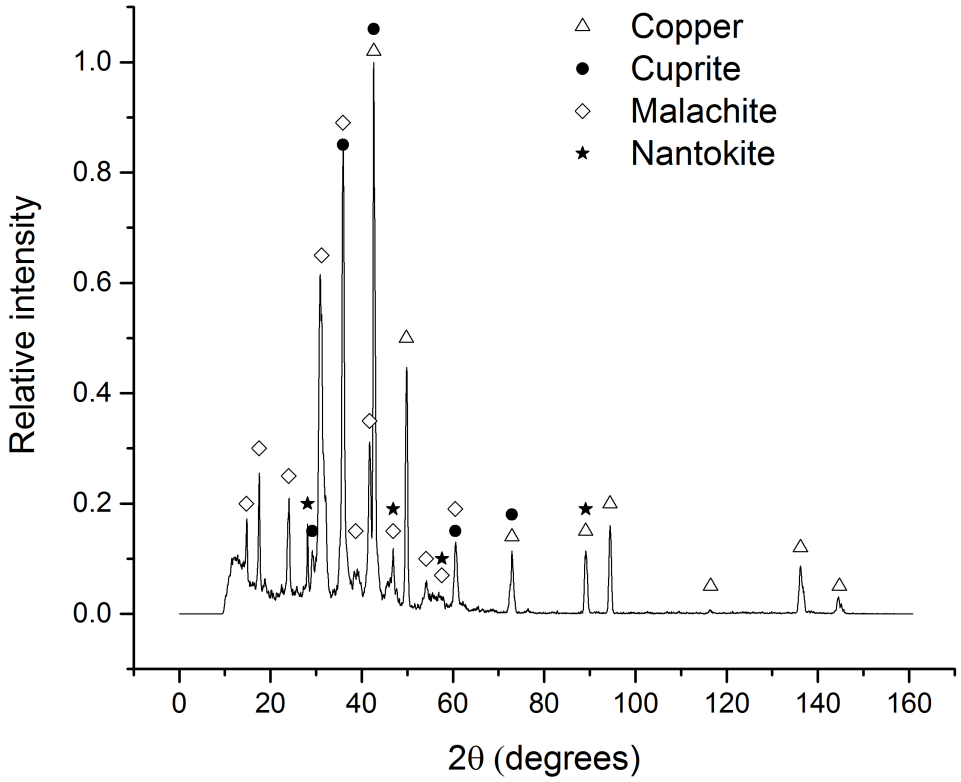

FIGURE 3.25: X-ray diffractogram of the malachite patina with labelled peaks for cuprite, malachite, nantokite, and copper.

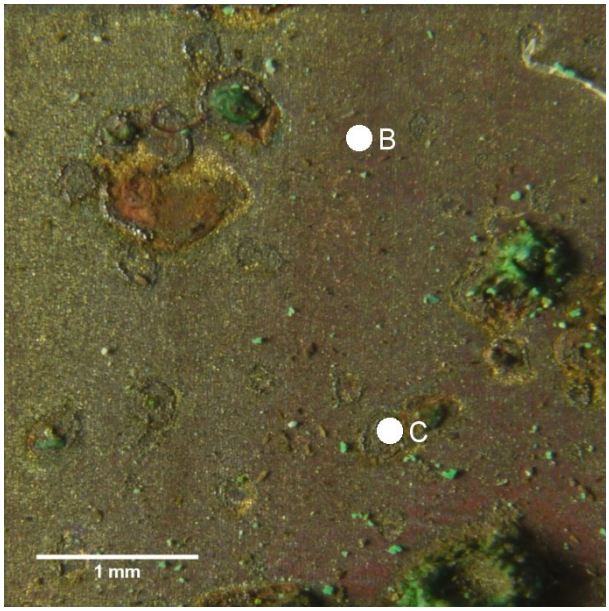

(a)

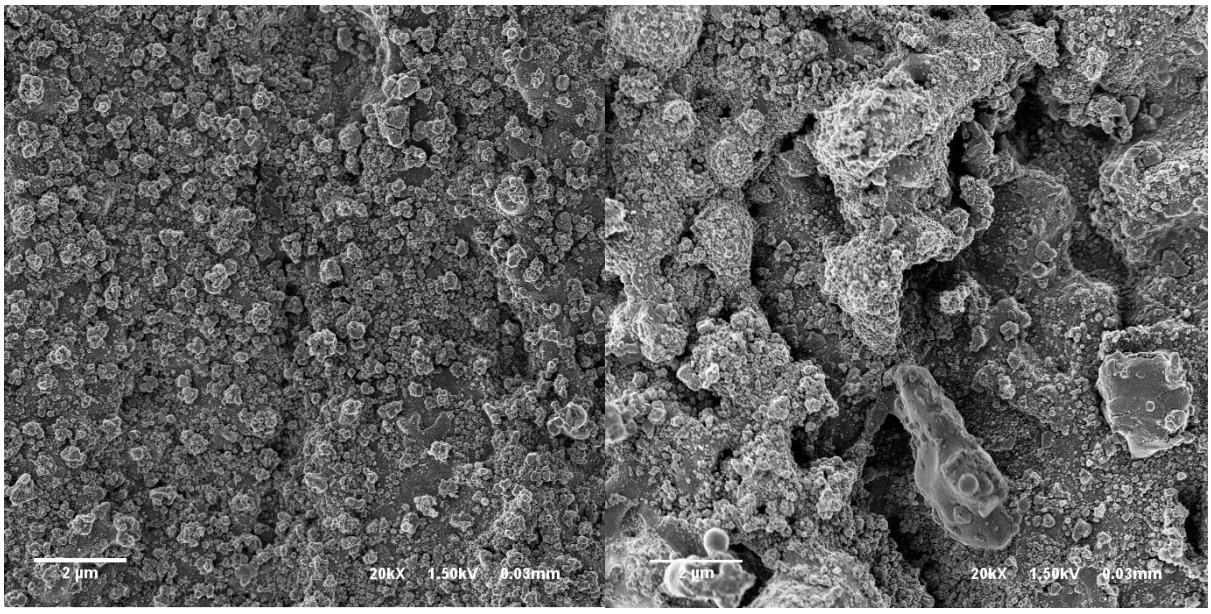

(b) (c)

FIGURE 3.26: Image (a) and FESEM micrographs of the cuprite corrosion layer, (b) and malachite crystals (c), of test area A2 of the malachite patina sample after laser cleaning.

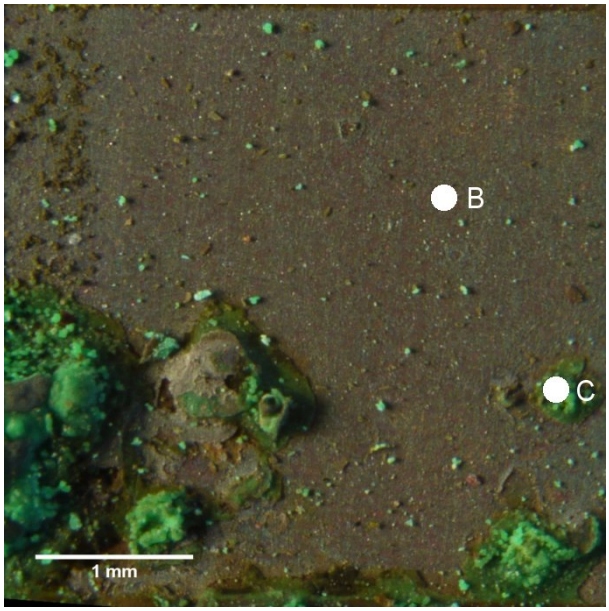

(a)

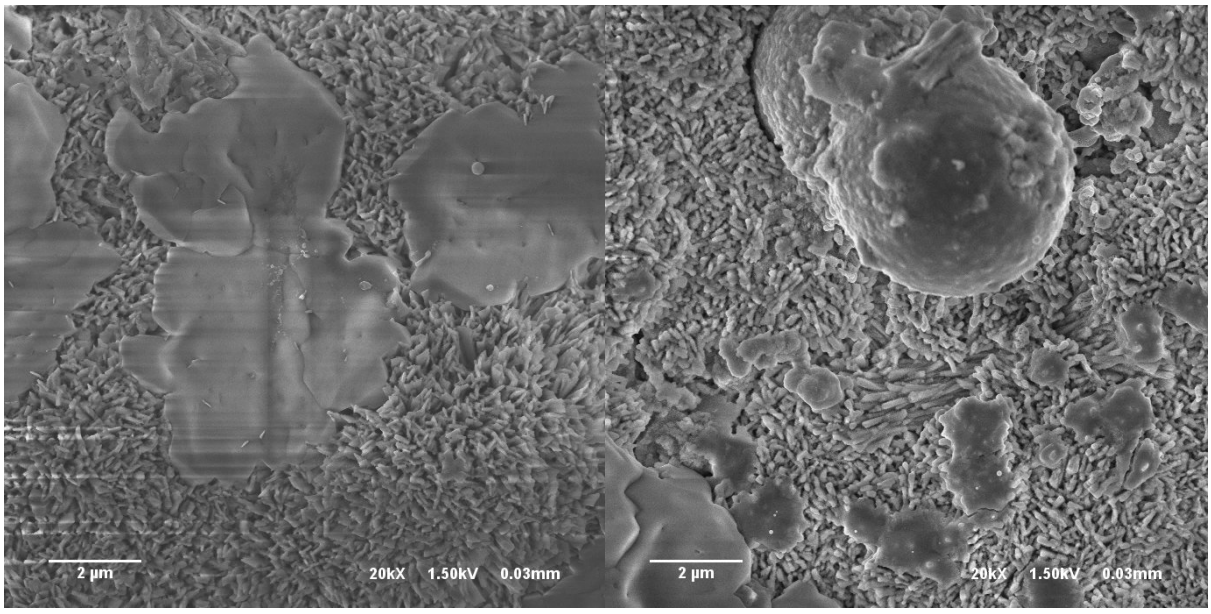

(b) (c)

FIGURE 3.27: Image (a) and FESEM micrographs of the cuprite layer (b) and malachite crystals (c) of test area C1 of the malachite patina sample after laser cleaning.

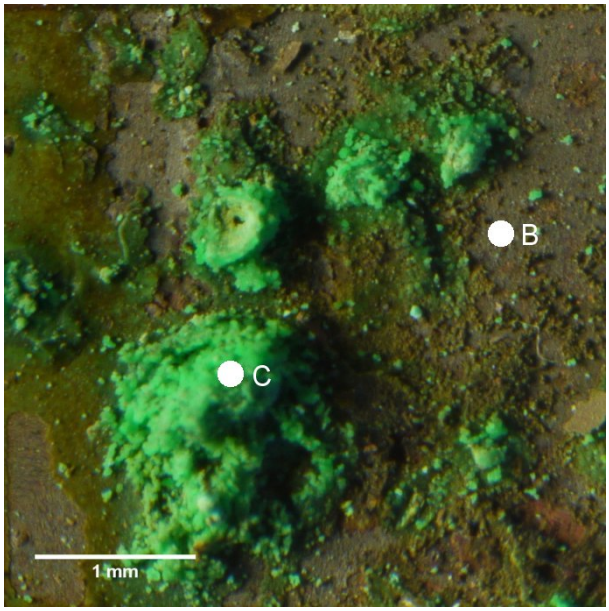

(a)

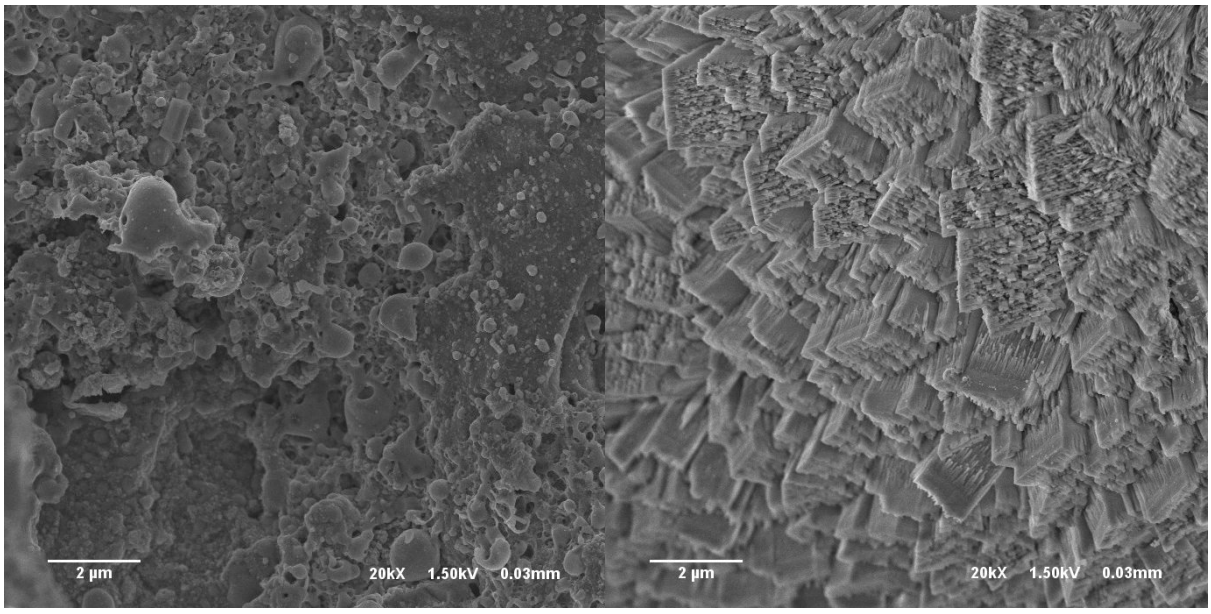

(b) (c)

FIGURE 3.28: Image (a) and FESEM micrographs of the cuprite layer (b) and malachite crystals (c) of test area B2 of the malachite patina sample after laser cleaning.

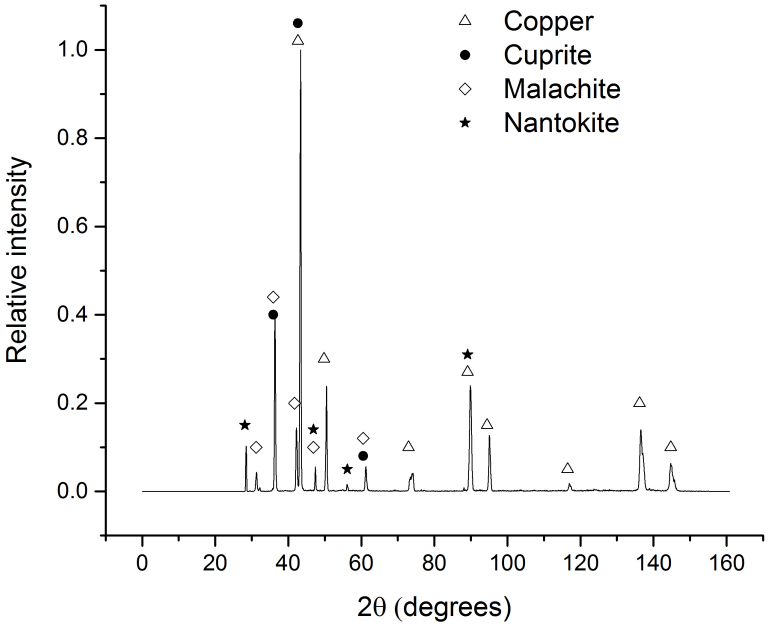

(a)

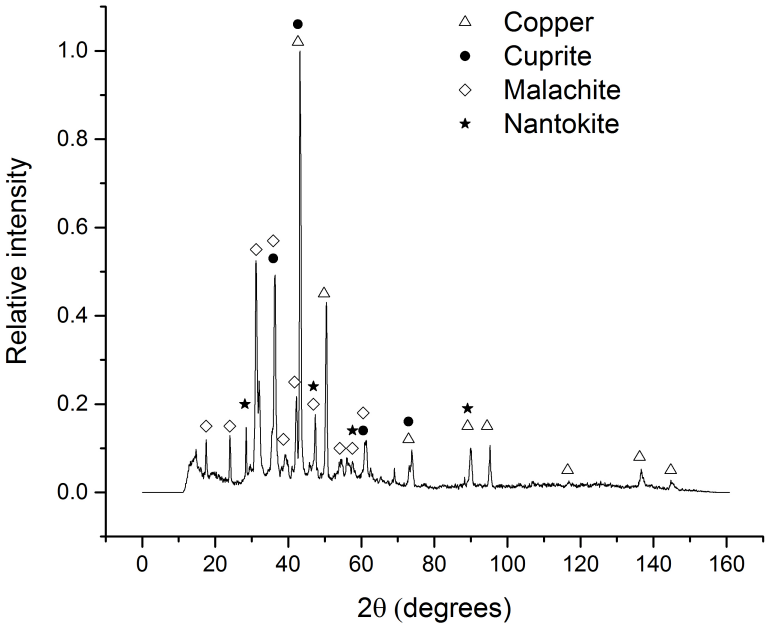

(b)

FIGURE 3.29: X-ray diffractograms of the cuprite layer (a) and malachite crystals (b) in test area C1 of the malachite patina sample with labelled peaks for cuprite, malachite, nantokite, and copper.

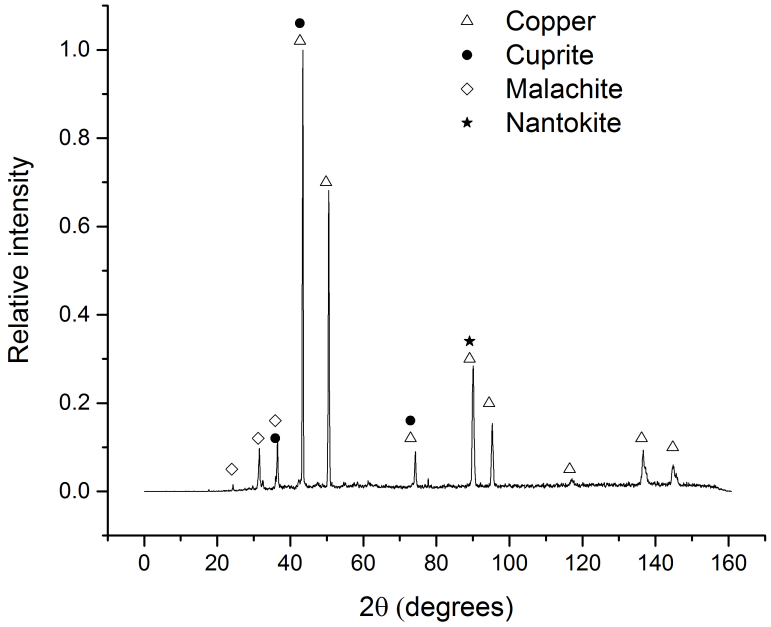

(a)

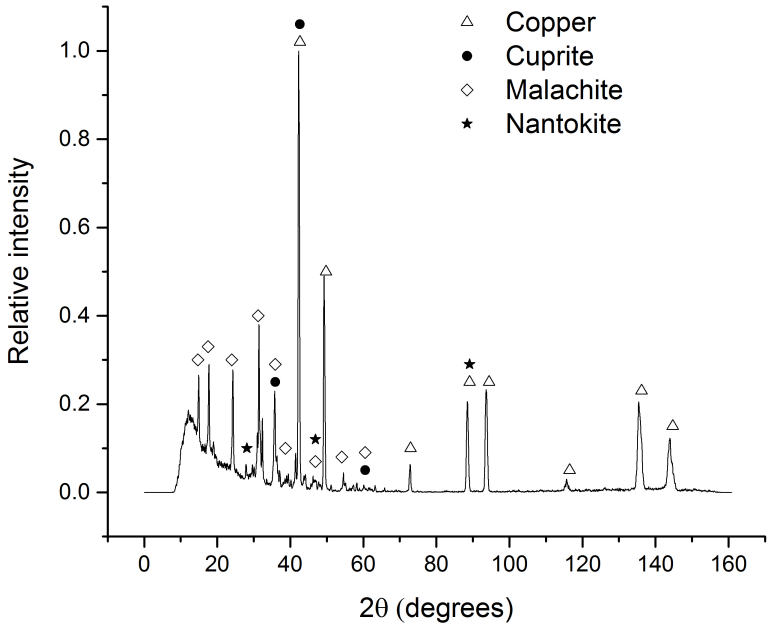

(b)

FIGURE 3.30: X-ray diffractograms of the cuprite layer (a) and malachite crystals (b) in test area B2 of the malachite patina sample with labelled peaks for cuprite, malachite, nantokite, and copper.

3.6 Conclusions and future experiments

Considering the results obtained with these tests, we have observed that the laser damage thresholds, obtained in previous studies, for these materials and used in this instance are too aggressive on the cuprite layer, which, ideally, should be preserved. This can be explained by the high heterogeneity of these layers specially during their formation. Different thickness, porosity values, and colour may lead to different responses to laser irradiation. Hence, it is clear that different protocols should be developed for each kind of patina present in the reference samples, and real artefacts should be characterised previous to any treatment to determine the best course of action.

The main obstacle for this process is that the material that must be preserved, i.e. the cuprite layer, shows lower ablation thresholds than the undesired layers. This makes the proper elimination of dangerous corrosion products, such as paratacamite and malachite, very difficult without damaging the desired layers.

In future experiments, fluences below $1.5\,J/cm^2$, i.e. the lowest value used in this set, should be used in order to avoid melting of the cuprite crystals, and other parameters, such as the pulse overlap, should be considered when designing the cleaning protocols. Additionally, cross-section analysis of the patinas would be helpful in determining if the substrate is being affected by the laser treatments.

The use of a UV laser to remove the paratacamite, malachite and nantokite crystals may be a solution, since these compounds, as well as cuprite, have a different absorbance in the UV-Vis region than they do in the IR region. Further information on absorbance values can be obtained by absorption spectroscopy.

The chemical interaction between the laser and the patinas should also be investigated, since it's possible that some of the corrosion products are being transformed during the cleaning treatments.

Chapter 4

Plasma cleaning

This chapter gives an introduction to glow discharge processes and their use in the cleaning of cultural heritage artefacts (Section 4.1). A discussion on the plasma cleaning processes performed on artificially corroded copper samples (Section 4.3) and their suitability for use on cultural heritage artefacts follows. Future works that can be done to optimise the process are discussed in the conclusions (Section 4.4).

4.1 Plasma discharge processes for cleaning

Low pressure plasmas exhibit some major advantages for their application in the field of conservation of Cultural Heritage, especially metals. They are dry processes, easily performed at room temperature, so they guarantee the preservation of metallurgical features; they can be applied directly on the exterior or the interior of complex shapes; plasma etching can be controllable and selective at the nanoscale and can be very mild; plasma deposition can produce very thin coatings with customizable structure having a minimal effect on the appearance of the surface, yet very good corrosion protection (Grassini et al., 2007). The working principles of D.C. and RF glow discharges, and their application in plasma etching and cleaning, are explained in this section.

4.1.1 Principles of plasma discharge processes

Plasmas are ionised gases. They consist of positive (and negative) ions and electrons, as well as neutral species. The ionisation degree can vary from high (100 %, fully ionised gases) to very low values (10×10^{-4} % to 10×10^{-6} %, partially ionised gases).

Besides the astroplasmas, which are omnipresent in the universe, we can also distinguish two main groups of laboratory plasmas, i.e. high-temperature or fusion plasmas, and the so-called low-temperature plasmas or gas discharges. In general, a subdivision can be made between plasmas which are in thermal equilibrium and those which are not in thermal equilibrium. Thermal equilibrium implies that the temperature of all species (electrons, ions, neutral species) is the same. This is, for example, true for stars, as well as for fusion plasmas. High temperatures are required to form these equilibrium plasmas, typically ranging from 4000 K to

20 000 K (M. A. Lieberman & Lichtenberg, 2005). On the other hand, interstellar plasma matter is typically not in thermal equilibrium. This means that the temperatures of the different plasma species are not the same; more precisely, that the electrons are characterized by much higher temperatures than the heavy particles.

This subdivisions can also be used for gas discharge plasmas, and are typically related to the pressure in the plasma. A high gas pressure implies many collisions in the plasma (i.e. a short collision mean free path, compared to the discharge length), leading to an efficient energy exchange between the plasma species, and hence, equal temperatures. A low gas pressure, on the other hand, results in only a few collisions in the plasma (i.e. a long collision mean free path compared to the discharge length), and consequently, different temperatures of the plasma species due to inefficient energy transfer.

In recent years, the field of gas discharge plasma applications has rapidly expanded. This is due, among other things, to the large chemical freedom offered by the non-equilibrium aspects of the plasma. This wide variety of chemical non-equilibrium conditions is possible, since (external control) parameters can easily be modified, such as: the chemical input (working gas; this defines the different species in the plasma: electrons, atoms, molecules, ions, radicals, clusters); the pressure (ranging from approx. 0.10 Pa to atmospheric pressure); the electromagnetic field structure (typically externally imposed, but it can also be modified by the plasma species; these electric and/or magnetic fields are used to accelerate, heat, guide and compress the particles); the discharge configuration (e.g. with or without electrodes, and discharge volume); and/or the temporal behaviour (e.g. pulsing the plasma).

High pressure discharges, which are characterized by rather high temperatures, are typically used for applications where heat is required, such as for cutting, spraying, welding or, as in the analytical ICP, for the evaporation of an analyte material. Low pressure plasmas, on the other hand, are typically used for applications where heat is not desirable, such as for etching or the deposition of thin layers. The heavy particle temperature is low (often not much higher than room temperature), but the electrons are at much higher temperatures, because they are light and easily accelerated by the applied electromagnetic fields. The high electron temperature gives rise to inelastic electron collisions, which, on the one hand, sustain the plasma (e.g. electron impact ionisation) and on the other hand, result in a 'chemically-rich' environment. The electrons are, therefore, considered to be the 'primary agents' in the plasma. Most of the applications, on the other hand, result from the heavy particle kinetics (e.g. sputtering, deposition) (Bogaerts, Neyts, Gijbels, & van der Mullen, 2002).

Direct current glow discharges

When a sufficiently high potential difference is applied between two electrodes placed in a gas, the latter will break down into positive ions and electrons, giving rise to a gas discharge. The mechanism of the gas breakdown can be explained as follows: a few electrons are emitted

from the electrodes due to the omnipresent cosmic radiation. Without applying a potential difference, the electrons emitted from the cathode are not able to sustain the discharge. However, when a potential difference is applied, the electrons are accelerated by the electric field in front of the cathode and collide with the gas atoms. The most important collisions are the inelastic collisions, leading to excitation and ionisation. The excitation collisions, followed by de-excitations with the emission of radiation, are responsible for the characteristic name of the 'glow' discharge. The ionisation collisions create new electrons and ions. The ions are accelerated by the electric field toward the cathode, where they release new electrons by ion induced secondary electron emission. The electrons give rise to new ionisation collisions, creating new ions and electrons. These processes of electron emission at the cathode and ionisation in the plasma make the glow discharge a self-sustaining plasma.

Another important process in the glow discharge is the phenomenon of sputtering, which occurs at sufficiently high voltages. When the ions and fast atoms from the plasma bombard the cathode, they not only release secondary electrons, but also atoms of the cathode material, which is called sputtering. This is the basis of the use of glow discharges for analytical spectrochemistry. Indeed, the material to be analysed is then used as the cathode of the glow discharge, which is being sputtered by the plasma species. Alternatively, the sputtered atoms can also diffuse through the plasma and they can be deposited on a substrate (often placed on the anode); this technique is used in materials technology, e.g. for the deposition of thin films. A schematic picture of the elementary glow discharge processes described above is presented in Figure 4.1. When a constant potential difference is applied between the cathode and anode, a continuous current will flow through the discharge; giving rise to a direct current (d.c.) glow discharge. It should be mentioned that in a d.c. glow discharge the electrodes play an essential role for sustaining the plasma by secondary electron emission. When a time-varying potential difference is applied, as in a capacitively coupled radio-frequency (rf) discharge (Section 4.1.1), the role of the electrodes becomes less important, because the electrons can oscillate in the plasma between the two electrodes, by the time-varying electric field. Eventually, the role of the electrodes becomes even negligible, giving rise to electrodeless discharges, as in the case of ICP (Bogaerts et al., 2002).

The potential difference applied between the two electrodes of the glow discharge does not drop linearly between cathode and anode, but drops almost completely in the first millimetres in front of the cathode. This is schematically illustrated in Figure 4.2. This region is called the "cathode dark space" (CDS) or "cathode sheath", and it is dark because the strong electric field, associated with the potential drop, accelerates the electrons emitted from the cathode to energies which are too high for efficient ionisation and excitation. Moreover, this region is characterised by a positive space charge, because of the much higher mobility of the electrons compared with positive ions. The major part of the glow discharge is filled with a region called "negative glow" (NG), which is characterised by a very weak electric field, or in other words a

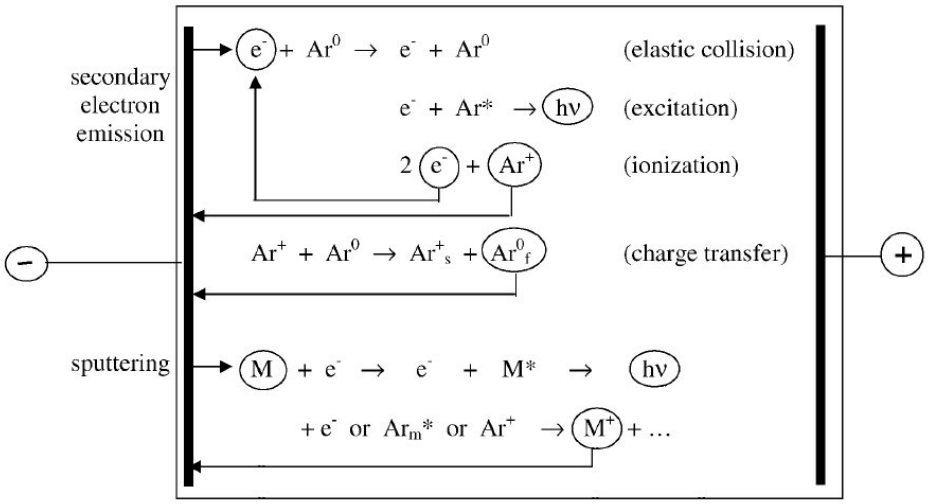

FIGURE 4.1: Schematic overview of the most important basic processes that take place in glow discharge plasmas. The subscripts f and s stand for "fast" and "slow", and the superscripts 0 and * denote the ground state and excited states, respectively. Ar^*_m symbolizes the Ar metastable atoms (Bogaerts, 2007).

constant and slightly positive potential, called the "plasma potential". This region has nearly charge neutrality (because of equal number densities of electrons and positive ions) and high luminosity (because the electrons have lost energy by collisions, and have now suitable energy for ionisation and excitation).

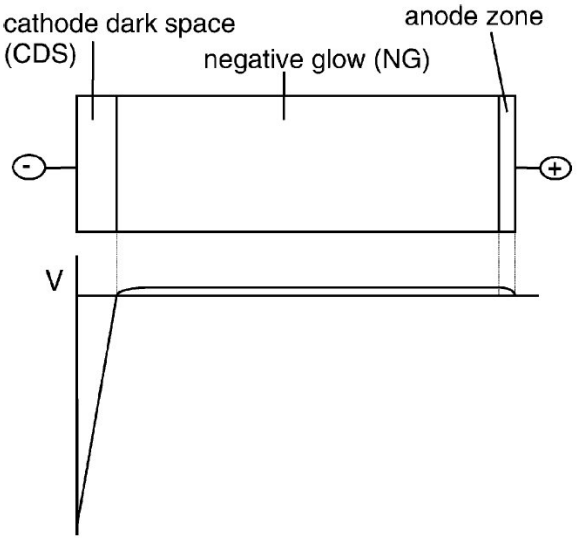

FIGURE 4.2: Schematic picture of the three spatial regions typically present in a glow discharge, and the characteristic potential distribution throughout the discharge (Bogaerts, 2007).

When the distance between anode and cathode is very long, such as in glow discharges used for laser applications and fluorescent lamps, two more regions can be distinguished between the negative glow and the anode, i.e., the so-called Faraday dark space and the positive column, where a slightly negative electric field ensures that sufficient electrons can reach the anode, necessary to maintain the electrical current. However, in most glow discharges, the distance between cathode and anode is rather short, so that the negative glow is only followed by a short "anode zone"(AZ), in which the positive plasma potential returns back to zero at the grounded anode. The length of the different regions, especially of the CDS, depends also on pressure: a higher pressure results in shorter regions, so that for a fixed distance between cathode and anode, a Faraday dark space and positive column can be formed.

A d.c. glow discharge can operate over a wide range of discharge conditions. The pressure can vary from below 1 Pa to atmospheric pressure. It should, however, be realised that the product of pressure and distance between the electrodes (pD) is a better parameter to characterize the discharge (as mentioned above). For instance, at lower pressure, the distance between cathode and anode should be longer to create a discharge with properties comparable to those of high pressure with small distance. The voltage is mostly in the range between 300 and 1500 V, but for certain applications it can increase to several kV. The current is generally in the mA range. The discharge can operate in a rare gas (most often argon or helium) or in a reactive gas (N_2, O_2, H_2, etc.), as well as in a mixture of these gases (Bogaerts et al., 2002).

Capacitively coupled (cc) radio-frequency (rf) glow discharges

To sustain a d.c. glow discharge, the electrodes have to be conducting. When one or both of the electrodes are non-conductive, e.g. when the glow discharge is used for the spectrochemical analysis of non-conducting materials or for the deposition of dielectric films, where the electrodes become gradually covered with insulating material, the electrodes will be charged up due to the accumulation of positive or negative charges, and the glow discharge will extinguish. This problem is overcome by applying an alternating voltage between the two electrodes, so that each electrode will act alternately as the cathode and anode, and the charge accumulated during one half-cycle will be at least partially neutralized by the opposite charge accumulated during the next half-cycle.

The frequencies generally used for these alternating voltages are typically in the radiofrequency (rf) range (1 kHz – 10^3 MHz; with a most common value of 13.56 MHz). The frequency should be high enough so that half the period of the alternating voltage is less than the time during which the insulator would charge up. Otherwise, there will be a series of short-lived discharges with the electrodes successively taking opposite polarities, instead of a quasi-continuous discharge. It can be calculated that the discharge will continue when the applied frequency is above 100 kHz (Chapman, 1980). In practice, many rf GD processes operate

at 13.56 MHz, because this is a frequency allotted by international communications authorities at which one can radiate a certain amount of energy without interfering with communications.

At this point, it is important to note that the term 'capacitively coupled' refers to the way of coupling the input power into the discharge, i.e. by means of two electrodes and their sheaths forming a kind of capacitor. At the typical rf frequencies, the electrons and ions have a totally different behaviour, which can be explained by their different masses. The light electrons can follow the instantaneous electric fields produced by the applied rf voltage. The ions, on the other hand, can follow the field in the sheath if the frequency is less than the ion plasma frequency. Because the ion plasma frequency is inversely proportional with mass, light ions can see the field variations at typical rf frequencies, whereas heavy ions can only follow time-averaged electric fields.

Another important aspect of cc rf discharges, which also results from the differences in mass between electrons and ions, is the phenomenon of self-bias. The self-bias or d.c.-bias is formed (i) when both electrodes differ in size, and (ii) when a coupling capacitor is present between the rf power supply and the electrode, or when the electrode is non-conductive (because it then acts as a capacitor). When a certain voltage is applied over the capacitor formed by the electrodes, the voltage over the plasma will initially have the same value as the applied voltage. When the applied voltage is initially positive, as in Figure 4.3, the electrons will be accelerated toward the electrode. Hence, the capacitor will be rapidly charged up by the electron current, and the voltage over the plasma will drop. When the applied potential changes polarity after one half-cycle, the voltage over the plasma changes with the same amount (i.e. twice the amplitude of the applied voltage). The capacitor will now be charged up by the ion current, and the voltage over the plasma will, therefore, drop as well, but this second drop is less pronounced, because of the much lower mobility (due to the higher mass) of the ions, and hence, the lower ion flux. At the next half-cycle, the applied potential, and hence also the voltage over the plasma, again changes polarity. The voltage over the plasma drops again more rapidly, because the capacitor is again charged up by the electron flux. This process repeats itself, until the capacitor is finally sufficiently negatively charged so that the ion and electron fluxes, integrated over one rf cycle, are equal to each other. This results in a time-averaged negative d.c. bias at the rf-powered electrode (see dashed line in Figure 4.3). It should be mentioned that the same phenomenon happens at the grounded electrode, but the effect is much smaller (Bogaerts et al., 2002).

Because of the negative d.c. bias, the ions continue to be accelerated toward the rf-powered electrode, and they can, therefore, cause sputtering of the rf-electrode material. In fact, the cc rf discharge often resembles a d.c. glow discharge, with a similar subdivision in different regions, similar operating conditions, and with similar processes occurring in the plasma.

For plasma processing applications, cc rf discharges, also called 'rf-diodes', consist, in the simplest case, of a vacuum chamber containing two planar electrodes separated by a distance

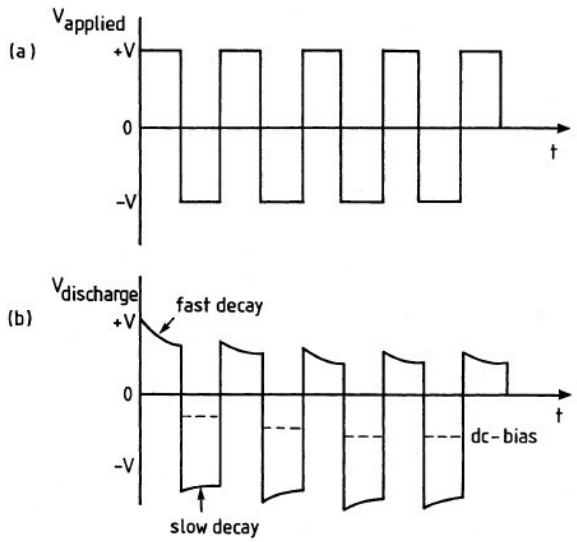

FIGURE 4.3: Development of self-bias (d.c.-bias) in a cc rf discharge, in the simplified case of a rectangular pulse: (a) applied voltage; and (b) resulting voltage over the discharge as a function of time, and resulting d.c.-bias (dashed line) (Bogaerts et al., 2002).

of several cm. The substrate is normally placed on one electrode. The typical driving voltage is 100 V to 1000 V. The pressure is in the range of 1 Pa to 100 Pa, and the electron density (plasma density) is of the order of $10^9/\text{cm}^3$ to $10^{11}/\text{cm}^3$ (M. A. Lieberman & Lichtenberg, 2005).

Plasma etching and cleaning

Cleaning of surfaces means the removal of all possible undesired residues, such as oxides, metallic and organic contaminants. Plasma-assisted cleaning of surfaces offers some alternatives to conventional wet (chemical) cleaning. In the case of cultural heritage, this can be achieved by plasma etching.

Plasma etching is essentially used to remove material from a surface. It can be conducted with a variety of discharge sources, such as d.c. glow discharges and cc rf discharges. The three most important parameters for etching are etch rate uniformity, anisotropy and selectivity. In capacitively coupled systems, the geometry of the electrode assembly at the wafer perimeter is most critical for etch rate uniformity, especially in the wafer edge region.

Anisotropic etching means that the material is removed in the vertical direction only, whereas the horizontal etch rate is zero (see Fig. 17a). Opposed to that is isotropic etching, which is characterised by equal vertical and horizontal etch rates.

Another critical process parameter is selectivity (i.e. removing one type of material while leaving other materials unaffected). It appears that highly-selective plasma etch processes are not easily designed. In fact, selectivity and anisotropy often compete in the design of a plasma

etch process (Michael A. Lieberman, 1999). There are basically four different low pressure plasma etch mechanisms, i.e. (1) sputter-etching, (2) chemical etching, (3) ion-enhanced energetic etching and (4) ion-enhanced inhibitor etching. The degree of anisotropy and selectivity will depend on the etch mechanism used.

1. The mechanism of sputter-etching is identical to sputter-deposition, but the discharge parameters are now optimized for the efficient removal of material from the target instead of the deposition of the sputtered atoms on a substrate. Sputtering is a more or less non-selective process, and the sputter yield depends only on the energy of the bombarding species, the masses of projectile and target species, and the surface binding energy. Consequently, there is not a great difference between sputter yields for different materials. However, sputtering is an anisotropic process which depends greatly on the angle of incidence of the bombarding ions.

2. The second mechanism is pure chemical etching. Atoms or radicals from the discharge plasma can chemically react with the target surface to form projectiles in the gas phase. Chemical etching is essentially isotropic, because the etching atoms arrive at the target surface with a nearly uniform angular distribution. Anisotropic etching is only possible when the reaction takes place between etching atoms and a crystal, where the etching rate depends on the crystallographic orientation. The etch rate is generally not determined by the flux of etching atoms, but rather by the set of reactions at the surface.

3. The third mechanism is ion-enhanced energetic etching. The discharge provides etching particles and energetic ions for the etch process. It appears that the combination of etching atoms and energetic ions is much more effective than the separate mechanisms of sputter-etching and chemical etching. The etching process itself is probably chemical, but with a reaction rate determined by the energetic ion bombardment. This etching method can also be very anisotropic, but the selectivity is generally lower than with chemical etching.

4. The last etching mechanism is ion-enhanced inhibitor etching. The discharge provides not only etching atoms and energetic ions, but also so-called inhibitor precursor molecules. The latter are deposited on the target material, to form a protective layer. The etching atoms are chosen in order to obtain a high chemical etch rate in the absence of ion bombardment and the inhibitor. The bombarding ion flux prevents the formation of an inhibitor layer and it removes this layer so that the target surface can be exposed to the etching atoms. Hence, the target surface will only be etched where there is no inhibitor layer. In this way, the ion-enhanced inhibitor etching is very selective, as well as anisotropic. Possible problems of ion-enhanced inhibitor etching are, however, the contamination of the surface, and the removal of the protective film after the etching step. To reach a compromise between parameters such as efficiency, precision, selectivity and anisotropy, the different etch mechanisms can be coupled to each other (parallel or after each other).

4.1.2 Instrumentation

The apparatus used for this project is a capacitively coupled parallel plate reactor with an asymmetric electrodes configuration, Figure 4.4. It consists of a vacuum chamber made of stainless steel, a powered electrode connected to a RF power supply (13.56 MHz) through an impedance matching unit and a ground electrode. Gas flow rates are controlled by mass-flow controllers, while a turbomolecular pump backed by a rotary pump, a throttle valve, and a pressure gauge allow to keep the pressure fixed at the selected value.

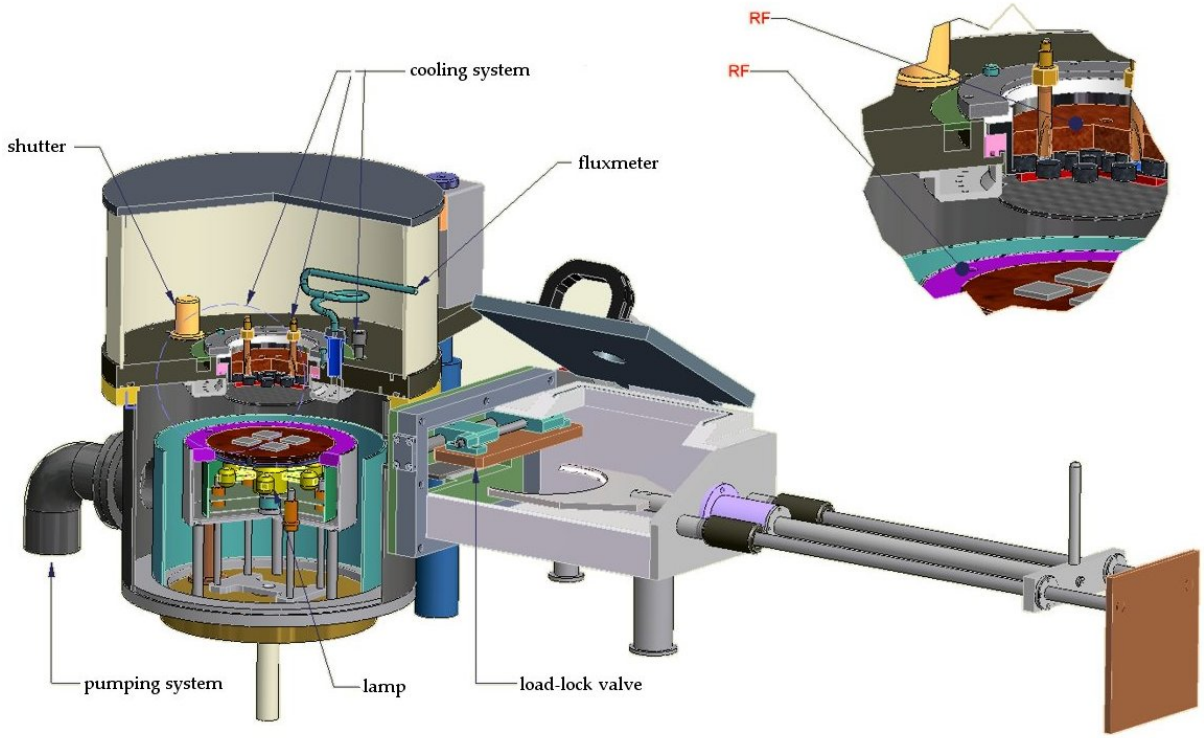

FIGURE 4.4: Schematic representation of the experimental plasma reactor.

4.2 Experimental parameters

Plasma cleaning treatments were carried out on three cuprite, and four malachite samples. The samples were processed on the grounded electrode, by applying the RF power, in the range of 20 W to 30 W, to a gas mixture containing hydrogen (H_2) and argon (Ar) in different ratios. The total flowrate was 100 sccm (standard cubic centimetre per minute) and the pressure inside the process chamber was of 7 Pa to 9 Pa. Table 4.1 summarises the different experimental conditions used for cleaning.

TABLE 4.1: Experimental parameters of plasma cleaning tests.

Sample	Ar/H_2 ratio (sccm)	RF Power (W)	Pressure (Pa)	Time (min)
Cuprite				
P1	4:1	20	7.1	20
P2	3:2	20	9.0	20
P3	3:2	30	8.8	20
Malachite				
P4	4:1	20	7.5	20
P5	3:2	20	9.2	20
P6	3:2	30	8.8	20
P7	3:2	30	9.0	60

4.3 Results

Seven different samples with either a cuprite or malachite patina were treated in a low pressure hydrogen plasma. The reference samples were imaged with high resolution photography and characterised by FESEM and μXRD. The cuprite patina samples (Figure 4.5) have a reddish brown corrosion layer (Figure 4.5a) composed of cuprite, as can be seen in the x-ray diffractogram (Figure 4.5c) of the reference sample. Peaks corresponding to copper from the substrate and x-ray source, can also be identified. The micro-structure of the patina is seen in Figure 4.5b.

The malachite patina samples have a reddish brown layer of cuprite with a layer of malachite and nantokite crystals on top (Figure 4.6a). The composition of the patina was confirmed by μXRD analysis (Figure 4.6c), which also shows the peaks corresponding to copper. Figure 4.6b is a FESEM micrograph showing the micro-structure of the patina crystals.

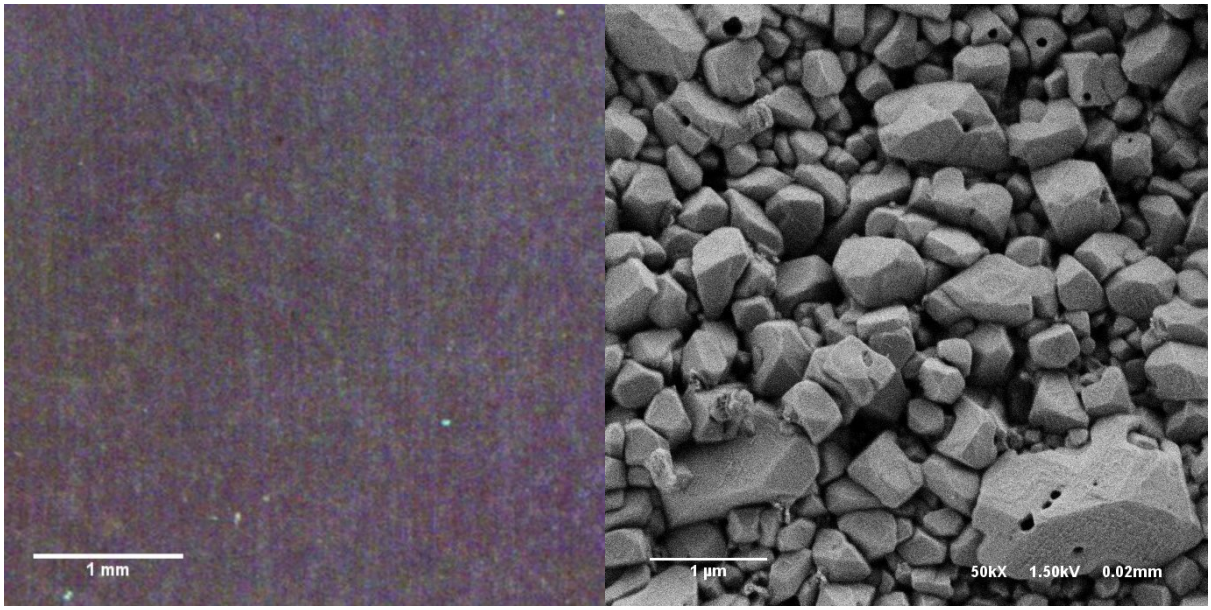

(a) (b)

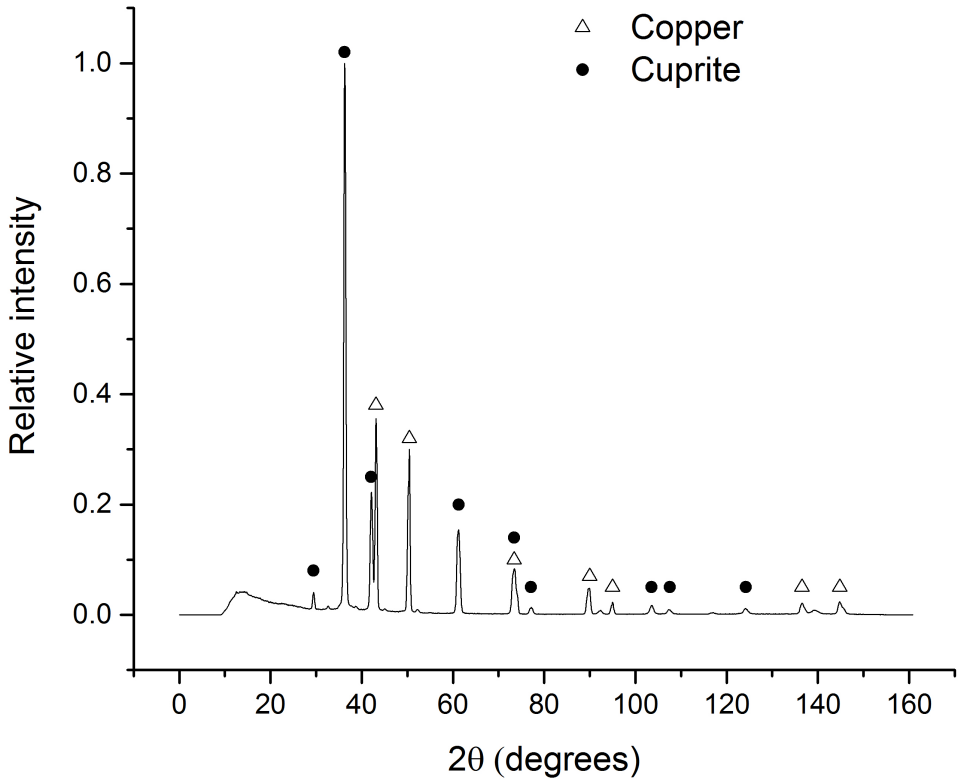

(c)

FIGURE 4.5: Image (a), FESEM micrograph (b), and x-ray diffractogram with labelled peaks for cuprite and copper (c), of a reference cuprite patina sample used for plasma cleaning tests.

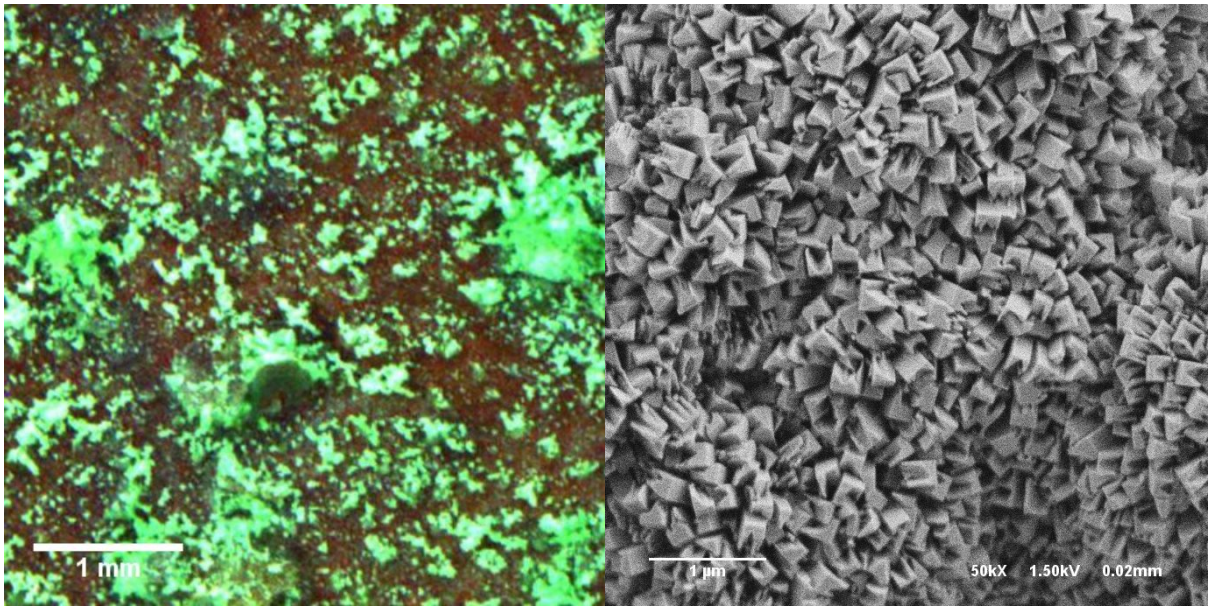

(a) (b)

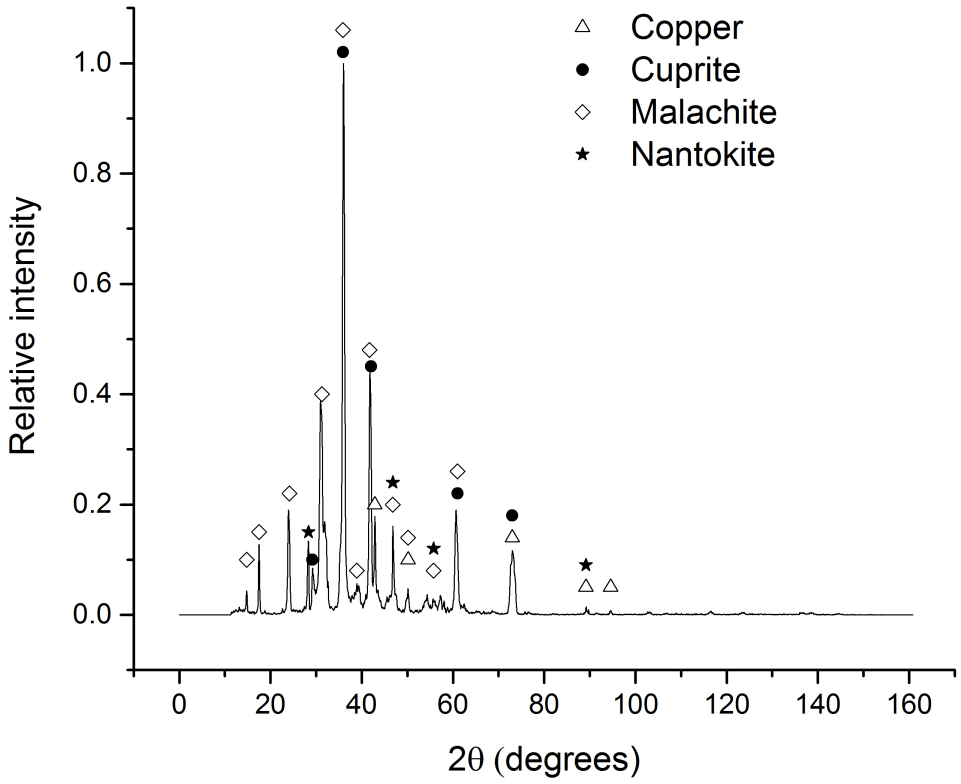

(c)

FIGURE 4.6: Image (a), FESEM micrograph (b), and x-ray diffractogram with labelled peaks for cuprite, malachite, nantokite, and copper (c) of a reference malachite patina sample used for plasma cleaning tests.

4.3.1 Cuprite samples

On cuprite samples, the applied power was enough to remove some of the patina. As can be seen on the images in Figure 4.7, visibly the patina is removed, but the FESEM images show that some of the cuprite patina remains on the surface.

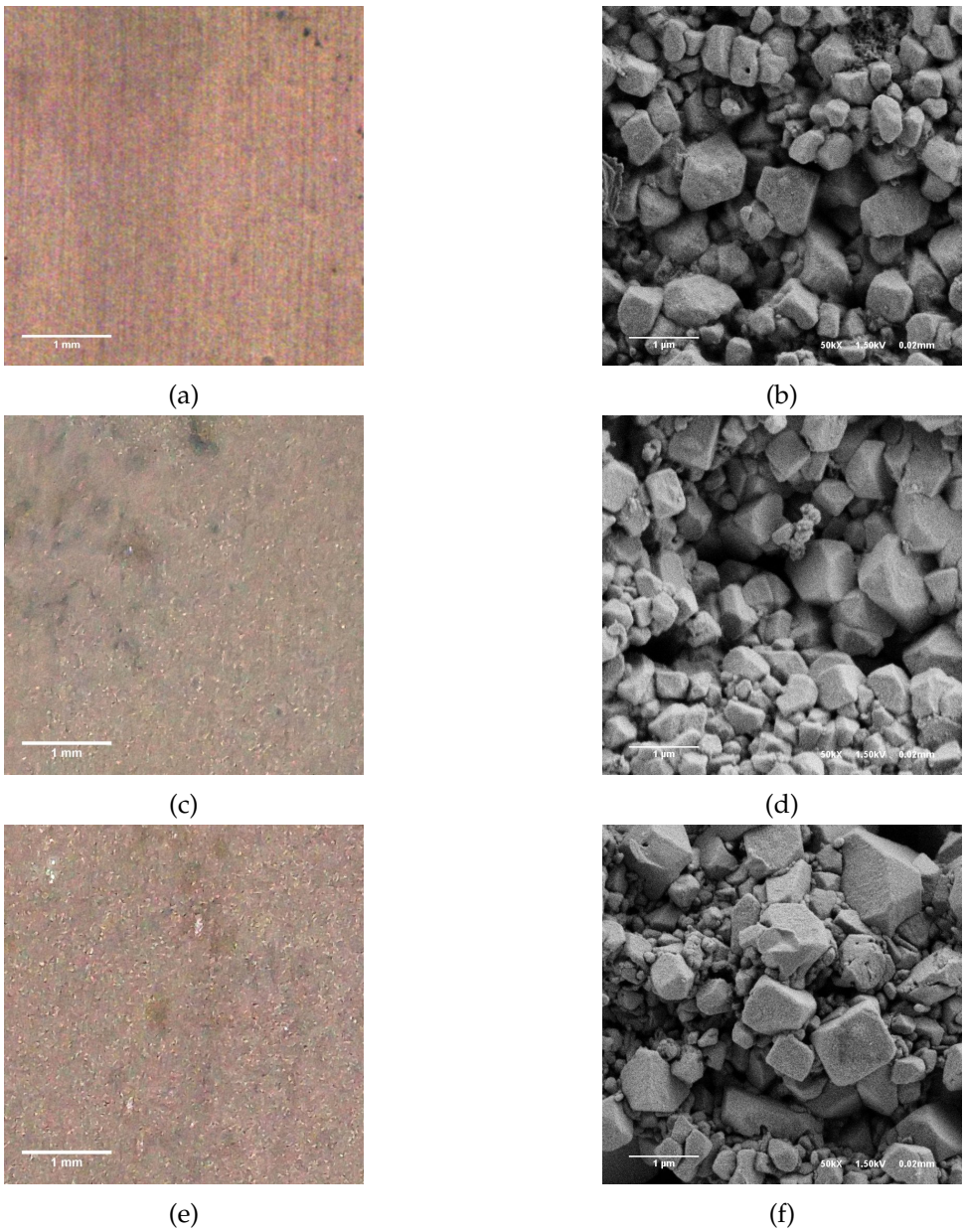

FIGURE 4.7: Images and FESEM micrographs of cuprite patina plasma cleaning samples. P1 (a) and (b); P2 (c) and (d); and P3 (e) and (f).

μXRD analyses were performed on all the samples after treatment and the results show that the cuprite layer thickness has been reduced when compared to the original, as evidenced

by the increase in relative intensity of the peaks corresponding to copper. Figure 4.8 shows the x-ray diffractogram of sample P3, which shows the largest difference in composition when compared to the original patina. This is not surprising, since a higher power was applied to this sample [1].

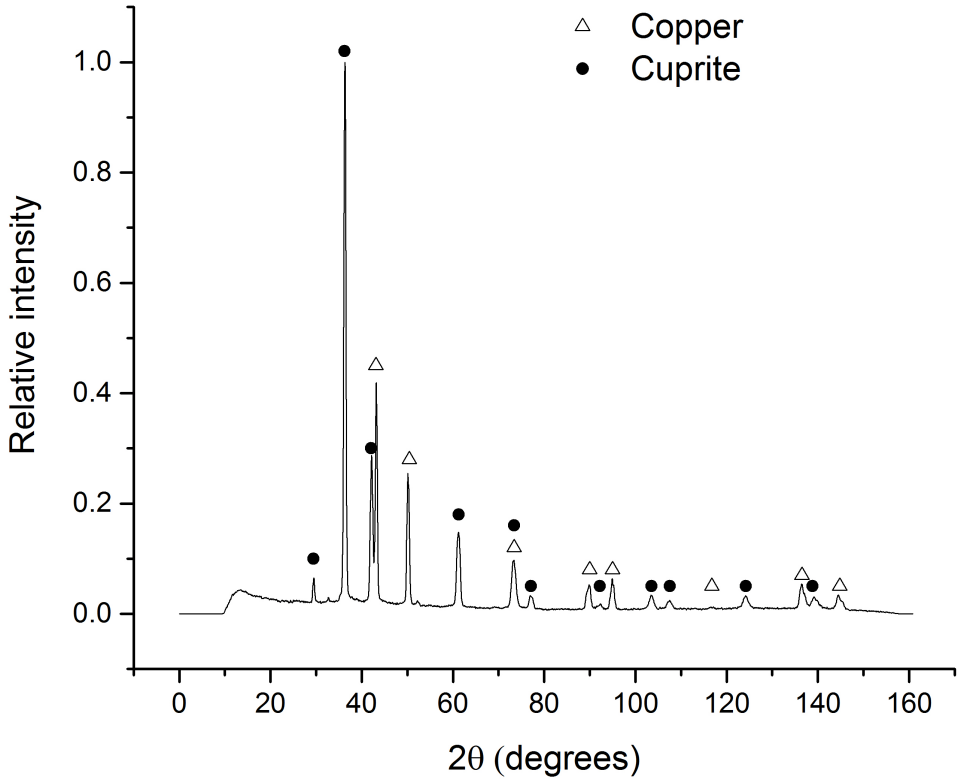

FIGURE 4.8: X-ray diffractogram of the patina on sample P3 with labelled peaks for cuprite and copper.

4.3.2 Malachite samples

The visible results on malachite patina samples are shown in Figure 4.9 with high resolution and FESEM images of samples P4 to P7. In these samples the changes in colour are easily seen, going from green crystals to a brown to dark brown patina, with some crystals in the midst. Also, some pieces of the patina were lifted from the surface. FESEM micrographs show crystal micro-structures similar to the original patina, which means that although the aspect of the samples changed, the malachite/nantokite crystals are still present.

[1] X-ray diffractograms for the rest of the samples can be found in Appendix B.

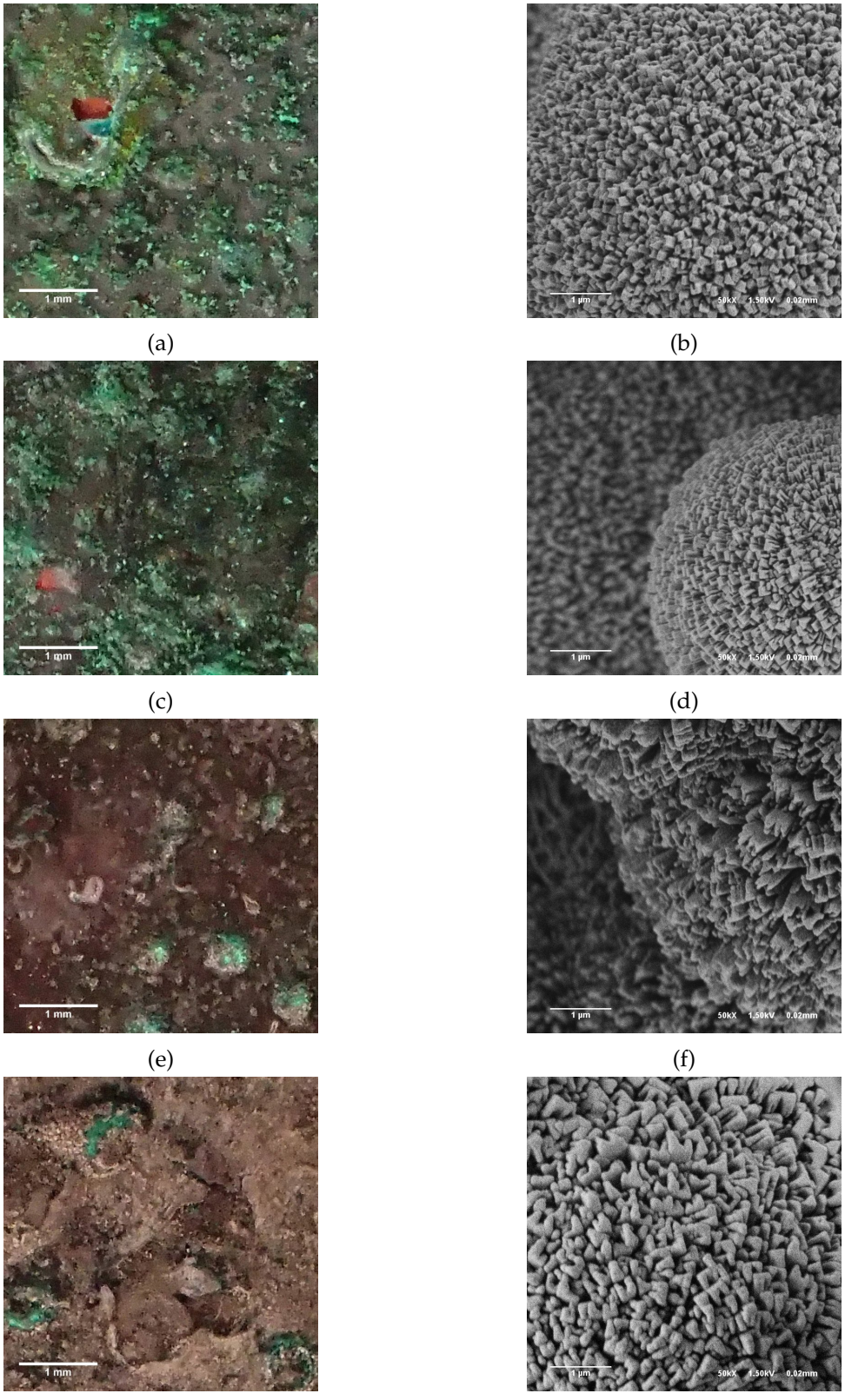

FIGURE 4.9: Images and FESEM micrographs of malachite patina plasma cleaning samples. P4 (a) and (b); P5 (c) and (d); P6 (e) and (f); and P7 (g) and (h).

After treatment, μXRD analyses were performed on all samples (see Appendix B). Figure 4.10 shows the diffractogram obtained for sample P7, where the copper and copper oxide peaks have a higher intensity with respect to the original patina, while the malachite peaks' relative intensity has not changed, and nantokite peaks have a low intensity or have disappeared, signaling the removal of the chlorides. This means that the malachite/nantokite layer has been partially removed. The sharpness and intensity of the peaks, however, indicate that the patina retains a crystalline structure.

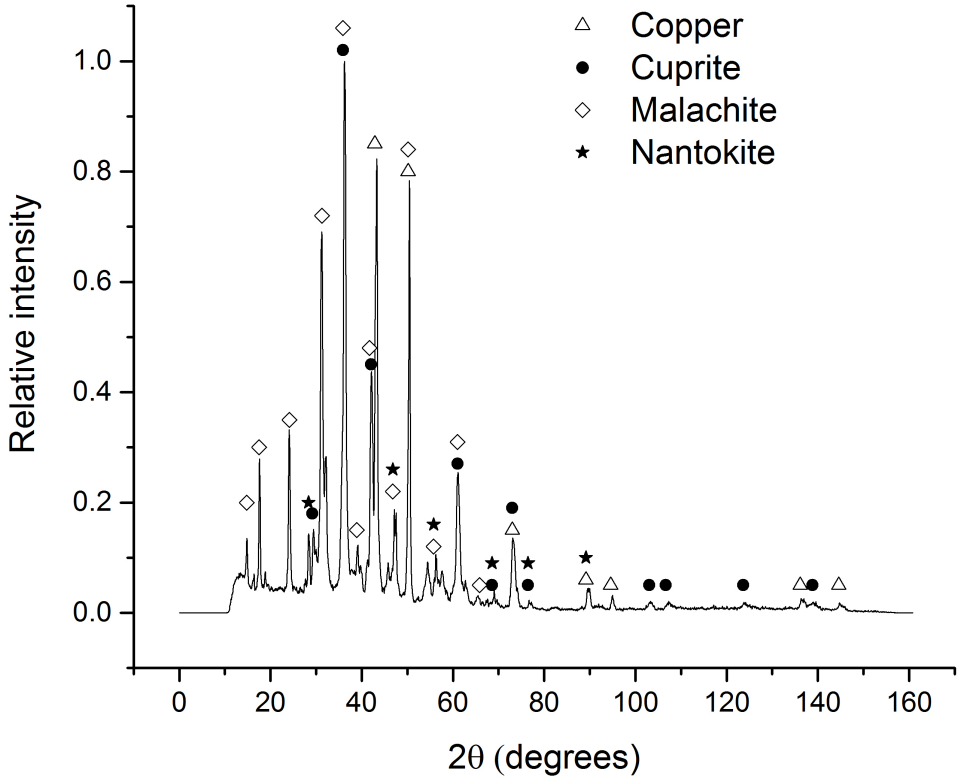

FIGURE 4.10: X-ray diffractogram of the patina on sample P7 with labelled peaks for cuprite, malachite, nantokite, and copper.

A glow discharge in a low pressure hydrogen plasma produces H atoms as well as ions. Though not studied in detail yet, it can be supposed that hydrogen atoms directly react with the patina and remove copper chlorides by the formation of volatile hydrogen chloride (HCl). The impinging ions also have an effect, enhancing the reactivity of the stroke surface, and it is also possible that the copper compounds are reduced to copper, and copper oxide. It is also observed that, in dependence of the treatment time, the H_2 plasma is able to significantly reduce the thickness of the corrosion layer.

4.4 Conclusions and future experiments

Plasma cleaning treatments on cuprite samples were performed, the layer was partially removed, with a thin layer of cuprite remaining on the samples. Cleaning of malachite patina samples resulted in a reduced corrosion layer, the total removal of the undesired corrosion layer can probably be achieved by increasing the treatment time or applied power. Modifying the parameters is easily done and, since the process is non-invasive and does not modify the bulk material, i.e. the copper substrate, harmless.

Increasing the applied power, increases the etching of the patina, resulting in a more efficient cleaning process. This is not feasible with the used instrument since it causes sputtering from the copper electrodes, and hence contamination of the sample, but can be avoided if the cathode electrode is made of stainless steel. Furthermore, increasing the treatment time allows the reactions taking place in the chamber and the action of the impinging ions to carry out, giving a more efficient cleaning. Additionally, increasing the H_2 pressure in the chamber can facilitate the chemical reactions needed for removal of the patina.

Chapter 5

Electrochemical Characterisation

5.1 Electrochemical Impedance Spectroscopy (EIS)

EIS is a powerful tool in developing the most appropriate methodology for ensuring long-lasting artefact preservation. EIS consists in the measurement of amplitude and phase of the surface impedance of coated metallic objects at different frequencies in order to highlight either the protective effectiveness of a coating or the stability of a corrosion product layer grown onto the metallic surface. The advantage of EIS over other laboratory techniques for the assessment of the corrosion behaviour of coated systems, is the possibility of using very small amplitude signals without significantly disturbing the properties being measured (Grassini et al., 2007; Hernández, Aoki, Tribollet, & de Melo, 2011). A severe limitation of EIS is the need of performing the measurement in an electrolyte that can affect the conservation state of an artefact of archaeological and historical value (Angelini, Grassini, & Parvis, 2010).

Electrochemical impedance theory is a branch of ac theory that describes the response of a circuit to an alternating current or voltage as a function of frequency. In dc theory (a special case of ac theory where the frequency equals 0 Hz) resistance is defined by Ohm's Law (Equation (5.1)).

$$E = IR \tag{5.1}$$

Using Ohm's law, you can apply a dc potential (E, V) to a circuit, measure the resulting current (I, A), and compute the resistance (R, Ω). A resistor is the only element that impedes the flow of electrons in a dc circuit.

In ac theory, where the frequency is non-zero, resistance is replaced by impedance (Z, Ω), the ac equivalent of resistance (Equation (5.2)). In addition to resistors, capacitors and inductors impede the flow of electrons in ac circuits.

$$E = IZ \tag{5.2}$$

In an electrochemical cell, slow electrode kinetics, slow preceding chemical reactions, and

diffusion can all impede electron flow, and can be considered analogous to the resistors, capacitors, and inductors that impede the flow of electrons in an ac circuit. It follows, then, that an equivalent electrical circuit, representative of the processes taking place in the system, can be determined for an electrochemical cell. Figure 5.1 shows the equivalent circuit for a metal/coating/electrolyte system, with two constant phase elements (CPE) which substitute the coating capacitance, C_c (CPE 1), and the double layer capacitance, C_{dl} (CPE 2), and which takes into account the phenomena related to the heterogeneous surface and diffusion processes.

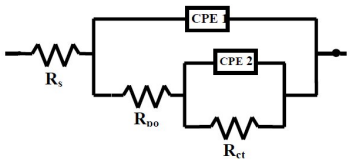

FIGURE 5.1: Equivalent circuit model of the system metal/coating/electrolyte (Angelini et al., 2004).

The impedance of a CPE is represented by Equation (5.3), where C is a constant depending on the analysed system, $i = \sqrt{-1}$, ω is the angular frequency, α a coefficient ranging between 0 to 1 and is related to the roughness of the surface. On smooth electrodes $\alpha = 1$ and $C = C_c or C_{dl}$. The pore resistance due to electrolyte penetration and at the damaged areas of the film is represented by R_{po}, while the charge transfer resistance, R_{ct}, may be related to the degree of coating (Angelini et al., 2004; Barsoukov & Macdonald, 2005).

$$Z = C\frac{1}{(i\omega)^{\alpha}} \tag{5.3}$$

EIS data is usually represented using Nyquist and Bode plots. Nyquist plots depict the imaginary impedance (Z'', Ω), indicative of the capacitive and inductive character of the cell, versus the real impedance of the cell (Z', Ω). Nyquist plots have the advantage that activation controlled processes with distinct time constants show up as unique impedance arcs and the shape of the curve provides insight into possible mechanism or governing phenomena (Angelini et al., 2010). Bode plots depict the absolute impedance ($|Z|$, Ω) or the phase angle (θ, °) versus frequency (ω, Hz), usually in a logarithmic scale. $|Z|$ and θ can be calculated from experimental values of Z' and Z'', by Equations (5.4) and (5.5), respectively.

$$|Z| = \sqrt{Z'^2 + Z''^2} \tag{5.4}$$

$$\tan\theta = \frac{Z''}{Z'} \tag{5.5}$$

5.2 Methods and instrumentation

Impedance spectra were recorded at the open circuit potential (OCP) by applying a sinusoidal signal of 10mV amplitude in the frequency range 100 000 Hz to 0.010 Hz with five points per decade. EIS experiments were controlled with an Ivium CompactStat: Portable Electrochemical Interface & Impedance Analyser potentiostat (see Section 2.1).

5.3 Results and discussion

elctrochemical impedance spectroscopy measurements were performed on copper electrodes with different patinas in order to obtain information on the protective properties of the corrosion product layer formed in different solutions. The measurements were performed under continuous immersion over two months. Figures 5.2 and 5.3 show representative impedance spectra of copper with a cuprite and malachite patina, respectively, recorded after various immersion times in 0.1 mol/l Na_2SO_4 solution or corrosive water (see Section 2.1.3).

From the spectra in Figure 5.2a it is possible to observe the presence of two time constants, related to the metal/solution and patina/solution electrochemical interfaces, respectively. The impedance increases as soon as the patina grows on the surface, after two weeks, and coats almost the entire surface although the thickness of the oxide layer is not too high; after four weeks the impedance and protective effectiveness decreases, probably due to diffusion reactions, which are due to the existence of ionic paths protruding through the oxide film.

In the case of malachite sample (Figure 5.3), the patina grows in the first four weeks and then the impedance decreases a little bit after eight weeks, probably due to a few diffusion reactions and a slow dissolution of copper. Since the patina has two layers (oxide and crystals) the impedance is higher than in the cuprite sample, even when the malachite/nantokite layer is not homogeneous. It appears from these results that the dissolution of copper is heavily influenced by diffusion phenomena and the corrosion product film porosity.

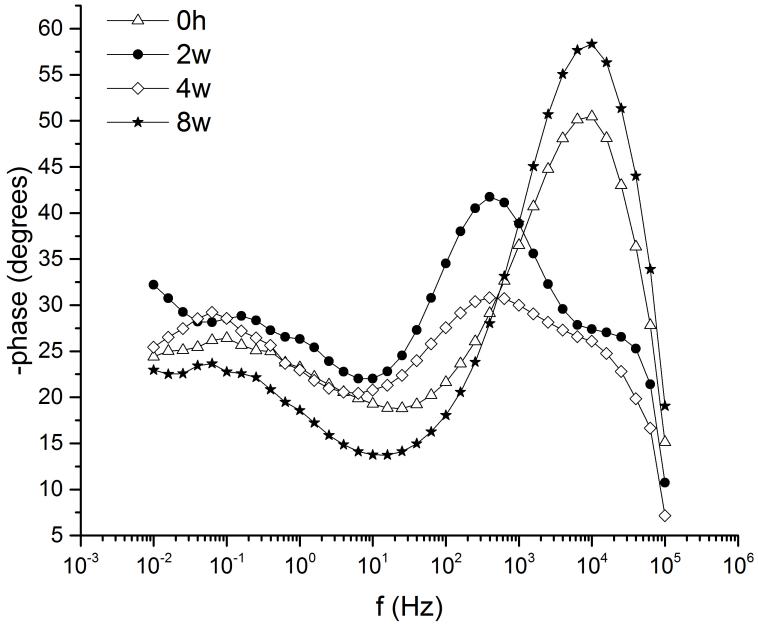

(a)

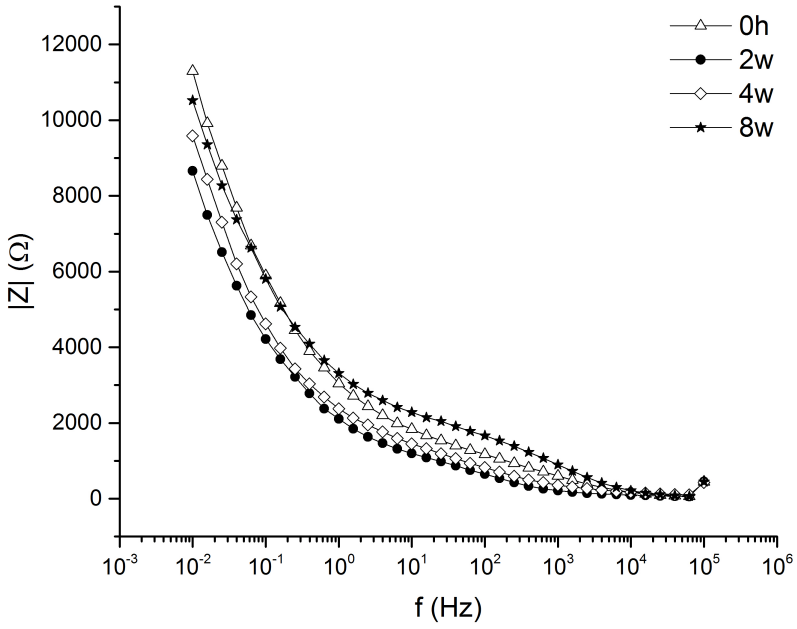

(b)

FIGURE 5.2: Bode plots, absolute impedance (a) and phase angle (b), of the EIS spectra of copper samples coated with a cuprite patina submitted to continuous immersion in 0.1 mol/l Na_2SO_4 over 8 weeks

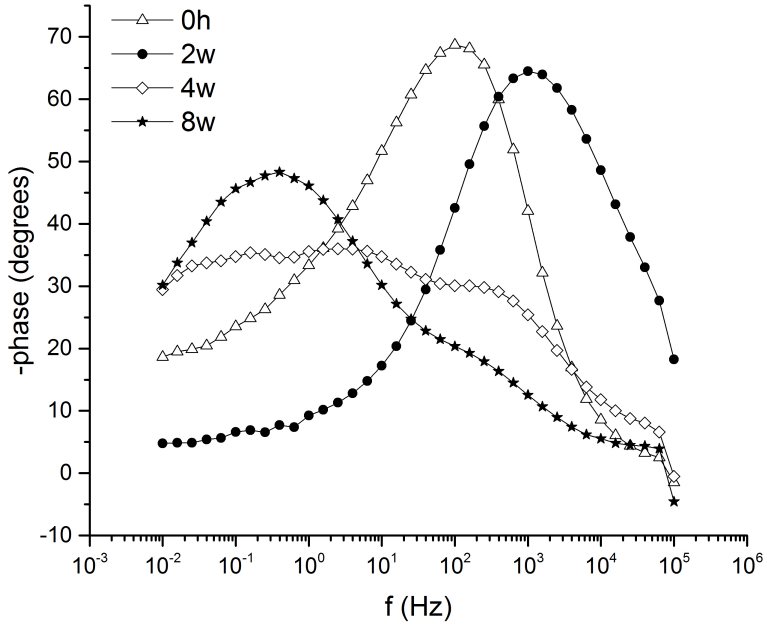

(a)

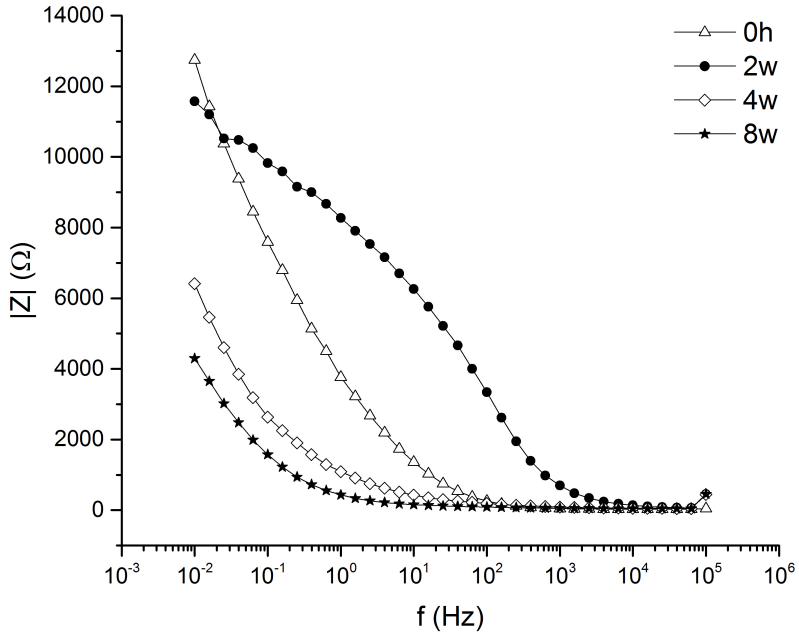

(b)

FIGURE 5.3: Bode plots, absolute impedance (a) and phase angle (b), of the EIS spectra of copper samples coated with a malachite patina submitted to continuous immersion in corrosive water over 8 weeks

Chapter 6

Summary and Conclusions

The conservation and valorisation of cultural heritage is of fundamental importance for our society, since it is witness to the artistic and industrial legacies of human societies. The information that can be gathered from such materials is a valuable source to understanding the past. A large component of this consists of material cultural assets that are often exposed to harmful long-term effects of environmental pollution, inappropriate handling, and intrinsic chemical–physical instability. In the case of metallic artefacts, one of the main problems is the preservation of archaeological objects taken out of excavation and stored in museums or deposits. Because corrosion is a never-ending problem, archaeologists and curators often face the challenge to choose the correct strategies for cleaning and preservation. During burial, copper-based artefacts react with the environment and become covered with corrosion products of different compositions, mainly oxides, sulphides, basic sulphates, chlorides, hydroxichlorides, basic green carbonates, and oxalates. Among them, corrosion products containing chlorides are considered very dangerous because copper and copper alloys can suffer from the effects of chloride salts, resulting in the development of bronze disease. However, the patina of copper alloys, such as bronzes, is often considered valuable, and for this reason it is important to remove the chlorides in the most complete way, while preserving the protective cuprite layer or any other desired corrosion products. For these reasons, the focus of this project was the development of protocols for cleaning archaeological copper artefacts by laser and plasma cleaning.

Laser cleaning relies on PLA for the removal of unwanted materials, such as pollutants, dirt, and corrosion products, in a precise, accurate, and highly controlled manner. Other advantages of the method include site selectivity, lack of mechanical or chemical contact with the substrate, and diversity in the types of substrates that can be treated. On the other hand, low pressure plasmas exhibit some major advantages for their application in the field of conservation of Cultural Heritage, especially metals. They are dry processes, easily performed at room temperature, so they guarantee the preservation of metallurgical features; they can be applied directly on the exterior or the interior of complex shapes. Plasma etching, the process involved in cleaning, can be controllable and selective at the nanoscale and can be very mild.

Due to the uniqueness and inhomogeneous nature of archaeological artefacts, their use as

samples for the evaluation of the processes assessed in this study is not advisable, instead reference copper samples were used to evaluate the cleaning parameters. Additionally, electrochemical characterisation of the artificial patinas was performed in order to obtain information on the protective properties of the corrosion product layers. These were measured using elctrochemical impedance spectroscopy, which consists in the measurement of amplitude and phase of the surface impedance of coated metallic objects at different frequencies in order to highlight either the protective effectiveness of a coating or the stability of a corrosion product layer grown onto the metallic surface.

A set of laser cleaning tests were performed on reference samples coated with three different kinds of patinas. In all instances, partial removal of the corrosion layer was achieved, but the interaction between the laser and materials were too aggressive, and resulted in melting of the cuprite layer, which should be preserved during conservation processes. Further experiments should be designed, with fluence values lower than $1.5\,J/cm^2$, while considering other parameters, such as the pulse overlap, in order to avoid melting of the desired corrosion layers. Additionally, cross-section analysis of the patinas would be helpful in determining if the substrate is being affected by the laser treatments. Nevertheless, it is clear that different protocols should be developed for different patinas, and real artefacts should be characterised previous to any treatment to determine the best course of action in regards to cleaning of their surface. The use of a UV laser has been proposed for further studies since the undesired compounds in the corrosion layers have a high absorbance at ultraviolet wavelengths. Moreover, the chemical interaction between the laser and material should also be investigated.

Plasma cleaning treatments were performed on samples with two kinds of patinas. In both cases the corrosion layers were partially removed. A glow discharge in a low pressure hydrogen plasma produces hydrogen atoms as well as ions. Though not studied in detail yet, it can be supposed that hydrogen atoms directly react with the patina and remove copper chlorides by the formation of volatile hydrogen chloride. The impinging ions also have an effect, enhancing the reactivity of the stroke surface, and it is also possible that the copper compounds are reduced to copper, and copper oxide. It is also observed that, in dependence of the treatment time, the hydrogen plasma is able to significantly reduce the thickness of the corrosion layer.

The total removal of the undesired corrosion products can probably be achieved by increasing the treatment time or applied power. Modifying the parameters is easily done and since the process is non-invasive and does not modify the bulk material, harmless. Increasing the applied power, increases the etching of the patina, resulting in a more efficient cleaning process. Furthermore, increasing the treatment time allows the reactions taking place in the chamber and the action of the impinging ions to carry out, giving a more efficient cleaning. Additionally, increasing the hydrogen pressure in the chamber can facilitate the chemical reactions needed for removal of the patina.

Elctrochemical impedance spectroscopy measurements were performed on copper electrodes with cuprite and malachite patinas. The measurements were performed under continuous immersion over two months. In the case of the cuprite patina, the impedance increases over two weeks, i.e. while the patina grows on the surface. After a month, the impedance and protective effectiveness decreases, probably due to diffusion reactions, which are due to the existence of ionic paths protruding through the oxide film. The malachite sample shows different results, the patina grows in the first four weeks and then the impedance decreases a little bit after eight weeks, probably due to a few diffusion reactions and a slow dissolution of copper. Since the patina has two layers (oxide and crystals) the impedance is higher than in the cuprite sample, even when the malachite and nantokite layer is not homogeneous. It appears from these results that the dissolution of copper is heavily influenced by diffusion phenomena and the corrosion product film porosity.

Both techniques show good results for cleaning, as long as the proper parameters are used. These depend on the nature of the artefact and the corrosion layers that are found on its surface.

References

Adriaens, A. & Dowsett, M. (2004). Electron microscopy and its role in cultural heritage studies. In *Comprehensive Analytical Chemistry* (Vol. 42, pp. 73–128). Elsevier.

Angelini, E., Batmaz, A., de Caro, T., Faraldi, F., Grassini, S., Ingo, G. M., & Riccucci, C. (2014, October). The role of surface analysis in the strategies for conservation of metallic artefacts from the Mediterranean Basin: Conservation metallic artefacts. *Surface and Interface Analysis*, *46*, 754–763. doi:http://dx.doi.org/10.1002/sia.5512

Angelini, E., Fracassi, F., Grassini, S., Rosalbino, F., & d'Agostino, R. (2004). PECVD Organosilicon thin films for corrosion protection of metals. In *Trends in electrochemistry and corrosion at the beginning of the 21st century: dedicated to professor Dr. Josep M. Costa on the occasion of his 70th birthday* (pp. 979–999). Barcelona: Publicacions Universitat de Barcelona.

Angelini, E., Grassini, S., Fracassi, F., d'Agostino, R., Palumbo, F., & Ciringiloglu, A. (2007). Cultural heritage protection with low pressure plasma treatments. *Vacuum International*, *2*, 26–32.

Angelini, E., Grassini, S., & Parvis, M. (2010, October). Silver artefacts: plasma deposition of SiOx protective layers and tarnishing evolution assessment. *Corrosion Engineering, Science and Technology*, *45*(5), 334–340. doi:http://dx.doi.org/10.1179/147842210X12767807773484

Barsoukov, E. & Macdonald, J. R. (Eds.). (2005). *Impedance spectroscopy: theory, experiment, and applications*. Hoboken, N.J: Wiley-Interscience.

Bäuerle, D. (2011). *Laser processing and chemistry* (4. ed). Berlin: Springer.

Bogaerts, A. (2007). Plasma diagnostics and numerical simulations: insight into the heart of analytical glow discharges. *J. Anal. At. Spectrom.* *22*(1), 13–40. doi:http://dx.doi.org/10.1039/B611436A

Bogaerts, A., Neyts, E., Gijbels, R., & van der Mullen, J. (2002, April). Gas discharge plasmas and their applications. *Spectrochimica Acta Part B: Atomic Spectroscopy*, *57*(4), 609–658. doi:http://dx.doi.org/10.1016/S0584-8547(01)00406-2

Bron, F., Carignan, L.-P., Mnard, D., & Yelo, A. (2010, February 1). Extracting Individual Properties from Global Behaviour: First-order Reversal Curve Method Applied to Magnetic Nanowire Arrays. In N. Lupu (Ed.), *Electrodeposited Nanowires and their Applications*. In-Tech.

Chapman, B. N. (1980). *Glow discharge processes: sputtering and plasma etching*. New York: Wiley.

Chung, F. H. & Smith, D. K. (Eds.). (2000). *Industrial applications of X-ray diffraction*. New York: Marcel Dekker.

Crow, D. R. (1994). *Principles and applications of electrochemistry* (4th ed). Cheltenham, U.K: S. Thornes.

De Ryck, I., Adriaens, A., Pantos, E., & Adams, F. (2003). A comparison of microbeam techniques for the analysis of corroded ancient bronze objects. *The Analyst*, *128*(8), 1104. doi:http://dx.doi.org/10.1039/b303588c

Degrigny, C. (2007). Examination and conservation of historical and archaeological metal artefacts: a European overview. In *Corrosion of Metallic Heritage Artefacts* (pp. 1–17). Elsevier.

Fotakis, C. (Ed.). (2007). *Lasers in the preservation of cultural heritage: principles and applications*. New York, NY: Taylor & Francis, v. 2. Series in optics and optoelectronics.

Gettens, R. J. (1961, January 1). Mineral alteration products on ancient metal objects. *Studies in Conservation*, *6*, 89–92. doi:http://dx.doi.org/10.1179/sic.1961.s022

Grassini, S., Angelini, E., d'Agostino, R., Palumbo, F., & Ingo, G. (2007). Advanced Plasma Treatment for Cleaning and Protecting Precious Metal Artefacts. In V. Argyropoulos (Ed.), *Strategies for saving our cultural heritage: papers presented at the international conference on conservation strategies for saving indoor metallic collections with a satellite meeting on legal issues in the conservation of cultural heritage, Cairo 25 February - 1 March 2007* (pp. 127–132). Athens: TEI of Athens.

Hamann, C. H., Hamnett, A., & Vielstich, W. (2007). *Electrochemistry* (2., completely rev. and updated ed). Weinheim: Wiley-VCH.

Hernández, R. d. P., Aoki, I., Tribollet, B., & de Melo, H. (2011, February). Electrochemical impedance spectroscopy investigation of the electrochemical behaviour of copper coated with artificial patina layers and submitted to wet and dry cycles. *Electrochimica Acta*, *56*(7), 2801–2814. doi:http://dx.doi.org/10.1016/j.electacta.2010.12.059

Hrnjic, M., Angurel, L. A., Lahoz, R., Grassini, S., Angelini, E., Schiavon, N., & de la Fuente, G. F. (2015, October 21–23). Near-IR laser cleaning of Cu-based artefacts: a comprehensive study of the methodology standardization. In *Proceedings of the 1st International Conference on Metrology for Archaeology* (Vol. 1, pp. 389–394). 1st international conference on metrology for archaeology. Benevento, Italy.

Kaesche, H. (2003). *Corrosion of Metals* (). Engineering Materials and Processes. Berlin, Heidelberg: Springer Berlin Heidelberg.

Koh, Y. S. (2005). *Laser cleaning as a conservation technique for corroded metal artifacts* (Doctoral, Lulea University of Technology, Lulea, Sweden).

Ladd, M. & Palmer, R. (2013). *Structure determination by X-ray crystallography: analysis by X-rays and neutrons ; celebrating the Centenary of X-Ray Crystallography* (5. ed). New York: Springer.

Lahoz, R. (2006). *Ablación láser de materiales inorgánicos y metálicos* (Doctoral dissertation, Insituto de Ciencia de Materiales de Aragón (CSIC-Universidad de Zaragoza), Zaragoza, Spain).

Lahoz, R., Angurel, L. A., Brauch, U., Estepa, L. C., & de la Fuente Leis, G. F. (2013). Laser Applications in the Preservation of Cultural Heritage: An Overview of Fundamentals and Applications of Lasers in the Preservation of Cultural Heritage. In *Conservation Science for the Cultural Heritage. Applications of Instrumental Analysis* (79, pp. 296–332). Lecture notes in chemistry. Springer.

Leyssens, K. (2006). *Monitoring the conservation treatment of corroded cupreous artefacts: The use of electrochemistry and synchrotron radiation based spectroelectrochemistry* (Doctoral Dissertation, Ghent University, Ghent, Belgium).

Lieberman, M. A. [M. A.] & Lichtenberg, A. J. (2005). *Principles of plasma discharges and materials processing* (2nd ed). Hoboken, N.J: Wiley-Interscience.

Lieberman, M. A. [Michael A.]. (1999). Plasma Discharges for Materials Processing and Display Applications. In H. Schlüter & A. Shivarova (Eds.), *Advanced Technologies Based on Wave and Beam Generated Plasmas* (pp. 1–22). Dordrecht: Springer Netherlands.

Paddock, S. W. (2000). Principles and Practices of Laser Scanning Confocal Microscopy. *Molecular Biotechnology*, *16*(2), 127–150. doi:http://dx.doi.org/10.1385/MB:16:2:127

Plenderleith, H. J. & Werner, A. E. A. (1971). *The conservation of antiquities and works of art: treatment, repair and restoration* (2d ed). London, New York: Oxford University Press.

Pourbaix, M. & Burbank, J. (1963). Atlas D-Equilibres Electrochimiques. *Journal of The Electrochemical Society*, *111*(1), 14C. doi:http://dx.doi.org/10.1149/1.2426051

Rubahn, H.-G. (1999). *Laser applications in surface science and technology*. Chichester: Wiley.

Scott, D. A. (1990, January). Bronze Disease: A Review of Some Chemical Problems and the Role of Relative Humidity. *Journal of the American Institute for Conservation*, *29*(2), 193–206. doi:http://dx.doi.org/10.1179/019713690806046064

Scott, D. A. (2002). *Copper and bronze in art: corrosion, colorants, conservation* (). Los Angeles: Getty Conservation Institute.

Selwyn, L. (2004). *Metals and corrosion: a handbook for the conservation professional*. Ottawa, Ont: Canadian Conservation Institute.

Siano, S. (2008). Principles of Laser Cleaning in Conservation. In *Handbook of the use of lasers in conservation and conservation science*. Brussels: COST office.

Tylecote, R. F. & Institute of Materials (Great Britain). (1992). *A history of metallurgy*. London: Maney Pub., for the Institute of Materials.

Weeks, E. R. & Semwogerere, D. (2013, February 12). Confocal Microscopy. In *Encyclopedia of Biomaterials and Biomedical Engineering* (Vol. null, *null*, pp. 1–10). Taylor & Francis.

Appendix A

Laser Cleaning

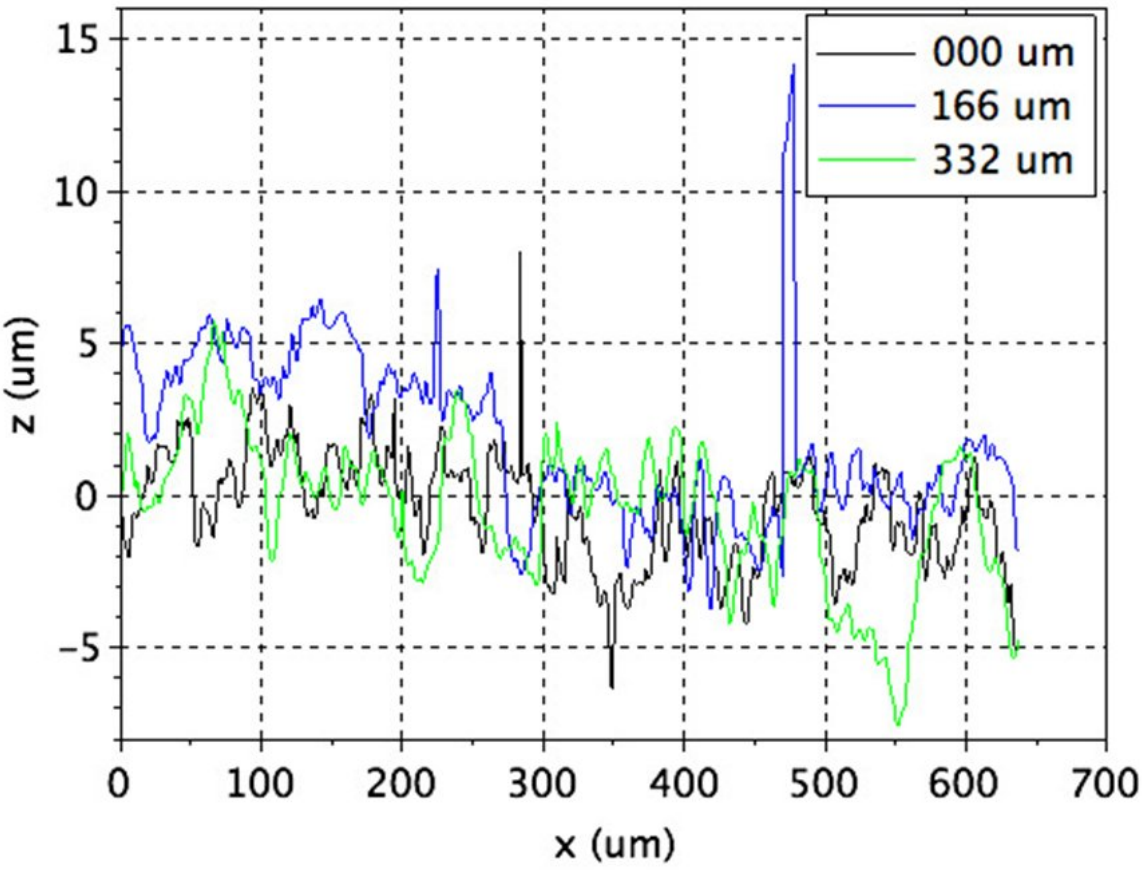

FIGURE A.1: Surface plot of test area A2 of the cuprite sample obtained by confocal microscopy.

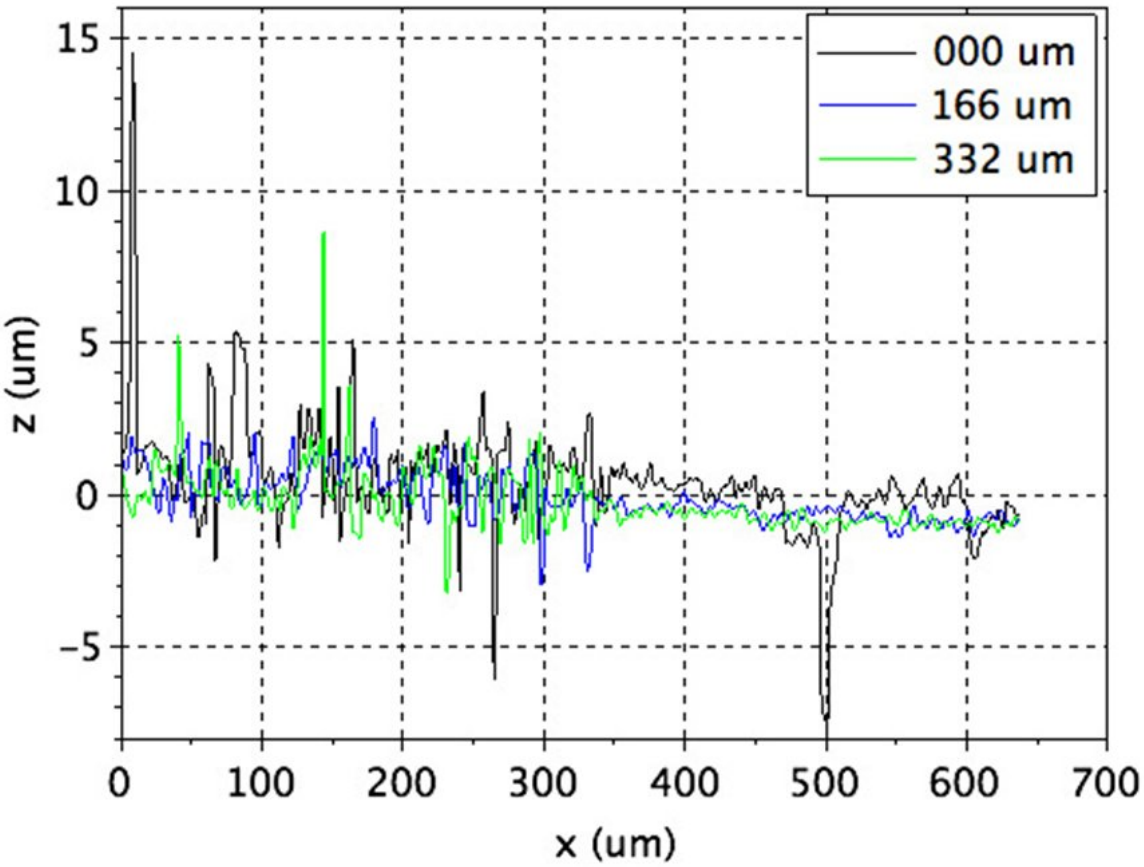

FIGURE A.2: Surface profile of test area A2 of the cuprite sample obtained by confocal microscopy.

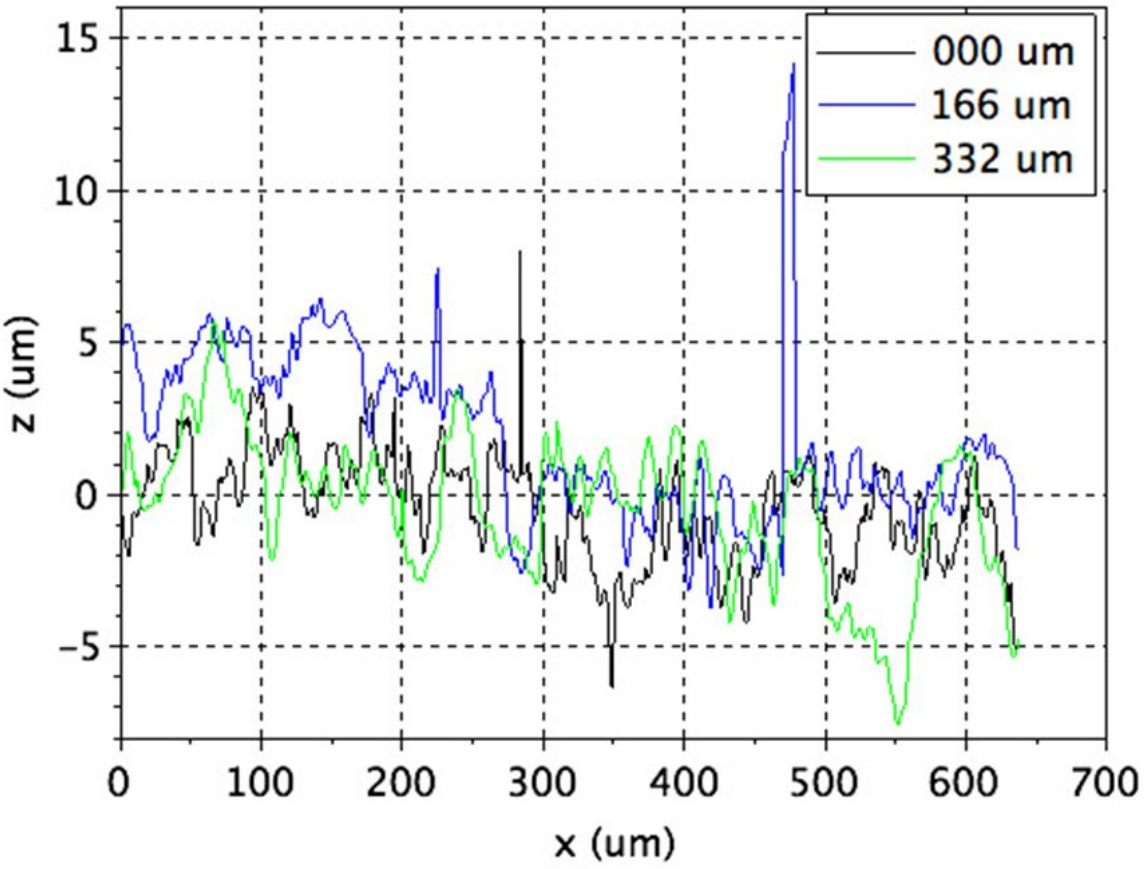

FIGURE A.3: Surface profile of test area C1 of the cuprite sample obtained by confocal microscopy.

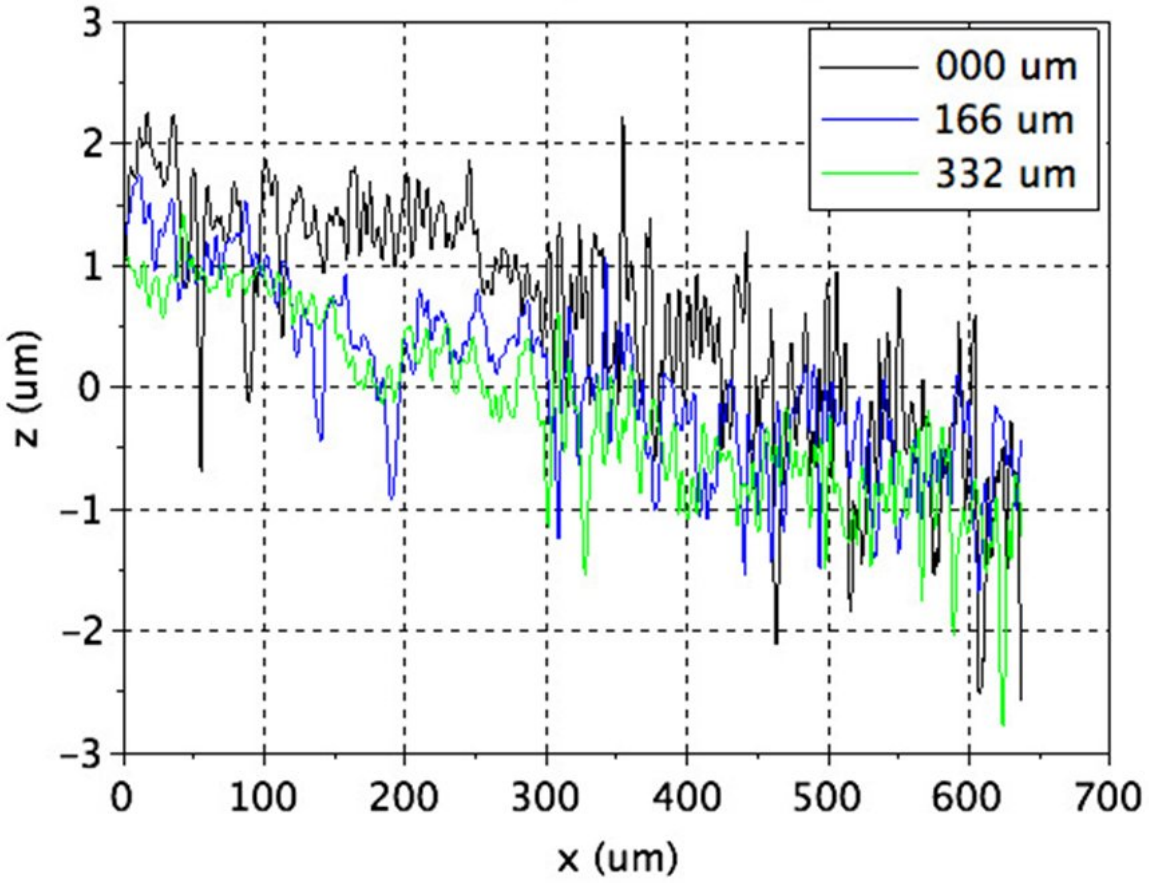

FIGURE A.4: Surface profile of test area B2 of the cuprite sample obtained by confocal microscopy.

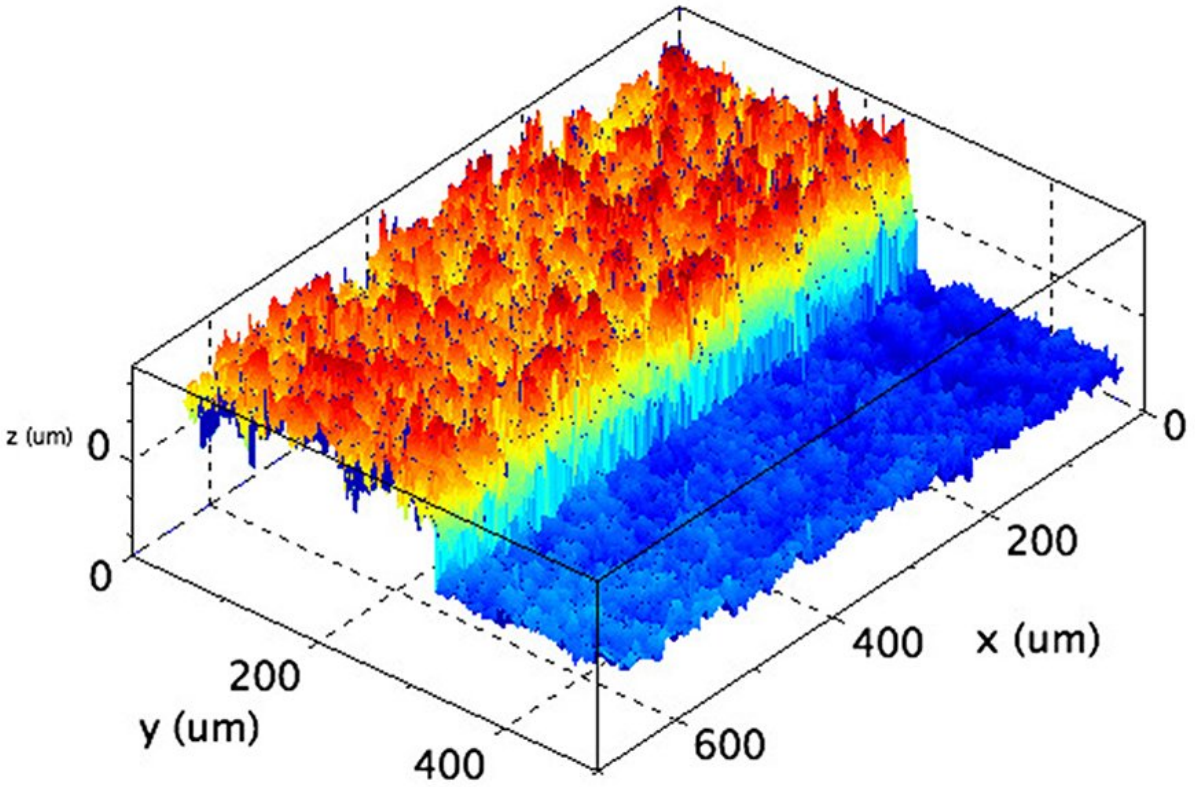

FIGURE A.5: Surface plot of test area A2 of the paratacamite sample obtained by confocal microscopy.

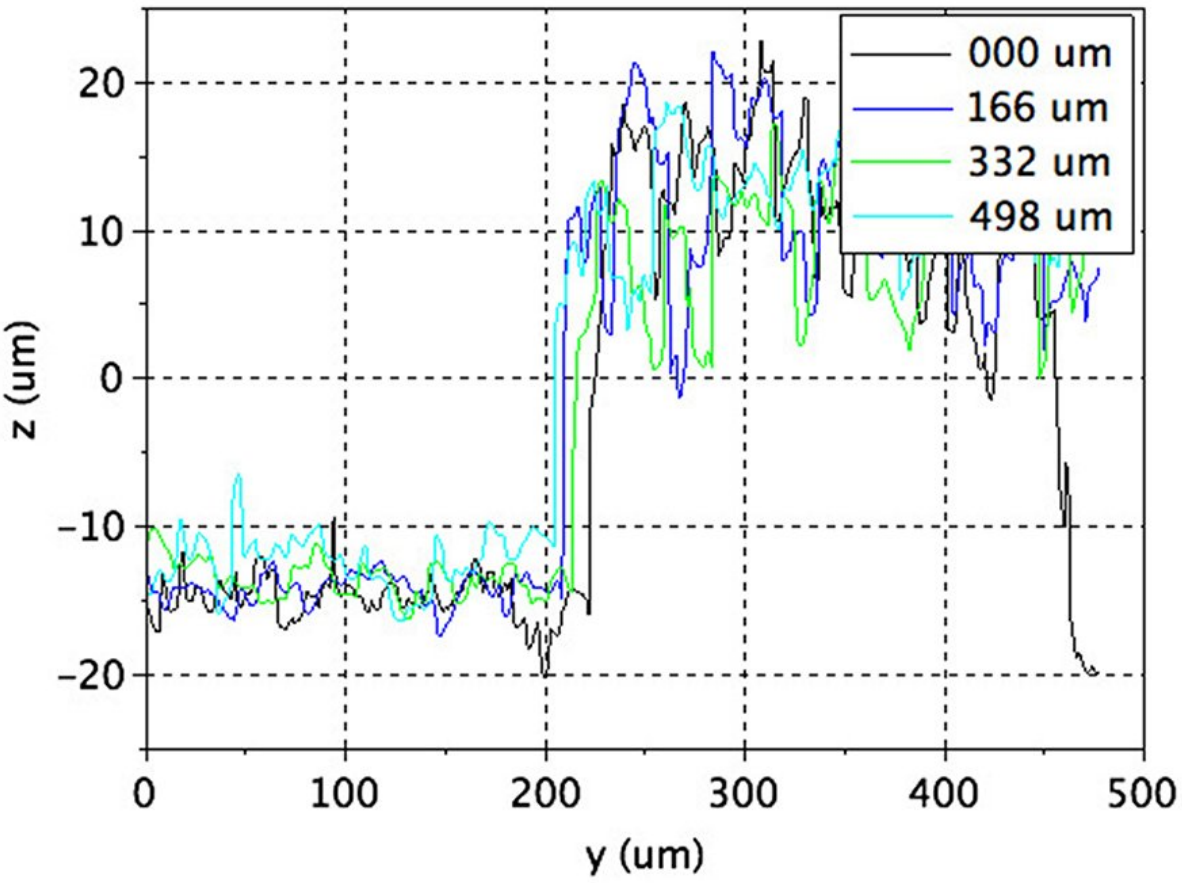

FIGURE A.6: Surface profile of test area A2 of the paratacamite sample obtained by confocal microscopy.

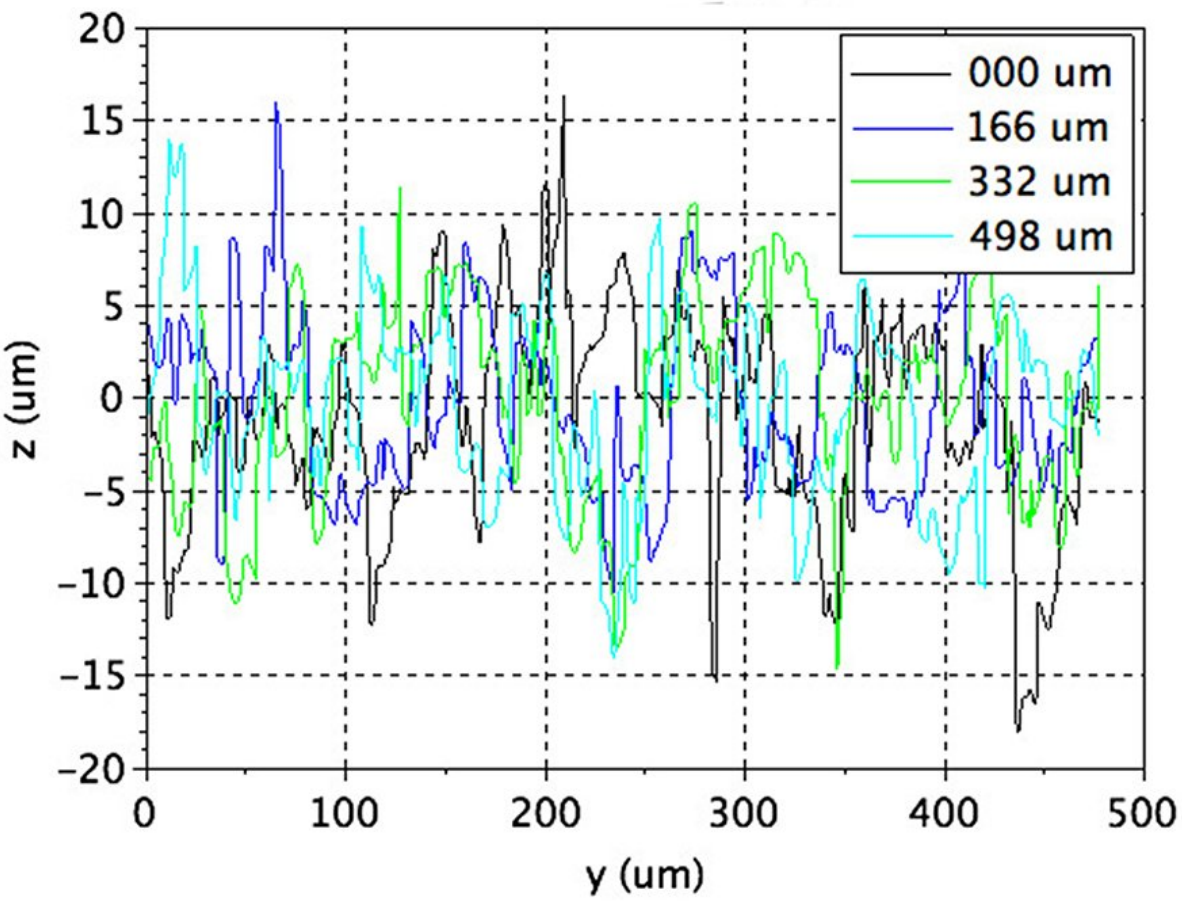

FIGURE A.7: Surface profile of test area C1 of the paratacamite sample obtained by confocal microscopy.

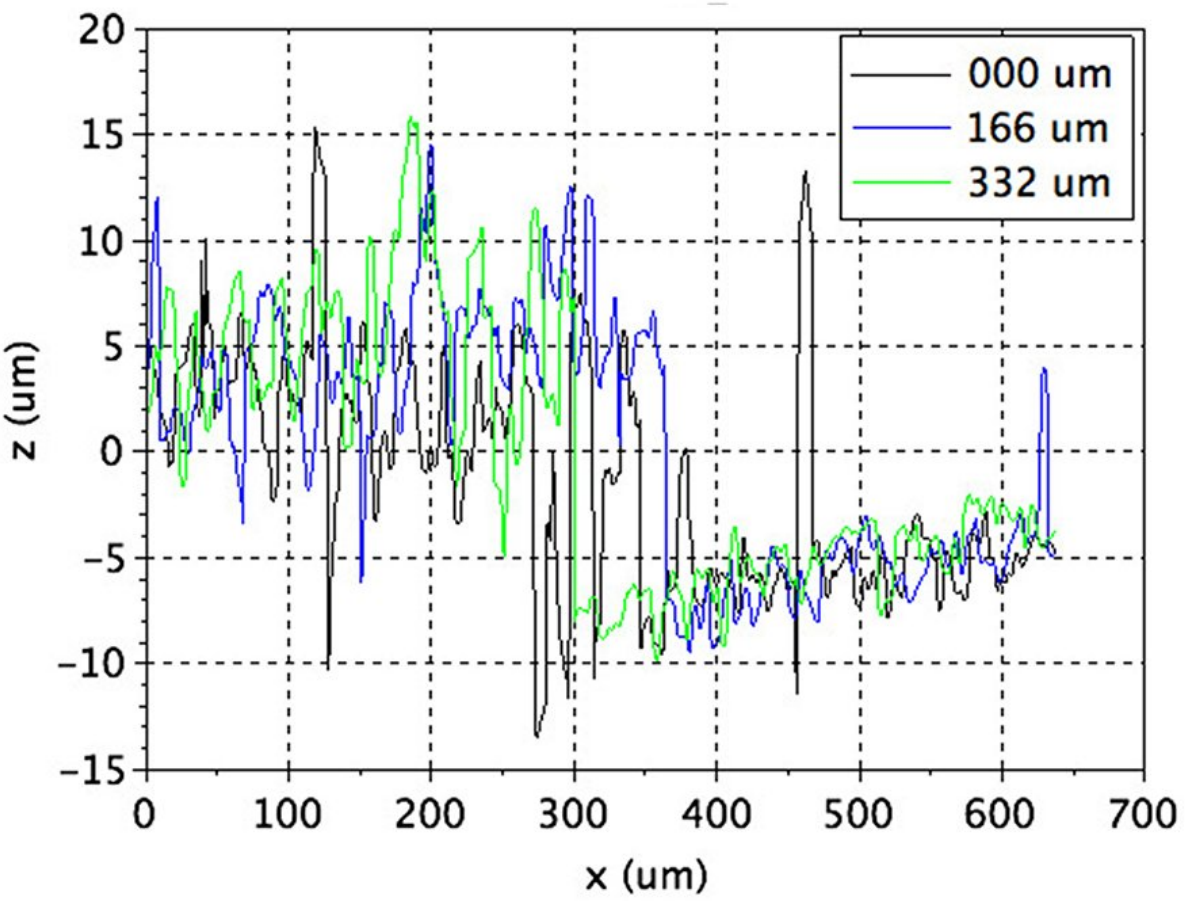

FIGURE A.8: Surface profile of test area B2 of the paratacamite sample obtained by confocal microscopy.

Appendix B

Plasma Cleaning

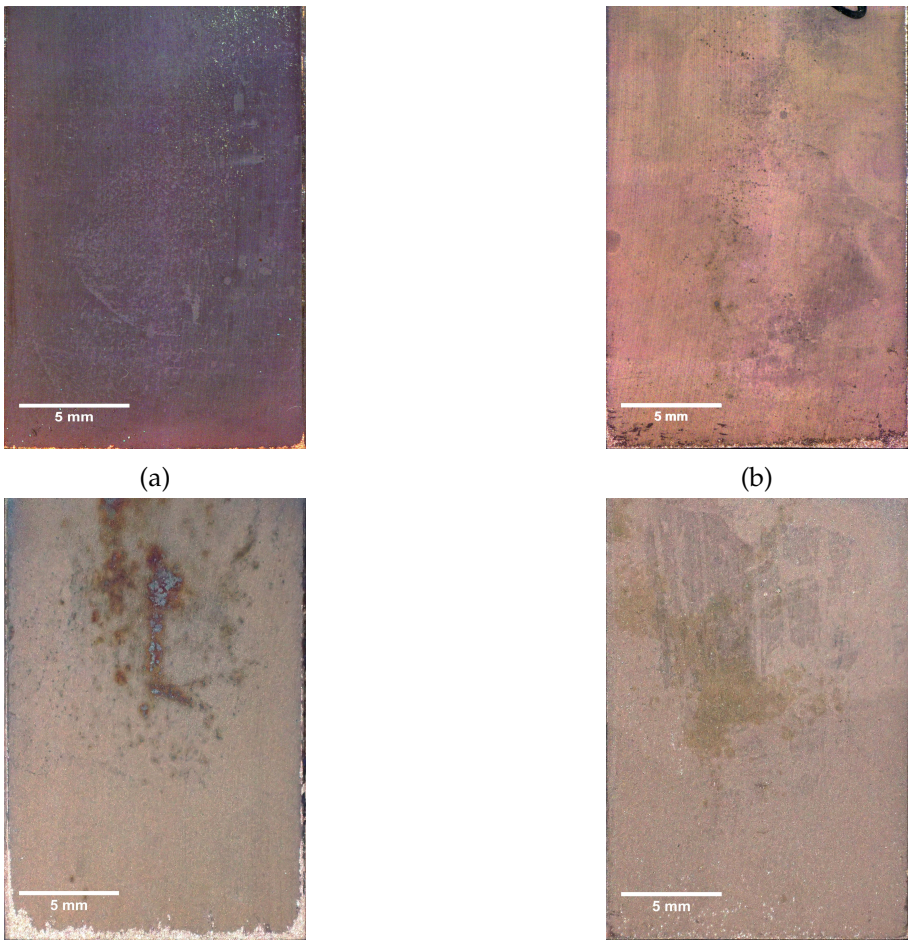

(a) (b)

(c) (d)

FIGURE B.1: Images of cuprite plasma cleaning samples. Reference sample (a), P1 (b), P2 (c), P3 (d).

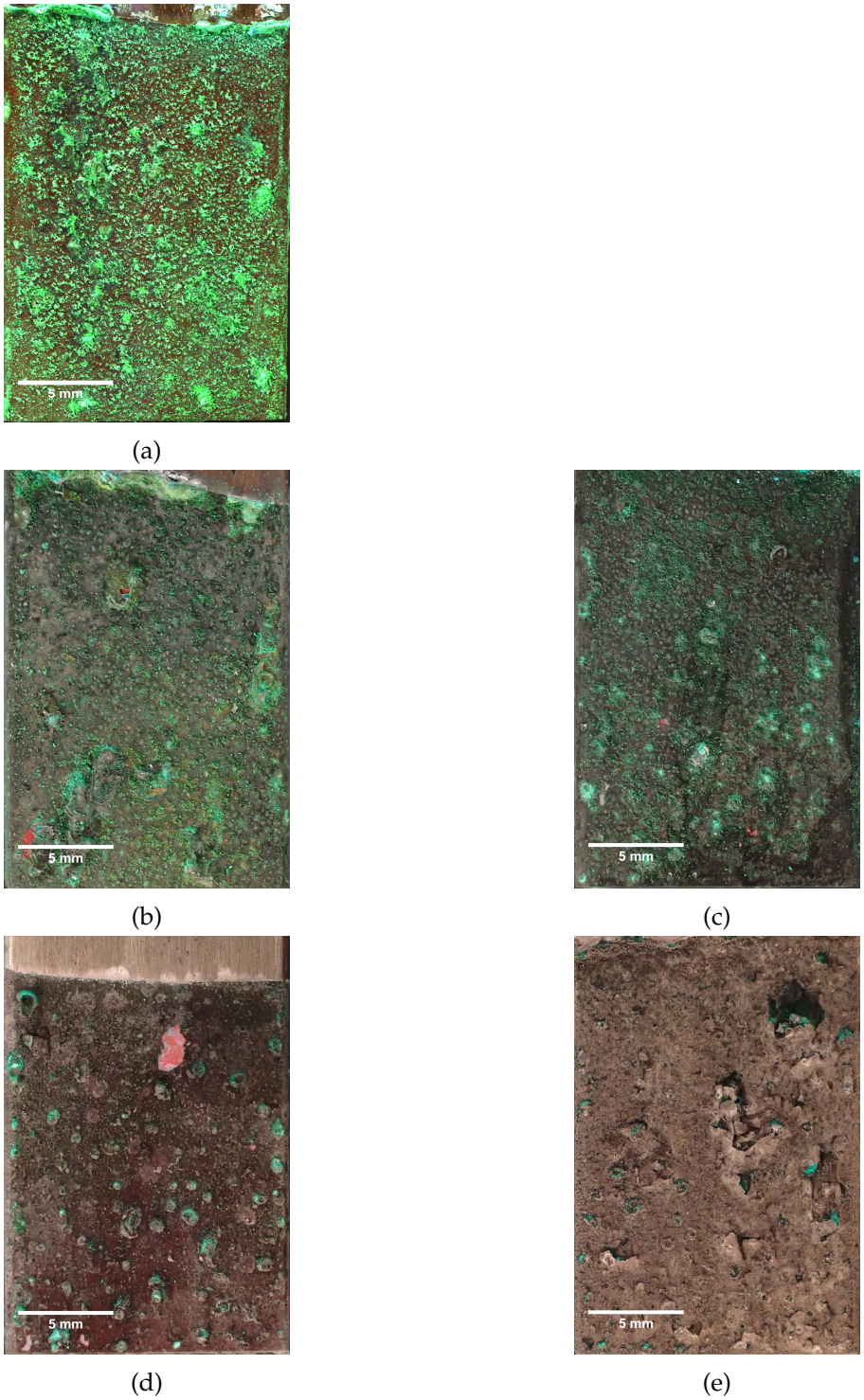

FIGURE B.2: Images of malachite plasma cleaning samples. Reference sample (a), P4 (b), P5 (c), P6 (d), and P7 (e).

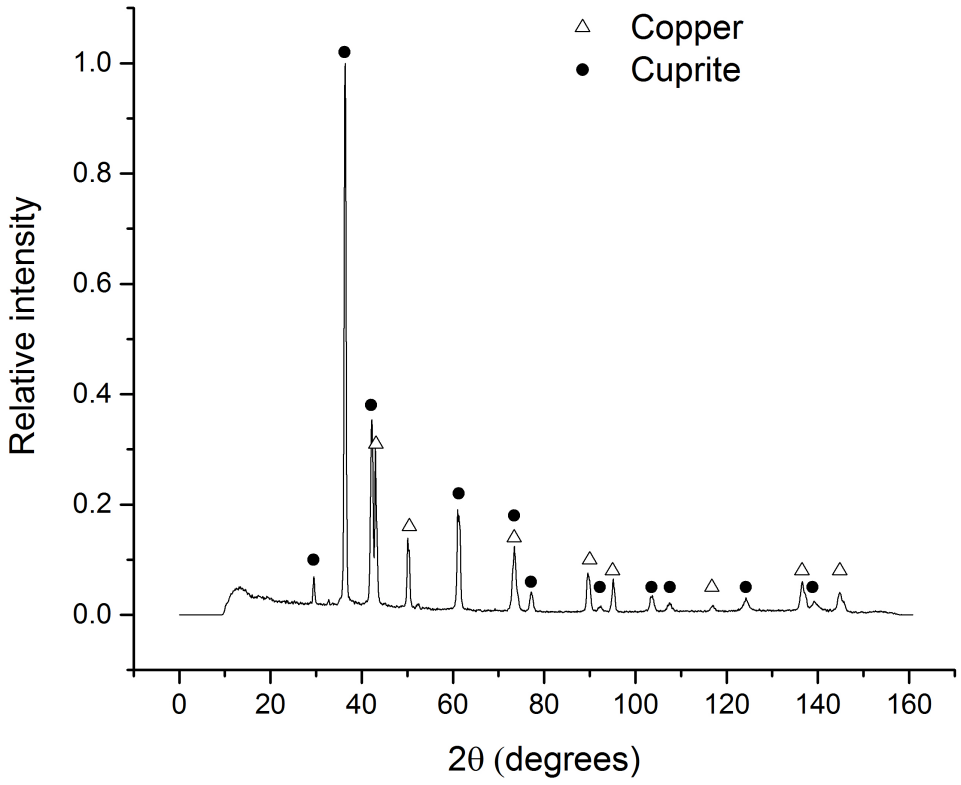

FIGURE B.3: Image of sample P1 after treatment.

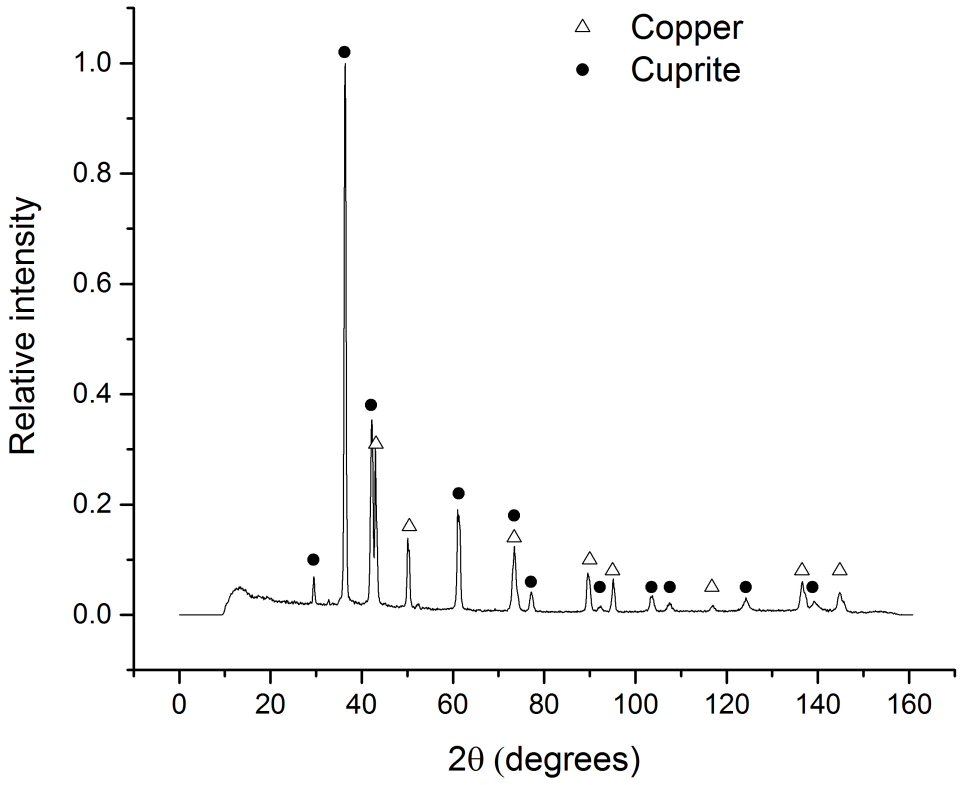

FIGURE B.4: Image of sample P1 after treatment.

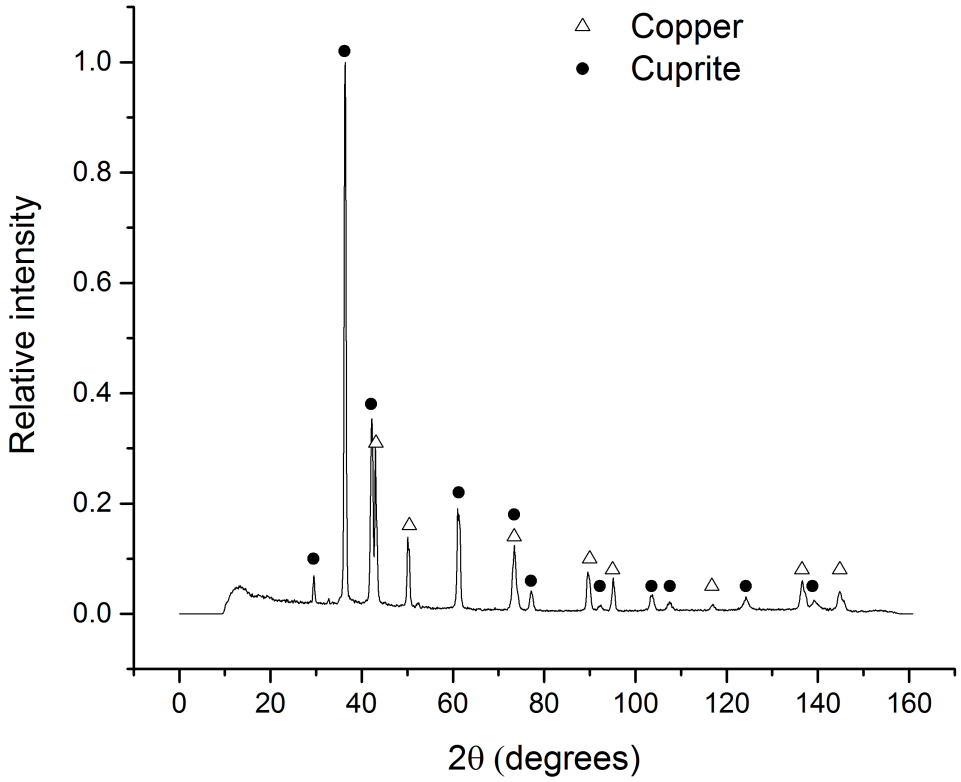

FIGURE B.5: X-ray diffractogram of the patina on sample P1 with labelled peaks for cuprite and copper.

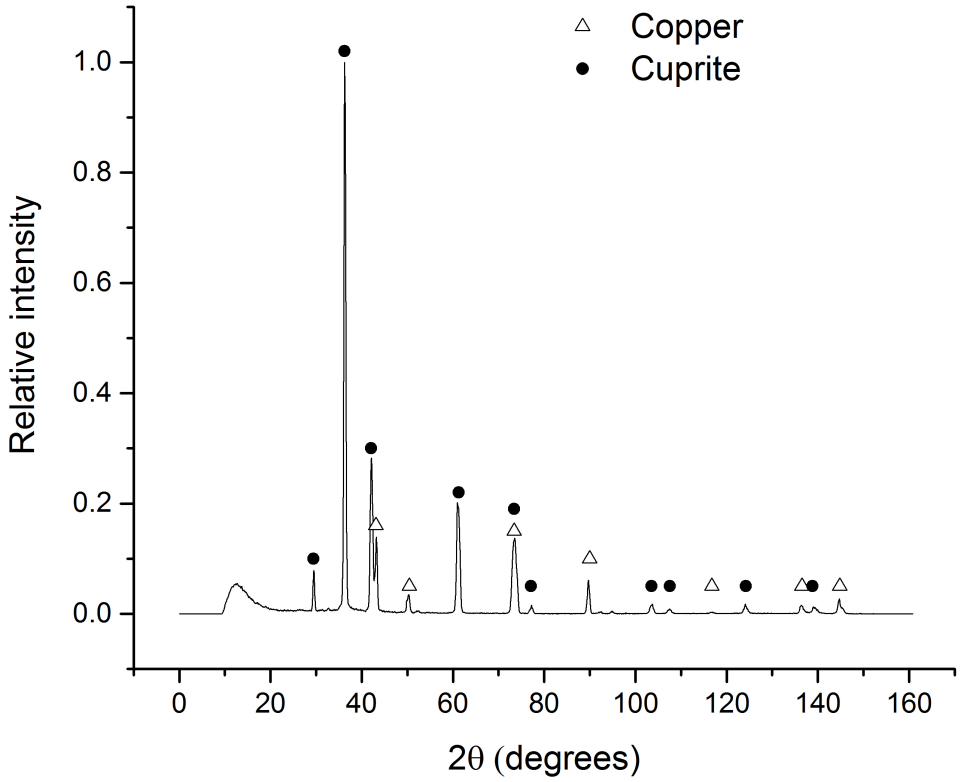

FIGURE B.6: X-ray diffractogram of the patina on sample P2 with labelled peaks for cuprite and copper.

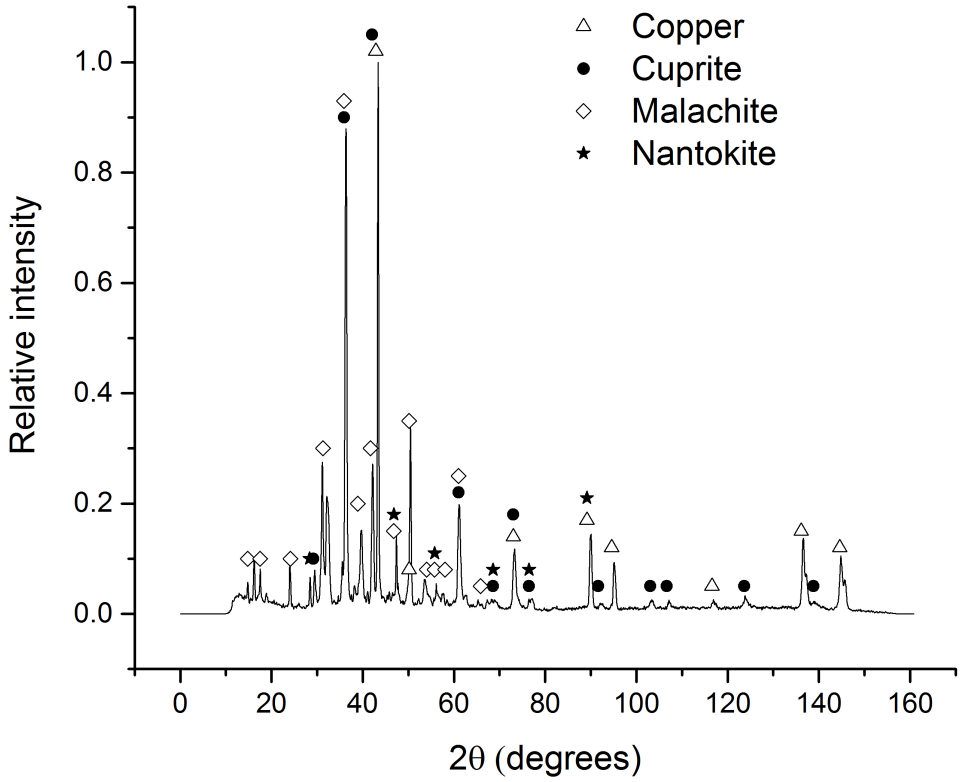

FIGURE B.7: X-ray diffractogram of the patina on sample P4 with labelled peaks for cuprite, malachite, nantokite, and copper.

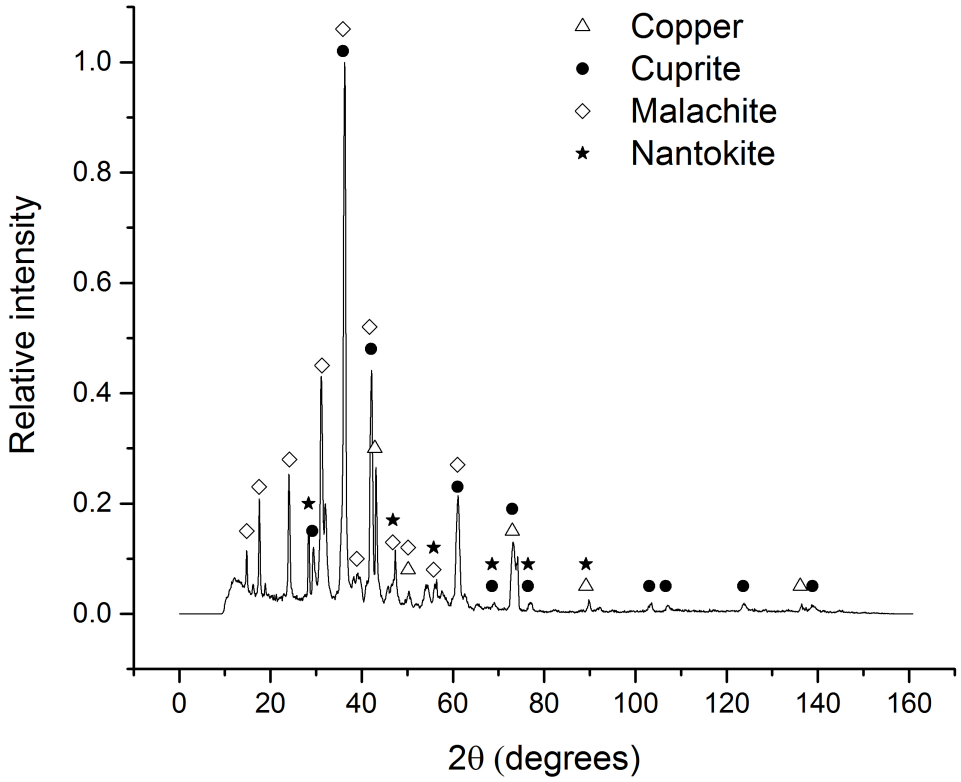

FIGURE B.8: X-ray diffractogram of the patina on sample P5 with labelled peaks for cuprite, malachite, nantokite, and copper.

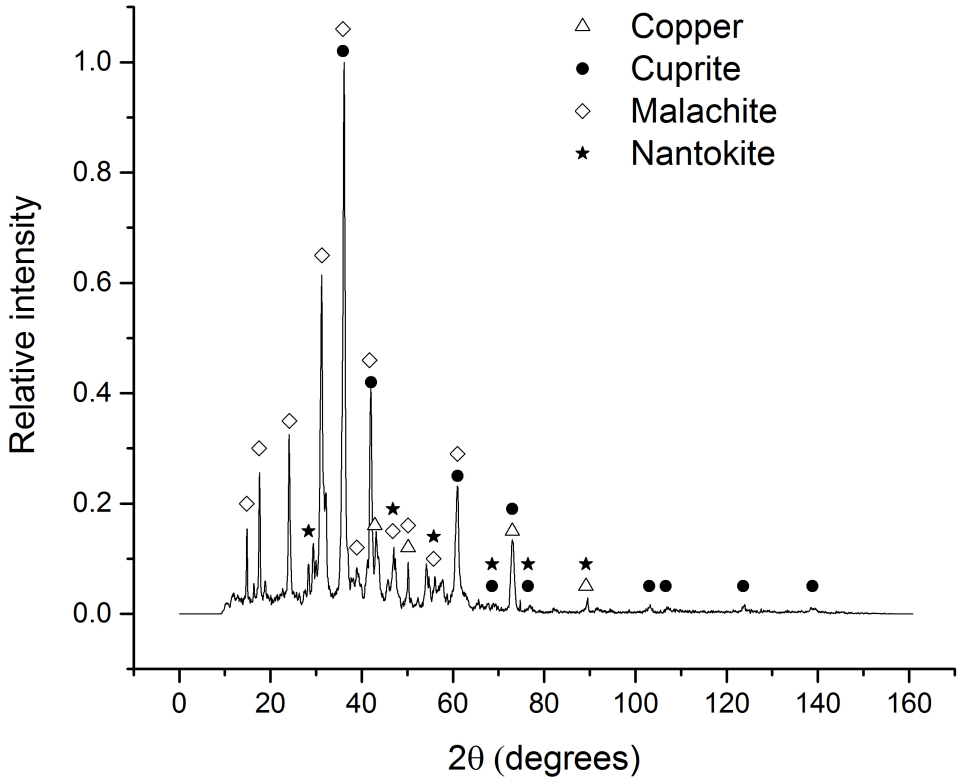

FIGURE B.9: X-ray diffractogram of the patina on sample P6 with labelled peaks for cuprite, malachite, nantokite, and copper.